LUNAR OCCULTATION STUDIES IN THE NEAR INFRARED

Thesis dissertation submitted to
Gujarat University
in partial fulfillment of the requirements
for the degree of
DOCTOR OF PHILOSOPHY
in **PHYSICS**

September 1999

Anandmayee Tej

(Regn. No 4408)

Astronomy & Astrophysics Division
Physical Research Laboratory
Navrangpura, Ahmedabad 380 009
INDIA

Certificate

I hereby declare that the work presented in this thesis is original and has not formed the basis for the award of any degree or diploma by any University or Institution.

Anandmayee Tej
(Author)
Astronomy & Astrophysics Div.
Physical Research Laboratory
Navrangpura
Ahmedabad 380 009
INDIA

T. Chandrasekhar
(Supervisor)
Associate Professor
Astronomy & Astrophysics Div.
Physical Research Laboratory
Navrangpura
Ahmedabad 380 009
INDIA

Contents

List of Tables

List of Figures

Acknowlegdements

To express my deep sense of gratitude in words does not convey my heartfelt adoration for Dr. T. Chandrasekhar, my thesis supervisor. He has bestowed incessant inspiration and encouragement throughout the course of this work. His critical evaluation and suggestions have greatly helped me. I consider it my privilege to be associated with him. I also wish to thank him for the financial support he had extended during my days of bankruptcy.

Dr. N. M. Ashok has been actively involved in my work at all stages. His keen interest and useful suggestions have helped me immensely. I have benefitted a lot from my scientific interactions with Dr. Andrea Richichi. It has improved my understanding of the subject. Desai Saab (Prof. J. N. Desai) is a walking encyclopaedia. The simplicity of his explanations and never ending enthusiasm has greatly influenced me.

I wish to thank Dr. Sam Ragland for introducing me to the field of lunar occultation. Discussions with him regarding the data analysis procedure has been very useful to me. He has been a helpful and encouraging senior colleague.

My interactions with all the faculty members at Thaltej has been very fruitful. The administrative staff at Thaltej and PRL have been very cooperative. I extend my sincere thanks to them.

I thank Mrs. Saroj Jani for generating the occultation predictions. Mr. K. S. B. Manian has always helped to tackle problems related to the instrument. I wish to thank Atmaram bhai for his cooperation and technical help during the design and development of the chopper unit.

Umaben, Rohiniji and other library staff at PRL were always helpful in providing me with the latest study material whenever needed.

I wish to thank Mr. Soumen Mondal, Mr. P. K. Kikani and Mr. C. K. Vishwanath for helping me with the observations. I am indebted to the staff at Gurushikhar especially Mr. Rajesh Shah, Mr. G. S. Rajpurohit and Mr. Jinesh Jain for making my observing runs very smooth and for working overtime and helping me attempt day time events.

Mr. Dholakia has been very cooperative in increasing my disk space whenever I needed. I take this opportunity to thank Dr. U. S. Sutaria and Dr. Gautam Patra for their help and concern.

Words cease to flow when the heart is full of emotions. My family, my fiance, my friends and my loved ones at Pondicherry are gems I treasure in my heart. They have been very close to me, watching and guiding each step of mine. No amount

of words can express my feelings for them so I will not attempt to do so. Just a note to say that I love them all very much.

Lastly, I wish to thank Shri Atal Bihari Vajpayee for treading the road I dreaded. Thanks to him, my rides to PRL were smooth and the last few hectic days were not literally backbreaking.

Chapter 1

Introduction

The intermediate and late type stars are central to a number of exciting research topics in contemporary astrophysics. The study of these cool stars aids in investigating questions pertaining to stellar evolution, model atmospheres, mass loss mechanisms and stellar pulsations. Probing the stellar photosphere and the circumstellar environment can unravel important and crucial information on the nature of the system under study and also give a general insight into stellar astrophysics. The angular diameter alongwith bolometric flux and distance determination can yield the effective temperature and linear radius of the stellar source. Direct determination of these fundamental quantities can pose constraints and establish the validity of the different stellar models. Stellar bodies in general subtend very small angles ($\sim$ a few milli arcseconds (mas)) at the earth, much less than the atmospheric seeing limits. Hence, the need for High Angular Resolution (HAR) studies. HAR is one of the most challenging aims for the current generation of large ground based telescopes. With the advent of long baseline interferometry methods it is possible to overcome the limitations imposed by the atmosphere and to push the instrument performance to the theoretical limits. However, long baseline interferometric methods are extremely demanding in terms of sophisticated technology and excellent sites. Lunar occultation inspite of being an older technique continues to be an attractive alternative to long baseline techniques especially for isolated small observatories of the 1m class.

Improving angular resolution, either for HAR studies or for astrometry, has been a long-standing goal in astronomy. Attempts to measure the small sizes of stellar bodies dates back to Galileo. However, it was first realized by Fizeau (1868) that the diameter of an extended object could be determined from interferometry by measuring the baseline length at which the fringe contrast drops to zero. This concept was exploited by Michelson & Pease (1921) using the 100″ Hooker telescope at Mt. Wilson. They made the important observation that, despite the atmospheric turbulence leading to motion of the fringes, the fringe contrast remains high and the HAR information could be extracted from short exposures. They measured angular sizes of 6 supergiants in the range of 20 – 40 mas. Mechanical instabilities imposed an upper limit to the baseline of 7m. The major difficulty with this technique was to preserve equality of the two light paths from the star to the point where the fringes are formed. The second problem was to make precise visibility measurements in the presence of scintillation.

Intensity Interferometry was the next major long baseline interferometric technique operated at Narrabri (Hanbury Brown et al. 1967; Hanbury Brown 1974). This was radically different from Michelson interferometry. The interference was carried out electrically. The principal advantage with this system was the use of very long baselines without the need for extreme mechanical precision and it was free from the effects of atmospheric scintillation. Using two 6.5m diameter incoherent light collectors and baselines of 10-150m, 32 early type southern stars were observed and angular diameters in the range 0.44 – 5.1 mas were obtained , which is on par with the expectation of the future generation of long baseline interferometry. This method was not used mainly because of the relatively low sensitivity and hence the need for large collectors and it was also incapable of measuring fringe phase. It was not suited for the study of cool stars as infrared (IR) detectors were not used and the maximum possible signal-to-noise (S/N) drops below the detection limits.

Modern Michelson interferometry (I2T) was started by Labeyrie (1975). It was a pioneering work in obtaining direct interference fringes between separate telescopes over an initial baseline of 12m. This technique has made a large contribution to the field of HAR measurements (Di Benedetto & Rabbia 1987; Granes et al. 1986 and Koechlin & Rabbia 1985). The Mark I stellar interferometer (Shao & Staelin 1980) was the first to demonstrate photoelectric fringe detection and phase-coherent fringe tracking. It was followed by Mark II and Mark III (Shao et al. 1987; 1988). The first application of the Michelson Interferometer in the infrared was by McCarthy & Low (1975) at 5 μm. With the use of masks in the aperture plane to isolate a single spatial frequency, they observed 11 late-type stars. The Michelson interferometer was more sensitive in the visible and the near infrared (NIR) but in the mid infrared heterodyne methods were more suited. The first heterodyne interferometer was designed by Johnson et al. (1974) which had a 5.5m baseline and a CO_2-laser local oscillator. Townes and collaborators used the Infrared Spatial heterodyne Interferometer (ISI) at 11μm to study dust shells around evolved stars (Bester et al. 1994, Danchi et al. 1994).

Labeyrie (1970) proposed speckle interferometry to recover the diffraction limited HAR information by recording the fast moving structures inside the seeing disc. Unlike the Michelson interferometry, this yields all the spatial frequencies simultaneously out to the diffraction limit of the telescope. The sampling angle on the object is decided by the observer unlike in lunar occultation. This technique is being extensively used at all large telescopes. The obvious limitation is the diffraction limit and hence the need for very large telescopes. It is not suitable for angular diameter measurements. Curie et al. (1974) introduced the Amplitude interferometer which produces interference fringes from a pair of inch-sized apertures. It provided angular diameter on the brightest red stars including α Ori, α Tau, α Boo and β Peg. Breckinrigde (1972) suggested the Rotating Shearing Interferometer in which the visibility of the perfectly frozen fringes is insensitive to atmospheric scintillations and telescope induced abberations unlike that in speckle interferometry. The interferogram is free of speckle noise. HAR observations of α

Ori with this interferometer revealed the presence of a circumstellar dust envelope and departure from circular symmetry (Roddier & Roddier 1983,1985; Roddier et al. 1986). An alternate approach to obtain diffraction limited imaging is with the use of adaptive optics. Adaptive optics is a means of real-time compensation of atmospherically induced wavefront errors with the help of a reference or guide star. It was first proposed by Babcock (1953). It uses wavefront sensors to measure the wavefront distortion and an optical component (a deformable mirror) to compensate for the wavefront error. It helps to enhance high angular resolution interferometry (Beckers 1993).

The last decade has seen revolutionary advancements in the field of long baseline interferometry. The interferometers in use in this era are:

- GI2T (Grand Interféromètre à Deux Télescopes) operating at CERGA, France – a modified version of the I2T with two 1.5m telescopes and an initial baseline of 70m (Labeyrie et al. 1986).

- SUSI (Sydney University Spatial Interferometer) – a long baseline optical amplitude interferometer (Davis et al. 1999a). It employs small apertures, adaptive optics for wavefront tilt correction and rapid signal sampling to minimize the effects of atmospheric turbulence. Commissioning observations and results are reported in Davis et al. (1999b).

- SOIRDETE (Synthèse d'Overture en Infrarouge à Deux Télescopes) – an infrared interferometer using a fixed 15m baseline with two 1m telescopes (Gay & Mekarnia 1988).

- IRMA (Infrared Michelson Array) operating at Wyoming with baselines between 2.5-19.5m (Dyck et al. 1993).

- IOTA (Infrared Optical Telescope Array) – an infrared array operating at 2.2μm in USA (Dyck et al. 1995).

- COAST (Cambridge Optical Aperture Synthesis Telescope) – a visible/near

infrared interferometer with baselines up to 100m. The first aim was realized in 1995 with the first images of Capella (Baldwin et al. 1996). Images were obtained using visibility amplitude and closure phase measurements together with self calibration methods. Resolving the stellar disk of Betelgeuse and its limb darkening (Burns et al. 1997), first direct detection of variation through its cycle of pulsation of the angular size of a Mira variable, R Leonis (Burns et al. 1998) and further programmes are in progress.

- Mark III in USA – initially designed with the goal of precise wide angle astrometry, it was later augmented to perform parametric imaging (Shao et al. 1988; Mozurkewich et al. 1988, 1991).

- NPOI (The Navy Prototype Optical Interferometer) – a descendant of the Mark I through Mark III series of phase-tracking interferometers. It includes subarrays for imaging and for astrometry. First images were obtained in 1996 (Benson et al. 1997).

1.2 Lunar Occultation

The twinkling of an eye in which stars poetically disappear or reappear beyond the lunar limb, is one of the most rapid of celestial events and ranks at par with solar eclipses as the most ancient of astronomical phenomenon. The first mention of it dates back to Aristotle who had observed the lunar occultation of Mars in 357 B.C. and had inferred that the orbit of the planet was beyond the lunar orbit. Although incapable of maintaining a decent log book, the prehistoric man too must have wondered at this impressive event. It is worth appreciating that in this current generation of long baseline interferometry, lunar occultation has shown remarkable potential in addressing and solving fundamental astrophysical problems. The telescopic era of lunar occultation started with Bullialdus who was the first to observe an occultation event through a telescope in 1623 A.D. The advent of photographic emulsions and techniques marked the beginning of the second

chapter in occultation studies. E. S. King was the first to record an occultation event on a photographic film in 1898 at Harvard. Understanding the nature of occultations was pioneered by Major P. A. Machmohan towards the beginning of the 20th century. Eddington (1918) pointed out that the occultation process is really a diffraction process and Williams (1939) gave the theory of this diffraction pattern in terms of the Fresnel integrals. Whitford's development of sensitive photocells and high gain amplifiers started the generation of photoelectric observations of occultation (Whitford 1939). Nather (1970) revived the occultation program and laid the foundation for the modern era of lunar occultation by introducing the technique of high speed photometry with digital recording. The non linear least squares method of analysing the light curves was established by Nather & McCants (1970). An exhaustive historical outline on lunar occultation can be found in Warner (1988) and White (1987). Table 1.1 lists the lunar occultation chronology. This table is a modified version of the Appendix as given in White (1987).

Lunar occultations have found wide application from X-rays to radio (Ricker et al. 1975; Aschenbach & Brinkmann 1975; Born & Debrunner 1979; Von Hoerner 1964; Lyne 1972 & Singal 1987). It has mainly helped in the astrometry of sources and also in studying the spatial distribution of flux in the emitting regions. Due to the wavelength dependence of the fringe spacing, this technique has been exploited for its HAR capabilities in the optical and the NIR. It offers a simple and productive technique to achieve HAR with a single telescope. Milliarcsecond resolution is achieved by this method with good accuracy ($\sim$ 0.1-0.2 mas). As the moon traverses across the sky at a characteristic 0.5 arc second per second, it occults more distant stellar sources. The angular scales involved being very small, the curvature of the moon is neglected and the lunar limb is considered as a straight edge. At any instant of time the lunar limb projects onto the surface of the earth the diffraction pattern of a sharp unlimited rectilinear edge. The HAR information comes embedded in the Fresnel diffraction pattern. This is the fluctuating intensity at the edge of the lunar shadow as sampled by the telescope. As the moon moves across the source, the fringe pattern moves across the telescope and a light curve is recorded.

An occultation can be observed at the leading edge of the moon (a disappearance) or at the trailing edge (a reappearance). Fig.1.1 gives a schematic illustration of the phenomenon of lunar occultation (disappearance). The observer is situated at the point O and the pattern is recorded as it sweeps across the observer.

For a monochromatic source, the light intensity at any point P, a distance x from the geometric point of occultation is represented by the Fresnel pattern

$$F(\omega) = 0.5I_o[(0.5 + c(\omega))^2 + (0.5 + s(\omega))^2] \tag{1.1}$$

where I_o is the free-field intensity of the stellar source and $c(\omega)$ and $s(\omega)$ are the classical Fresnel diffraction integrals which are defined as

$$c(\omega) = \int_0^\omega cos(\frac{\pi}{2}t^2)dt \tag{1.2}$$

$$s(\omega) = \int_0^\omega sin(\frac{\pi}{2}t^2)dt \tag{1.3}$$

where the dimensionless Fresnel number ω is given by

$$\omega = x(\frac{2}{\lambda D})^{\frac{1}{2}} \tag{1.4}$$

with λ being the wavelength of observation and D the distance to the lunar limb. The geometric point of occultation is defined as the point at which the intensity of the star goes to one-fourth of it initial free-field value.

Fig. 1.2 shows a schematic diagram of the geometry of occultation. If V is the velocity of the moon, ϕ is the position angle of moon's motion and the occultation takes place at a position angle of θ on the disk, then the apparent rate will reduce by a factor $cos\beta$, where, β is the contact angle and is given by

$$\beta = \theta - \phi \tag{1.5}$$

Hence, the velocity component in the direction of occultation is

$$V_{comp} = V cos\beta \tag{1.6}$$

At the lunar distance of $\sim$ 4 $\times 10^5$ km, the lunar motion of 0.5 $''$/s corresponds to the fringe pattern sweeping across the earth at a rate of $\sim$ 1 km/s. The exact

Table 1.1: Lunar occultation chronology.

DATES	SIGNIFICANCE OR EVENTS
Prehistoric to present	A time keeper
375 B.C.	Mars occulted, Aristotle
294 B.C. to 98 A.D.	Seven occultations listed in The Almagest
4 March 640	Aldebaran occulted, Japan
1609	Galileo observes moon with telescope
5 July 1623	Spica occultation observed with a telescope by Bullialdus
1623 to 1900	Occultation evidence for lunar atmosphere
1687 to present	Lunar motion theory
1833 to present	Discovery and resolution of close binaries
1834	Absence of lunar atmosphere was concluded by the suddenness of the event
1878 to 1909	First analysis of lunar motion by lunar occultations
1898	First photographic record of an occultation event by E.S.King
1909	Suggestions to measure stellar diameter by occultation by McMahon
1936,1938	Attempts to measure the diameters of Regulus, β Cap and ν Aqr
1950 to 1953	First successful resolutions of stellar diameters
1950	Suggestion to observe occultations at radio wavelengths by Hetmanzev & Ginzburg
1950 to 1955	Geodetic applications using photoelectric methods
1964	Lunar occultation of Crab Nebula observed in X-rays
1968 to present	Systematic programs for occultation
1970	Nonlinear least squares technique introduced by Nather & McCants for analysis of occultation curves
1970	First infrared observations by Ridgway and Joyce
1976	Surface brightness - diameter calibration by Barnes
1979	Analysis of lunar motion theory, 62000 occultation timings
1980 to present	Effective temperature calibration of cool stars
1980	Resolution of double stars in Hyades
1981	Catalog of occultation binaries by White
1985	Comparison of Laser ranging and occultation results
1986	Remeasure of Antares
1987	Catalog of occultation diameters by White & Feierman
1994,1995	Binaries discovered in Taurus and Ophiuchus SFR
1996	Catalog of 157 occultations from TIRGO
1999	Homogeneous calibration of temperature scale for giants using only LO diameter information
2000 –	Evolution of a common data base using lunar occultation and long baseline techniques

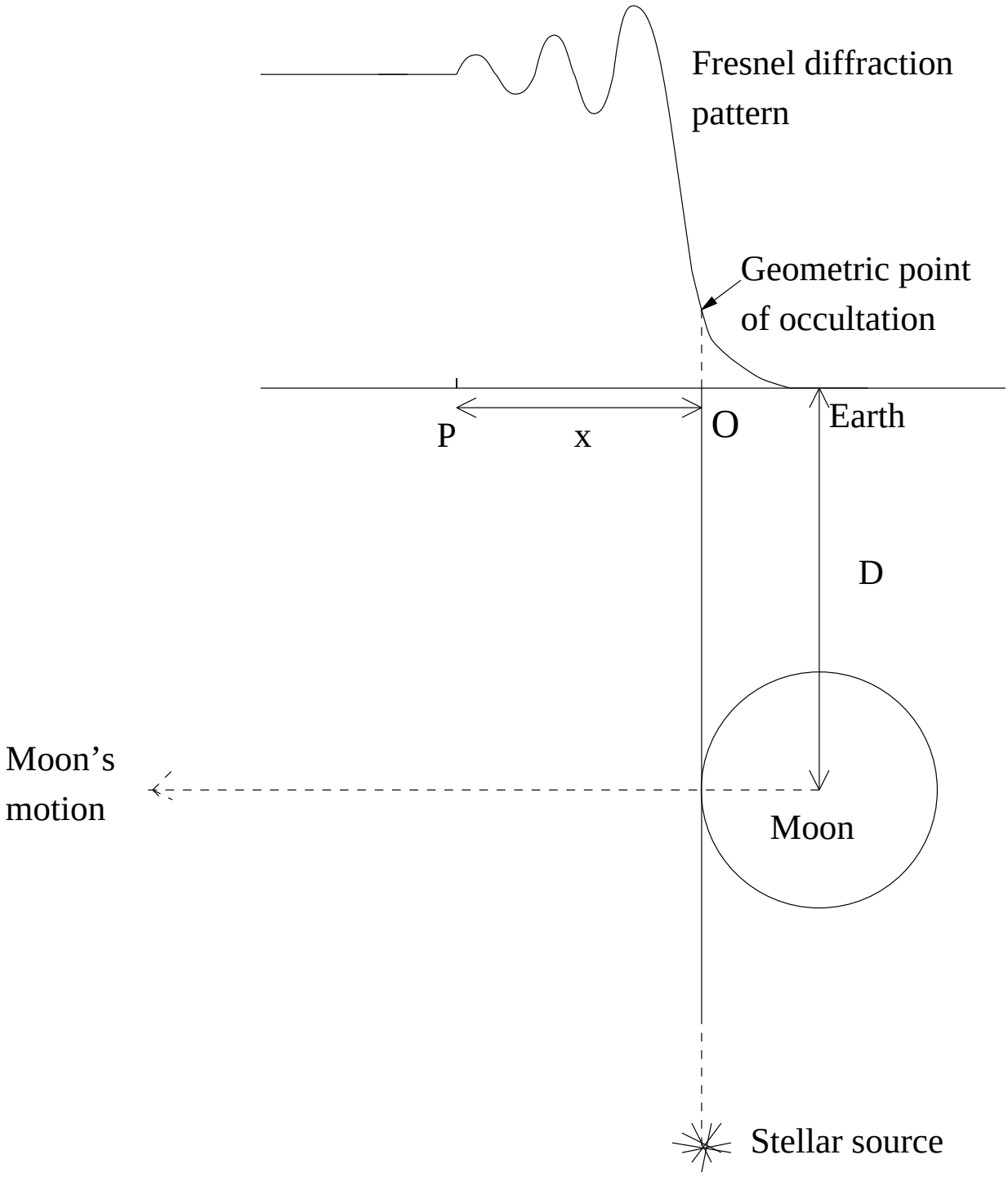

Figure 1.1: Schematic diagram of the lunar occultation phenomenon.

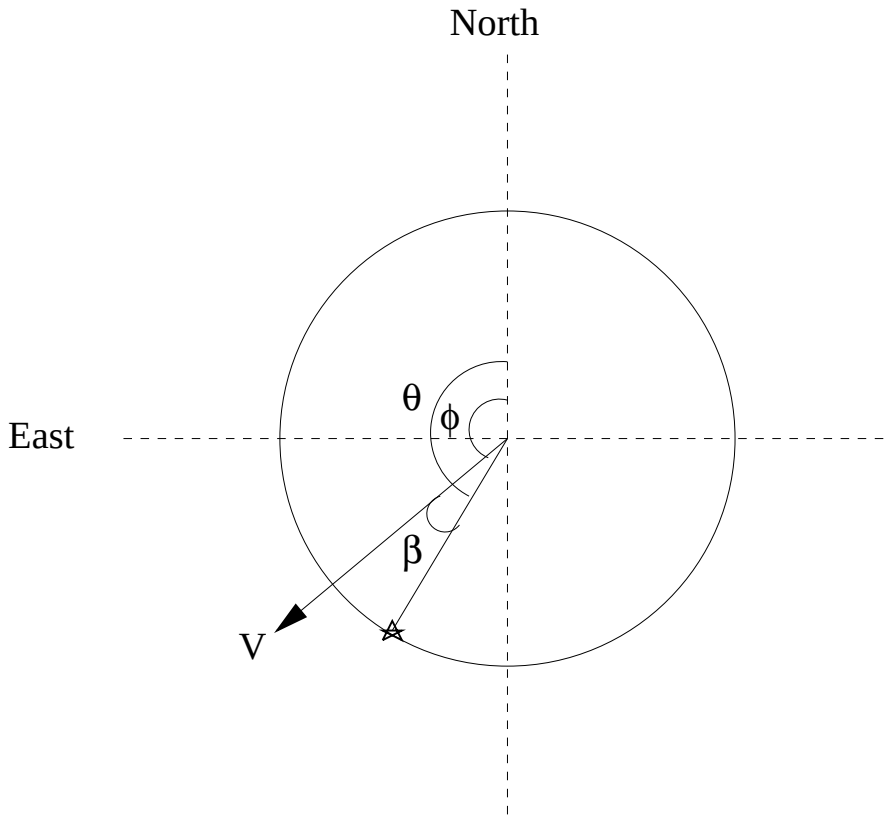

Figure 1.2: Point of occultation on the lunar disk and the velocity vector.

velocity component is unique to each event and depends on many factors like the exact distance to the lunar limb, the position angle of occultation, the lunar velocity vector, the altitude of the moon and the latitude of the observatory.

Taking a typical lunar rate of 0.5 km/s, the time scales for maxima and minima for the optical and the near IR are given in Table 1.2. As is evident from the table, the event is a fast one, it takes only $\sim$ 130 milli seconds for the third maxima to cross the detector plane when observing in the K band. Hence, the need for a high speed photometer to record the fast photometric sequence as the star disappears (or reappears) beyond the edge of the moon. At 2.2μm data sampling at 1-2 milli second level is necessary for retrieving the light curve without losing vital information. The photometer and the data acquisition system used for this thesis work is discussed in Chapter 2. The light curve recorded is the point source Fresnel pattern convolved with various instrumental and source averaging factors. The finite time response of the detector, the finite filter bandwidth and the finite size of

Table 1.2: Maxima & Minima positions as measured from the geometric point of occultation.

Fresnel No	Fringe	Length Scale(m) @			Time Scale(ms) @		
		0.5μm	2.2μm	3.36μm	0.5μm	2.2μm	3.36μm
1.22	Max	12.2	25.6	31.6	24	51	63
1.87	Min	18.7	39.2	48.5	37	78	97
2.35	Max	23.5	49.3	60.9	47	99	122
2.74	Min	27.4	57.5	71.3	55	115	143
3.08	Max	30.8	64.6	79.8	62	129	160

the telescope are the instrumental effects that average the light curve. The spectral energy distribution and the finite size of the source also influence the trace. These effects are to be carefully taken care of in the data analysis procedure to obtain a reliable estimate of the angular diameter of the source. These will be individually explained in detail in Chapter 2.

Advantages and disadvantages of lunar occultation

Two important features of this technique need to be recognized. Firstly, the phenomenon takes place well outside the earth's atmosphere and hence is in principle not limited by 'seeing'. Secondly, the resolution is not limited by the size of the telescope. The telescope aperture plays the role of collecting the flux only. This is the greatest advantage where even a 1m class telescope can achieve resolution down to 2 mas level. The S/N ratio of the occultation light curve is the limiting factor. It would appear that in order to increase the resolution we just need to increase the S/N ratio. But this is practically limited by scintillation. As mentioned by Richichi (1994), simulation studies show that there is a possibility of going down to 0.1 mas resolution by observing very bright giants of intermediate spectral type

through very narrow band filters with 1-2m telescopes. A point which is seldom mentioned or appreciated is the lucky combination of the size and the distance of the moon which accounts for the practical success of the lunar occultation technique. Richichi (1994) gives a simple explanation for this. If the lunar distance would have been less (thus increasing the number of sources covered), then the event would have been too fast and recording it would have been difficult even by today's standard. And if the moon had been farther away, it would have been easier to sample but the events would have been very rare. And a bigger moon would have led to dealing with a lunar atmosphere.

Lunar occultation has some inherent drawbacks. Firstly, it is burdened with the obvious limitation of the choice of the source. Only sources lying in the zodiacal belt and hence in the path of the moon are occulted. Theoretically, this accounts for 10% of the sky. This limitation is not that severe as there are a large number of sources still available unless one is interested in a particular source which is away from the path traversed by the moon. In the TMSS catalogue, of the 5612 sources listed, 3564 are suitably located for lunar occultation and this comprises $\sim 64\%$ of the total number. Secondly, the occultation event is unique in terms of geometry and time. One has to take observations at the exact time of the event. Finally, a single occultation observation gives a one-dimensional scan of the source. But if the event is observed from two different location or the occultation is repeated then it is possible to construct the two-dimensional image of the source.

The NIR is an ideal window to study cool stars and their immediate circumstellar surroundings. This is mainly because these stars radiate most of their energy is this part of the spectrum. It is well known that many stars of the late spectral type show the presence of shells. Tsuji (1978) has pointed out that it is difficult to obtain the photospheric diameter for these stars as it becomes hard to separate the dust from the photosphere. At optical wavelengths, the dust particles scatter the stellar radiation and in the thermal infrared, the dust reradiates

absorbed stellar energy. But in the NIR, the light penetrates to the stellar photosphere and we sample the photospheric continuum emission. In the mid IR again, moon itself is a strong source and poses constraints on observing faint sources. The lunar occultation technique itself has an added advantage in the NIR. A lunar occultation is perforce observed against a bright background of scattered moonlight. Compared to the visible region, the background is less by a factor of ~ 20 in the K band. Hence, the contrast (signal-to-background) is better in the infrared. In the infrared, there is a possibility of recording day time events. But here, the solar elongation becomes a crucial factor. Day time events demand extremely good sky conditions, even a speck of cloud is enough to reflect sunlight into the telescope beam causing system saturation. Thermally excited atmospheric convection currents also increase the scintillation noise. The other slight advantage in the infrared is the fringe spacing. It depends on the wavelength of observation and scales as the square root of the wavelength. Hence, at 2.2μm the fringe spacing is wider by a factor of 2 as compared to the visible region.

1.3 Lunar Occultation Vs Long Baseline Interferometry: The current scenario

Until recently, lunar occultation was the major source of angular diameter information. Despite the limitation imposed by the moon on the sky coverage, the number of direct angular size measurements by this method has been overwhelming (White & Feierman 1987; Richichi et al. 1996a; McAlister 1985 and Dyck 1986). But in the last couple of years, interferometric observations of giants and supergiants have begun to be reported in the literature with an increasing frequency (Dyck et al. 1996, 1998; van Belle et al. 1999; Perrin et al. 1998).

Typically, lunar occultations and long baseline interferometry have operated in different resolution ranges. Lunar occultation was by far the only technique available to reach resolution below 5 mas and has a median of resolved diameters

around 3-4 mas (Ridgway et al. 1980; Richichi 1997; Richichi et al. 1998 a & b; Ragland et al. 1997a) and long baseline interferometry had values close to $\sim$ 10-15 mas (Perrin et al. 1998). However, this gap is vanishing now with longer baselines and more sensitive instruments. van Belle et al. (1999) report the results from the Palomar Testbed Interferometer (PTI) on 69 giants and supergiants observed in the K band. The spectral class of the giants lie between G6 to M6 alongwith a solitary B7 giant and the supergiants lie between F5 and M5. With the use of a mean baseline of 110m, they have reported resolutions down to 1-2 mas with the highest resolution being 1.15 mas. The quoted accuracies are typically $\sim$ 0.05-0.06 mas.

Lunar occultation was again the only technique for HAR study of stars beyond spectral type M5 (Richichi et al. 1998 a & b) as these sources are faint in the visible and were beyond the detection limit of the optical interferometric techniques. But recently, Perrin et al. (1998) using 20m baseline and the FLOUR combiner on the IOTA interferometer give diameter values and hence the effective temperatures of 9 giants ranging in spectral types from K1.5 to M8. They give the extension of the temperature scale beyond M6 for the first time. The uniform disk (UD) values they obtain range between 10-20 mas with 0.2 mas accuracies. Dyck et al. (1998) also present results from IOTA. They give diameter values for 74 cool stars at 2.2μm ranging in spectral type between K0-M8 using a mean baseline of 37.5m. The UD values obtained by them are mostly in the range 5-10 mas.

The future generation of long baseline interferometers promises to revolutionize the field of HAR astronomy by breaking the limitations of seeing and pushing the angular resolution limits to the sub-milli arcsecond level. Then it will surpass the limits of lunar occultation. Resolution below $\sim$1 mas is practically not possible with the lunar occultation technique. Even though data analysis techniques (Knoechel & von Der Heide 1978; Richichi et al. 1992) have been established to minimize the low frequency part of the scintillation thereby increasing the effective S/N ratio, it seems unlikely to improve the resolution. The resolution with the

NPOI will be $\approx 200\mu$as with the 437m baselines being operational. It is sufficient to measure the diameters of all stars later than F with $m_v \leq$ 7-8 magnitudes. The Next Generation Array (NGA) based on the experience of COAST is being planned with twenty 1.5m movable telescopes with baselines up to 500m. Operating in the 0.6-2.2μm, this can achieve micro arcsecond resolution. SUSI, in the fully operational form with baselines 5-640m and spectral range of operation of 0.4-0.9μm will have resolutions between 0.05-20 mas.

In addition to transparency at ultraviolet and infrared wavelengths, space offers considerable advantage of suppressed atmospheric disturbances. It provides a significant increase in the resolution and sensitivity and an unlimited isoplanatic patch size. Regarding the stability at the wavelength scale, large systems floating in space have the advantage of being in a seismically and acoustically quiet environment. A number of proposed projects have been outlined in Shao & Colavita (1992). Connected-element interferometers (Traub & Gursky 1980), free-flying spacecraft (Labeyrie et al. 1984) and moon as a suitable platform (Labeyrie 1978) have been proposed. Kilometric baseline space interferometry will show the full advantages of long baseline interferometry, initially with astrometry at the micro arcsecond level and eventually with very high resolution imaging.

We are hence stepping into the next millennium with such impressive and sophisticated facilities. But in this race for the highest possible angular resolution, one should not forget the contribution of lunar occultation. The attractive features of it are:

- It is a simple technique which can be implemented with a single small telescope.
- The data reduction and analysis methods are involved but not as cumbersome as that of interferometric techniques.
- Sky condition is not a stringent requirement. Light curves observed through thin clouds can yield good scientific results.

- Last but not the least, it does not require dedicated time on large telescopes.

1.4 Scope of the technique and motivation for the present work

By itself, the angular diameter of a star has no intrinsic value but in conjunction with other observational data it enables the basic physical properties of the star to be deduced. It then becomes possible to make direct comparison of the observed properties of the star with the predictions of theoretical models of stellar atmospheres and interiors.

Measurement of angular diameters is the only direct means of deriving the effective temperature (T_{eff}). From the basic definition it follows that

$$T_{eff} = \left[\frac{4F}{\phi^2\sigma}\right]^{\frac{1}{4}} \tag{1.7}$$

where, F is the bolometric flux which can be estimated from the multiwavelength photometry of the source, ϕ is the angular diameter and σ is the Stefan-Boltzman constant. The effective temperature is a fundamental quantity characterising a star. Since effective temperatures are relatively poorly estimated especially for the cool spectral types, these determinations are of fundamental importance to stellar astrophysics.

The recent accurate parallax measurements, from the Hipparcos mission, are beginning to permit the direct conversion of the measured angular diameter to linear stellar radii. The absolute luminosity of the star can be estimated from the knowledge of the bolometric flux and the distance and thus enables the star to be plotted as an empirical point in the theoretical HR diagram. If the mass of the star is also known, these parameters can pose tighter constraints on stellar evolutionary models.

Lunar occultation has offered great potential in detecting and studying multiple systems. This has represented one of the main applications of lunar occultation (Evans & Fekel 1979; Evans et al. 1985; Richichi et al. 1997; Richichi et al.

1996b; Richichi et al. 1994a). A single observation yields only the projected separation between the components because of the one-dimensional nature of the scan obtained. Observations at two different position angles can give the true separation. Apart from determining the orbital parameters, the nature of lunar occultations is suited for new discoveries which can be followed up by other methods. Multiplicity at early stages of star formation in the Taurus and Ophiuchus clouds has been extensively surveyed by lunar occultation, speckle interferometry and direct imaging (Richichi et al. 1994b; and Simon et al. 1995). The limiting separation is ~ 5 mas which is now easily achievable by interferometric techniques. Lunar occultation still offers unrivaled capabilities of limiting magnitudes and dynamic range ($\Delta m \sim 1.5$). Only the NPOI promises to go down to such resolutions (Armstrong et al. 1998). The expected resolution is ~ 65 μas for $\Delta m \sim 0$ and ~ 200 μas for $\Delta m \sim$ 3-4 mag.

That all cool giants of spectral type M0 or later have circumstellar gas shells was first stated by Deutsch (1960). Circumstellar envelopes at angular scales of few arc minutes have been well studied from CO millimeter observations (Sargent & Beckwith 1987) and IRAS data (Young et al. 1993). 10μm observations have revealed the presence dust component in the shells. However, the direct detections of these shells are limited. Danchi et al. (1994) have studied the distribution of dust around a sample of well known late-type stars from the 11μm spatial interferometric observations. They classify these stars into two categories. One with the inner radii of the dust shell very close to the photosphere (3 – 5 $R_\star$) and at a higher temperature ($\sim$ 1200 K). $R_\star$ corresponds to one stellar radius. In this class the asymmetric distribution of warm dust at a few stellar radii of the bright carbon star TX Psc was detected by lunar occultation (Richichi et al. 1995). The other class is of dust shells with large inner radii ($\geq$ 8 $R_\star$). In a recent work the detection of a shell around M1 supergiant TV Gem was reported (Ragland et al. 1997b). The lunar occultation light curve reveals the presence of an inner shell at $\sim$ 20 $R_\star$ and an outer shell at $\sim$ 500$R_\star$ is deduced using IRAS photometric data. The presence of dust in these two isolated shells suggests an episodic or sporadic mass loss in

TV Gem. In a lunar occultation light curve the circumstellar feature shows up as a smooth monotonically varying background superimposed on the fringe pattern of the central star. Lunar occultation has good capability of exploring this field because of the high angular resolution that can be achieved to study the circumstellar envelopes and disks present very close to the stellar photosphere of very young and cool stellar systems.

The study of Mira type stars are important as they play a crucial role in enriching the interstellar medium with dust and gas because of their high mass loss rate. Located at the tip of the Asymptotic Giant Branch (AGB), these large amplitude variables help in our understanding of strong mass loss, the formation of planetary nebulae and the structure of the white dwarf mass function. Another interesting application of lunar occultation is that it can be used as a tool to investigate the pulsational properties of Mira type variables. The mode of pulsation of this group of stars is still an unresolved problem. An accurate determination of the angular size along with the parallax can give a precise linear radii for these stars and help in determining the mode of pulsation using well established theoretical Period-Mass-Radius relations.

In India, the technique of lunar occultation has been extensively used at radio wavelengths. The Ooty Radio Telescope (ORT), in the shape of a large parabolic cylinder, has been designed to take advantage of this technique and provide arc second resolution. Being operated at 327 MHz, this has helped derive positional and structural information of $\sim$1000 radio sources (Singal 1987 and references therein). These mainly include sources in Abell clusters and 3C radio sources. Lunar occultations in the visible have been attempted by scientists at the Indian Institute of Astrophysics, Bangalore and also by us here at the Physical Research Laboratory (PRL) (Chandrasekhar et al. 1992). However, observations in the near infrared has been pioneered by the PRL group (Ashok et al. 1994; Ragland 1996; Ragland et al. 1997 a & b).

The 1 m class telescopes available in the country suffice for good scientific

work and have the potential to address the problems mentioned above. The 2.2μm and 3.36μm windows are best suited for study of late type stars. The observations related to this thesis work have been done in these two infrared windows, mainly at 2.2μm. In this thesis, we have concentrated on deriving reliable angular diameter values for a sample of M giants and determining their effective temperatures accurately. Though we do not have a statistically large sample to derive an independent temperature calibration, we have several new angular size determinations and the results obtained will serve as benchmarks for future work in this field. Another important aspect of this thesis is to measure the angular diameter of the Mira variable R Leonis at 3.36μm and 2.2 μm and study the phase and wavelength dependent variation of this source and to derive the mode of pulsation.

1.5 Sample Selection and Observations

A vigorous attempt has been made to observe all suitable occultation events in the broad K band during the period of this thesis work. The telescope time being a limiting factor, the sample selection was primarily based on the following criteria:

- Individual source history with special focus on M type giants and other interesting sources.
- Geometry of occultation and feasibility of the event.
- Event time, solar elongation for twilight events.
- Phase of the moon.
- Altitude of the source above horizon at Gurushikhar.

All the sources in our sample were chosen from the Two Micron Sky Survey and hence are brighter than 3^{rd} magnitude in K except one SAO source. This ensures a good S/N ratio of the light curves. We have attempted over 100 occultation events and have successfully observed 42 of them. Out of these only 27 light

curves with good S/N ratio were chosen for detailed analysis. The complete list of the sources successfully observed are given in Table 1.3 at the end of this chapter.

The observations mentioned in this thesis were taken at the Cassegrain focus of the 1.2m IR telescope at Gurushikhar, India (72^o 46′ 45.″ 9 E, 24^o 39′ 10.″ 9 N; 1680 m) with the photometric system described in Chapter 2. Except for R Leo, which was observed in the narrow band Circularly Variable Filter (CVF) at 3.36μm ($\Delta\lambda$ = 0.05μm), all other observations were taken in the standard broad band K filter ($\lambda = 2.2\mu m, \Delta\lambda = 0.4\mu m$).

Compared to disappearances, reappearance events are difficult to observe since the source is behind the moon before it reappears. Here, one has to do offset guiding of a nearby (within 5 degrees) star which itself is not occulted. A visually bright ($\sim$ 5-6th mag) star is preferred and the guiding is done by placing this reference star at the centre of the cross wire of the eyepiece. In the absence of a visually bright star nearby, we choose a reference star bright in K with a strong signal. A visually bright star has a distinct advantage while observing in less than optimal sky conditions and in the vicinity of the bright lunar limb. In such a situation guiding the star by signal maximization becomes difficult due to the fluctuations in the signal level itself.

The observing procedure includes taking the coordinate difference, as seen on the telescope console, for the program star and the guide star well before the event. On several occasions we take this difference the previous day at the same altitude of the event. This takes care of the differential flexure of the telescope structure. This becomes crucial if the event takes place at lower altitudes and the reference star is slightly further away. An hour before the event the console reading of the reference star is taken and this is repeated at regular intervals ($\sim$ 10 mins). The frequency of readings is increased in the last 20 minutes before the event. This helps to give corrections to account for problems related to the telescope drift. A few minutes ($\sim$ 5) before the time of reappearance, the difference is given to the telescope to point to the program star. The bias level is adjusted to avoid system

saturation and is placed at a convenient position to account for the negative slope of the background level, due to the receding lunar limb, as seen by the detector. This simple procedure has been followed and reappearances are being routinely observed with a high success rate.

1.6 Outline of the thesis

This thesis consists of six chapters. The present chapter briefly reviews the field of HAR and introduces the technique of lunar occultation. As a part of this thesis work, an angular chopper has been designed and developed for accurate photometry. A brief description of the instrument used and the details of the angular chopper are discussed in Chapter 2. This chapter also includes the details of the data analysis procedure and an exhaustive discussion of the laboratory calibration of the detector system used. Phase-dependent and wavelength-dependent variations of the angular size and the mode of pulsation of the Mira variable R Leonis are presented in Chapter 3. This chapter also includes results on the bright infrared source and suspected Mira variable IRC-20563. The measured angular diameters and the derived effective temperatures of a sample of 15 M giants are discussed in Chapter 4. Chapter 5 comprises results on sources of other spectral types. The sixth and last chapter gives a summary of the work done and outlines the scope for future research in this field.

Table 1.3: Details of the 42 successful events.

Sr. No.	Source	Date	Event type	V	K	* Phase
1.	SAO 94345	1995 Jan 13	D	6.50	7.00	12.24
2.	IRC-20379	1995 Feb 24	R	12.00	2.26	24.15
3.	IRC-10301	1995 Mar 20	R	7.20	1.56	18.28
4.	IRC-10305	1995 Mar 20	R	7.50	2.37	18.45
5.	IRC-20470	1995 Mar 24	R	-	2.36	22.48
6.	IRC-20474	1995 Mar 24	R	7.50	2.44	22.52
7.	IRC+20125	1995 Apr 06	D	8.70	2.77	6.53
8.	IRC-20497	1995 May 17	R	7.20	0.72	18.03
9.	IRC-20502	1995 May 17	R	7.10	2.92	18.07
10.	SAO 158836	1995 May 17	D	5.3	4.39	12.32
11.	IRC-20271	1995 Jun 10	D	2.90	2.41	12.33
12.	IRC-20299	1995 Jun 11	D	9.08	2.13	13.38
13.	IRC-20453	1995 Oct 28	D	-	2.38	4.39
14.	IRC+10032	1995 Dec 04	D	7.58	2.64	11.94
15.	IRC+10034	1995 Dec 04	D	8.71	1.28	12.02
16.	IRC-20429	1996 Feb 14	R	-	2.86	25.5
17.	IRC+20090	1996 Feb 26	D	$\sim$11	2.79	7.7
18.	IRC+20111	1996 Feb 27	D	8.40	1.35	8.58
19.	IRC+20112	1996 Feb 27	D	4.70	-1.03	8.62
20.	IRC+20076	1996 Mar 24	D	3.90	1.57	5.19
21.	IRC-20563	1996 Apr 10	R	11.10	0.78	22.43
22.	IRC-20444	1996 May 06	R	-	1.69	18.96
23.	IRC+10194	1996 May 23	D	6.80	1.87	6.10
24.	IRC-20563	1996 Nov 15	D	11.10	0.78	4.44
25.	IRC-10580	1996 Nov 18	D	8.52	0.47	7.5
26.	IRC+20166	1996 Dec 25	R	5.94	0.79	15.04
27.	IRC+20191	1996 Dec 26	R	6.00	2.90	16.17
28.	IRC+10038	1997 Jan 17	D	9.00	2.37	7.36
29.	IRC-20325	1997 Feb 02	R	5.00	2.35	24.77
30.	IRC-20382	1997 Feb 04	R	8.60	2.05	25.87
31.	IRC+20067	1997 Feb 14	D	9.10	2.75	7.08
32.	IRC+20191	1997 Mar 18	D	6.00	2.90	9.62
33.	IRC+10206	1997 Mar 20	D	5.10	2.64	11.55
34.	IRC+10232	1997 May 15	D	5.20	2.90	7.77
35.	IRC-20362	1997 May 23	R	-	2.83	17.08
36.	IRC-20557	1997 May 25	R	-	2.70	18.95
37.	IRC-10300	1997 Jun 16	D	4.30	1.01	11.36
38.	IRC-20301	1997 Jun 18	D	6.80	1.65	13.34
39.	IRC+10215	1997 Dec 19	R	4.40 – 11.30	-2.6 – -2.3	18.85
40.	IRC-10308	1998 Jan 22	R	7.10	0.15	23.3
41.	IRC-10308	1998 Apr 13	R	7.10	0.15	16.9
42.	IRC-20362	1998 Apr 16	R	-	2.83	19.95

* Phase here refers to days after new moon.

Chapter 2

Instrumentation, Data Analysis and System Calibration

This chapter gives a technical overview of the instrument used for observation with the emphasis on the chopper designed, the details of the data analysis procedure and the experiments performed to calibrate the system.

2.1 Instrumentation

The photometer used for the work presented here has been developed by the IR group of PRL prior to this thesis work. A detailed description of the system can be found in Ashok et al. (1994) and Ragland (1996). This instrument has been extensively used for lunar occultation observations, photometry of eclipsing binary systems, studies of classical novae and related objects, photometry of comets etc. As a part of this thesis work, an angular chopper was designed and developed. This replaced the linear tertiary mirror in the existing chopper. A brief description of the photometer and details of the angular chopper set up will be discussed in the following sections.

2.1.1 The IR Fast Photometer

The optical and mechanical layout of the photometer is shown in Fig. 2.1. The main parts of the photometer are

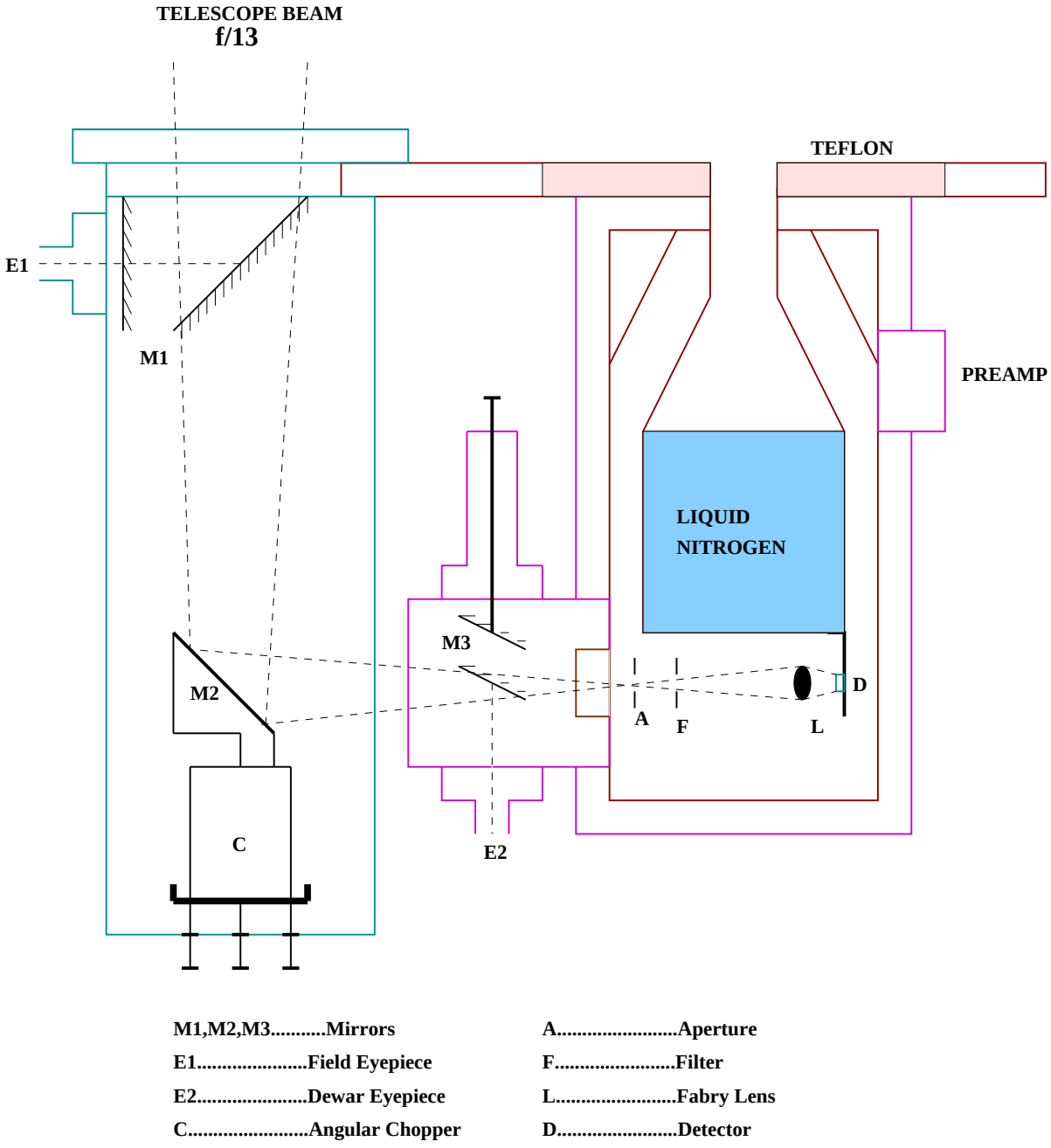

Figure 2.1: The schematic diagram of the Fast IR Photometer.

1. The LN_2 cooled dewar which houses the InSb IR detector. This is attached independently to the Cassegrain plate. Care is taken to electrically isolate it from the telescope body using teflon supports. This is done to avoid 50 Hz contamination from the mains power line due to earthing problems.

2. The rectangular metallic box which has the field eyepiece and the chopper mounted inside it. This box is rigidly coupled to the Cassegrain plate.

3. The dewar eyepiece which is attached to the quartz window of the dewar.

Two side-looking dewars namely the fast dewar (D1) and the CVF dewar (D2) have been used for all the observations reported in this thesis work. The InSb detector (D) is attached to the cold bottom plate of the dewar. It is sufficiently baffled to reduce background radiation falling on it. The aperture wheel (A), the filter wheel (F) and the Fabry lens (F) are also mounted on this plate. The CVF dewar has a different optical set up. In this there is a focal ratio changer after the aperture wheel which operates in the $f/13 \Leftrightarrow f/20$ mode and the Fabry lens is replaced by an off-axis Fabry mirror.

The f/13 beam from the telescope falls on the chopper mirror (M2) mounted at 45^o to the central axis of the telescope. After a right angled reflection at M2 the beam is directed into the dewar housing. The field eyepiece E1 is used to centre the source with the help of the flip mirror M1 which can be placed in the path of the beam. The mirror M3 deflects the light into the dewar eyepiece E2. This is used to fine tune the optical alignment of the system. With the mirrors M1 and M3 removed from the path, the undeflected beam goes through the aperture wheel, the filter wheel and falls on the Fabry lens/mirror which focuses all the light falling on the focal plane aperture uniformly on the detector.

Both the dewars house photovoltaic InSb detectors of 0.5mm diameter with a spectral range of 1-5 μm. The specifications of the two dewars are given in Table 2.1. The filter characteristics of the two dewars are given in Table 2.2. Dewar D1 has an additional option of two switchable feedback resistors (R_f). Experimentally

Table 2.1: Electrical Characteristics of the two dewars.

Components	Specifications	Dewar 1 (FAST)	Dewar 2 (CVF)
1. Detector	Impedance @77K (R_D)	$1.2 \times 10^9 \Omega$	$2 \times 10^9 \Omega$
	NEP	$5.6 \times 10^{-15} W/\sqrt{Hz}$ (40 Hz, K)	$4 \times 10^{-15} W/\sqrt{Hz}$ (20 Hz, K)
2. Pre Amp.	Feedback resistor (R_f) @77 K	$1.87 \times 10^8 \Omega$ $2.12 \times 10^{10} \Omega$	$2.5 \times 10^8 \Omega$
	Voltage Responsivity	-	2.2×10^{10} V/W
	Current Responsivity	0.54 A/W	-
	Pre Amp. noise with feedback resistor	$0.31 \times 10^{-6} V/\sqrt{Hz}$ @40 Hz	$9 \times 10^{-7} V/\sqrt{Hz}$ @20 Hz

Table 2.2: Filter Characteristics of the two Dewars.

Band	Dewar 1 (Fast) λ (μm)	$\Delta(\lambda)$ (μm)	Dewar 2 (CVF) λ (μm)	$\Delta(\lambda)$ (μm)
J	1.25	0.31	1.26	0.32
H	1.65	0.29	1.65	0.34
K	2.20	0.36	2.20	0.40
L	3.80	0.66	-	-
M	4.71	0.64	-	-
CVF_{min}	-	-	1.7	$\sim$0.03
CVF_{max}	-	-	3.4	$\sim$0.05

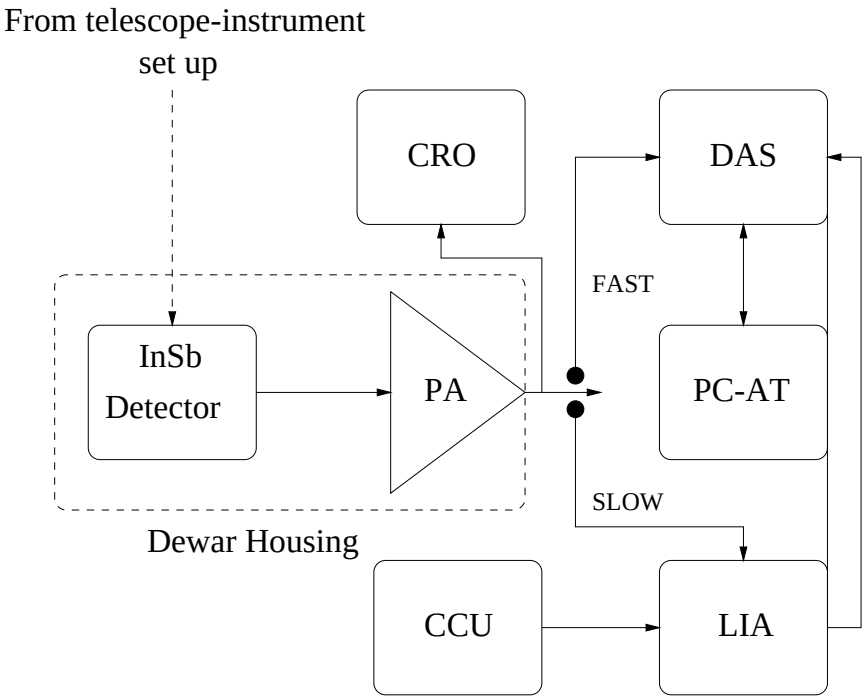

Figure 2.2: The block diagram of the telescope-instrument set up.

it has been determined that the time constants (i.e. the time taken for the signal to reach $1/e$ of its initial value) for the two modes are $\tau_{hi} \sim 7$ms and $\tau_{lo} < 0.1$ms. The gain being a factor of 100 better in the high R_f configuration, the system has been used in this mode for better sensitivity. A careful consideration of the time response of the dewars used has been an essential part of the data analysis.

Fig. 2.2 gives a block diagram of the entire set up. For lunar occultation observations the preamplifier (PA) output is directly read by the data acquisition system. But in case of conventional photometry, an intermediate stage of the lock-in amplifier (LIA) exists. Lock-in amplifiers use a technique known as phase-sensitive detection to single out the component of the signal at a specific reference frequency and phase. Noise signals at frequencies other than the reference frequency are rejected and do not affect the measurement. A reference signal from the chopper control unit (CCU) at the frequency of chopping is fed to the lock-in amplifier to which the the preamplifier output is phase-locked. This ensures that the lock-in

output is a dc signal. After this phase sensitive detection the output goes to the data acquisition system. A Keithley system 575 is used for data acquisition. It has a 16 bit A/D converter and can be easily interfaced with IBM-like PCs.

2.1.2 Angular Chopper

As will be discussed later, the finite size of the source smears the fringe pattern of the lunar occultation light curve. This smearing effect is proportional to the size of the source, hence the number of fringes visible increases with the decrease in the size. The angular resolution of lunar occultation is thus ultimately related to the number of fringes that can be detected above the noise threshold, i.e., it is limited by the finite S/N ratio of the light curve. In all our occultation observations we have been restricted to sources with K magnitudes brighter than 3 to get sufficient S/N ratio to fully exploit the technique down to resolutions of 2mas. But there are a bountiful of interesting sources which are fainter than this but at present beyond the limit of our system sensitivity. Other than a larger telescope (which is a limitation with us), chopping is the only way of going to fainter magnitudes with the required S/N ratios with this single element detector system. This discriminates against a strong sky background which is of concern in infrared photometry. In this two neighbouring portions of the sky, one containing the star and the sky and the other containing only the sky are presented alternately to the detector and their difference is taken electronically by phase-sensitive rectification. This removes the sky background electronically. The chopped output we measure is $(Star + Sky) - (Sky)$. Simon et al. (1985), in their lunar occultation observations of the obscured star forming region M8E-IR at 3.8 μm and 10 μm have used phase-sensitive detection with the sky chopper at 80 Hz to reduce the strong lunar background. This prompted us to investigate the possibility of using this technique with the aim of going fainter.

With the existing linear chopper, sufficient sky throw was a setback even

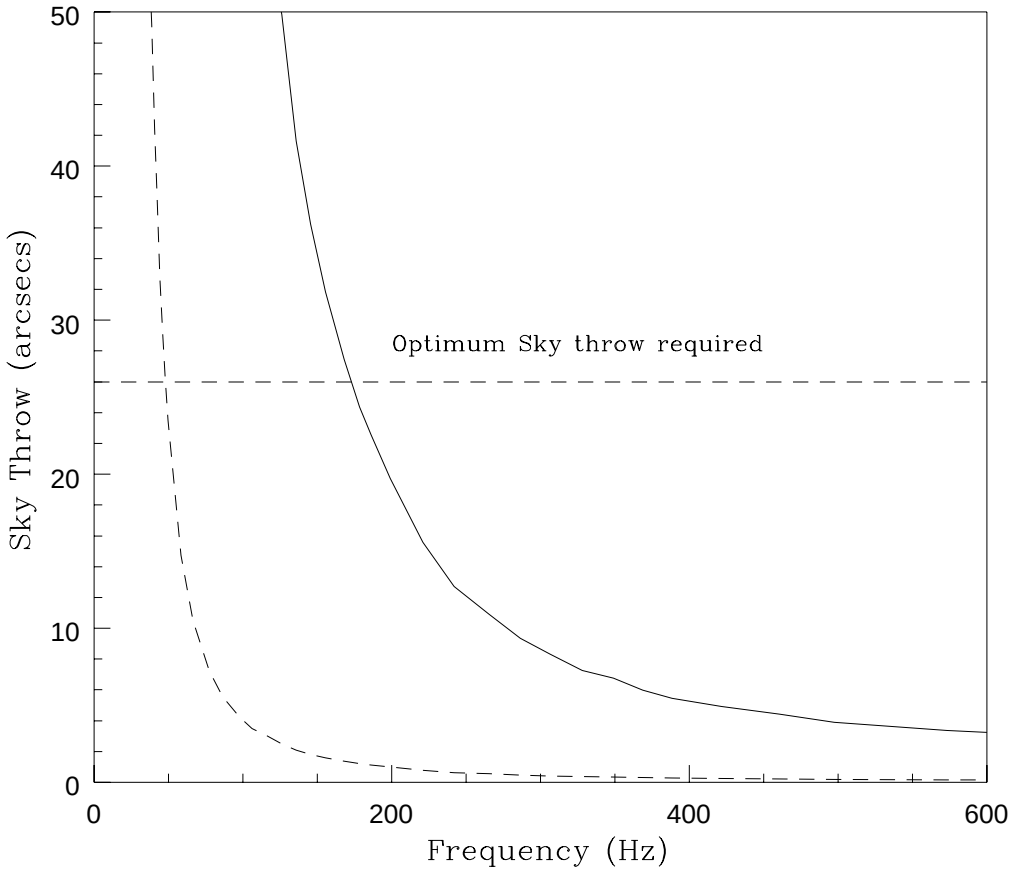

Figure 2.3: The sky throw versus the chopping frequency for the angular (solid line) and the linear (dashed line) chopping modes. The line shows the optimum sky throw required.

for the conventional slow photometry. This required very high power to the chopper motor and thus resulted in producing highly distorted beam profiles. Hence, angular chopping was considered as a better alternative to this. To record occultation events in the chopping mode requires fast chopping at the rate of the signal sampling, i.e., at 1 KHz. This aspect of observing could not be firmly established due to difficulty in getting proper throw at very high frequencies. Fig. 2.3 shows the frequency response in terms of the sky throw achievable in case of the angular and the linear chopper. The optimum sky throw line shown corresponds to 26 arcseconds, which takes the beam out of the detector. From laboratory experiments

described later, it appears that the present configuration of the angular chopper is usable upto 350 Hz with the optimum sky throw. We observed the occultation of 64 Tauri at 100 Hz, but the light curve recorded was very noisy. However, the extensive laboratory testing done for this purpose resulted in a good photometric system which has been used thereafter.

An important aspect of the work is to obtain the JHK photometry of the occulted source in order to get an accurate estimate of the bolometric flux. For most of the sources in our sample, the spectral energy distribution peaks in the NIR and hence JHK fluxes cover the critical region of the flux distribution curves for these sources. As already stated above, chopping is done to subtract the sky background. In the absence of the wobbling secondary mirror in our telescope configuration, this is achieved by the tertiary focal plane chopper. The chopping frequency is normally fixed between 10-15 Hz.

The original system described in Ashok et al. (1994) and Ragland (1996) had the linear chopper set up. This is the conventional chopper configuration which consists of a flat mirror attached at the centre to the central shaft of the chopper motor. Apart from the lack of sufficient throw at low power to the chopper, the main problem with this system was the lack of stability. With the ends of the mirror being free, the force being applied to the centre distorted the beam profile. Lack of stability and repeatability of the beam profile showed up in the accuracy of the photometry which was of concern. These drawbacks of the linear chopper have been overcome to a great extent by the angular chopper configuration.

Fig. 2.4 shows the schematic of the angular chopper unit. In this set up one end of the tertiary mirror is held at 45^o to the telescope axis by a L shaped shaft which is coupled to the core of the Linear Voltage Differential Transformer (LVDT). The other end is rigidly fixed to the base plate (B). The core is then fixed to the diaphragm of the chopper. The LVDT output is calibrated to the linear displacement of the core and hence is used to monitor the core displacement and the beam contour. This can also be used as a feedback to the chopper motor control unit to

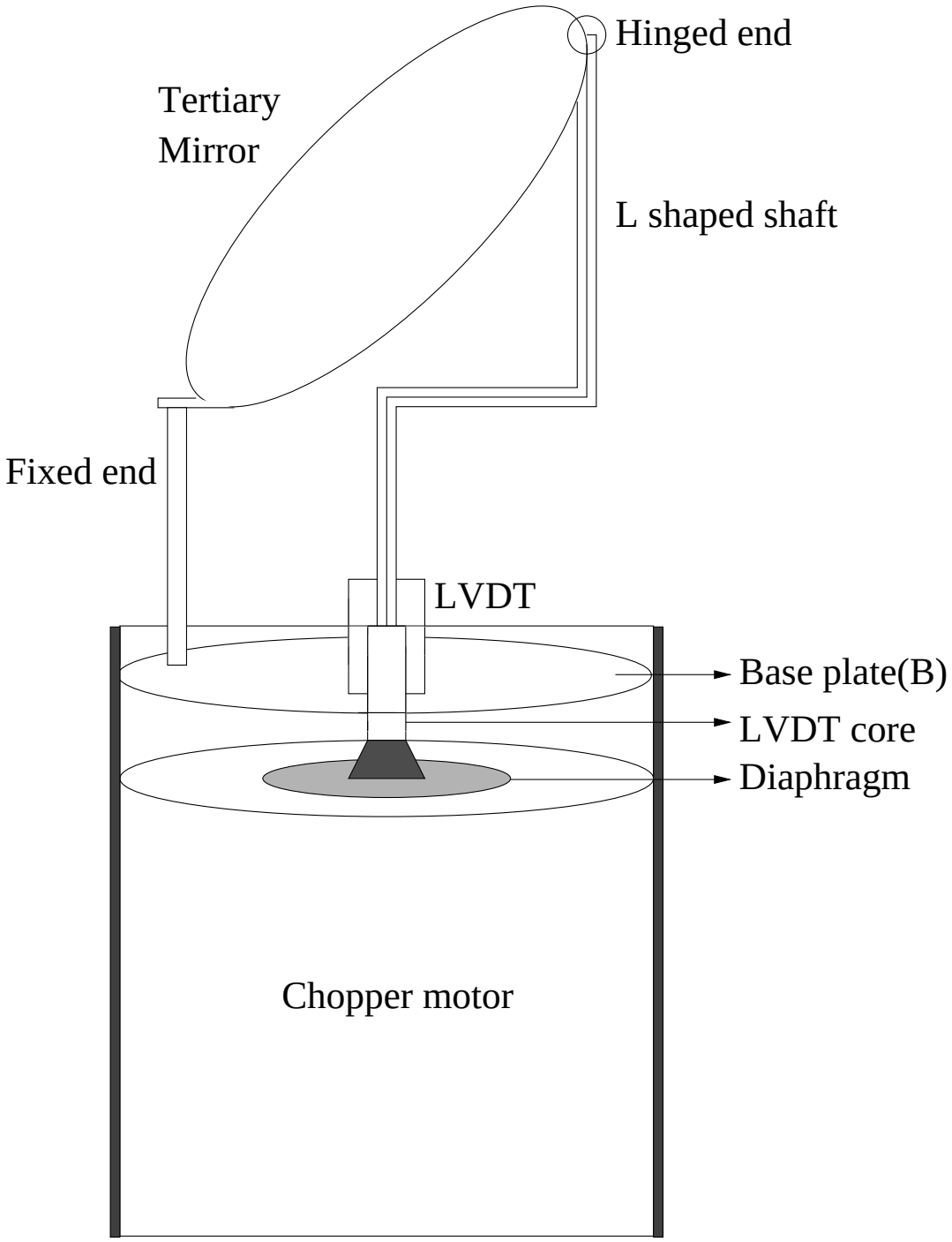

Figure 2.4: The schematic diagram of the angular chopper.

ensure that the signal fed to the chopper is a perfect square wave. But this option has not been used in our observations. Mechanically, this LVDT set up restricts the freedom of movement of the core and adds to the stability of the system. The free movement of both ends of the mirror is also arrested, hence, we get a stable and rigid system.

In this configuration the force from the chopper motor is transmitted through the core and the L-shaped attachment to the hinged end of the mirror. This makes the motion of the mirror angular. When the mirror is pushed by an angle θ, the telescope beam gets reflected through 2θ. This gives sufficient throw in the sky even with very small linear displacement of the shaft, i.e., with a small power to the chopper motor. In our configuration, to get a minimum throw of $\sim$ 26 arcsecs, the mirror has to tilt by an angle of $\sim 11.5'$. This requires a very small ($\sim 100\ \mu$m) linear displacement of the shaft. A small linear movement is translated into a large angular displacement and this is the most important advantage of the angular chopper. Extensive testing of this system was done in the laboratory before it was attached to the photometer and used for regular observations.

A simple experimental set up was used to check the system stability. In this a laser source is held rigidly along the axis of the chopper and the beam is chopped by vibrating the chopper at the frequency of operation. The reflected beam is then allowed to fall on a distant wall. In case of a rigid and stable system the reflected beam makes two well defined spots on the wall and the positions are repeatable. An alternate approach was also tried out. Here, the reflected laser is allowed to fall on a photodiode kept at some distance. The output of the photodiode is fed to a spectrum analyser. If the stability of the system is maintained then the spectrum shows a dominant component at the frequency of chopping and other frequency components are more or less absent. Fig. 2.5 shows the spectrum analyser output at a chopper frequency of 350Hz tried out for the fast chopping mode. As is clearly seen it has a dominant component at the frequency of chopping. After studying the stability of the spots on the wall and the output of the spectrum analyser the

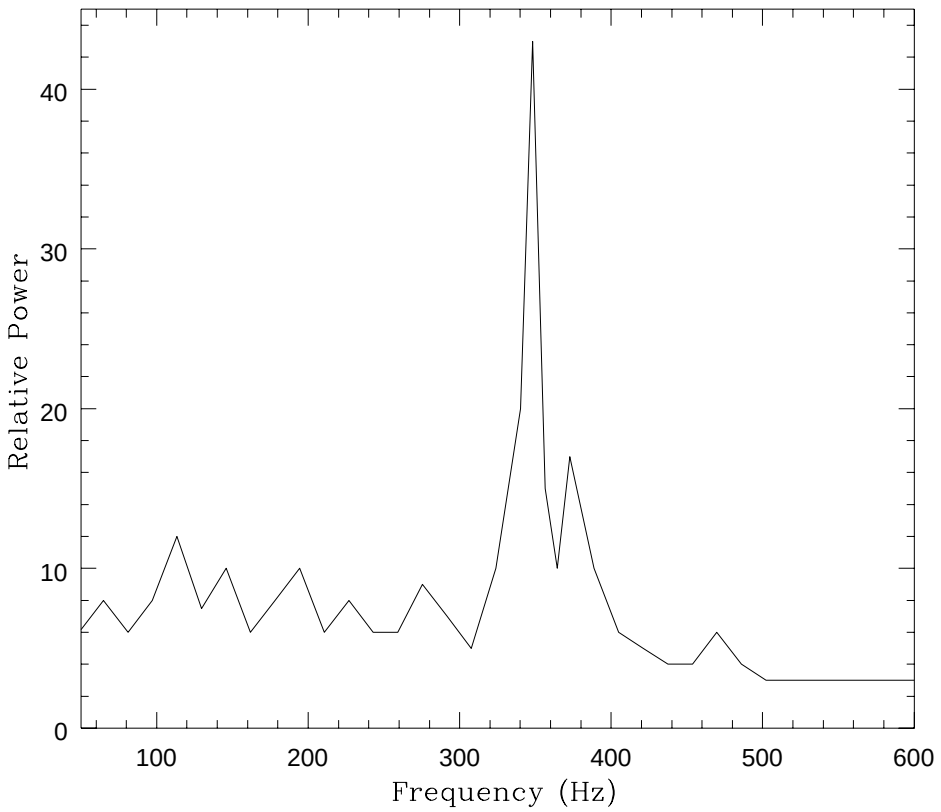

Figure 2.5: The spectrum analyser output at a chopping frequency of 350 Hz.

weight of the plate, on which the flat mirror is fixed, was optimized to give the required stability but not at the cost of the dampening the movement of the shaft too much.

When the system is well aligned, this angular set up gives almost a distortion free beam profile which greatly increases the photometric accuracies. We get accuracies of the order of ± 0.02 to ± 0.03 in the photometric magnitudes of a typical 3rd magnitude star in K with 1s integration. Accuracies of ± 0.01 have also been obtained on several occasions. Another interesting application of this angular chopper is the large sky throw ($\sim$ several arcminutes) achievable in the slow photometry mode. This helps in photometry of extended objects like comets (Chandrasekhar et al. 1996).

2.2 Data Analysis

The data analysis procedure adopted for detailed analysis of the occultation light curves is along the lines originally outlined by Nather & McCants (1970). The algorithm basically consists of the standard iterative non-linear least squares model fit of a theoretical light curve to the observed data. Another approach based on the same principles has also been tried out. In the following sections both these methods will be discussed in detail.

2.2.1 Non-linear least squares method

In this approach an *a priori* model of the one-dimensional brightness profile of the occulted source in the direction of occultation is assumed. In case of stellar sources which can be accurately described by a simple model of a circular disk, the brightness profile as given by Diercks & Hunger (1952) is

$$S(\phi) = I_0 \frac{\frac{2}{\pi}\left(1-(\frac{\phi}{\Omega})^2\right)^{1/2} + \frac{1}{2}\kappa\left(1-(\frac{\phi}{\Omega})^2\right)}{1+\frac{2}{3}\kappa} \tag{2.1}$$

where, 2Ω is the angular diameter of the star, I_0 is the intensity of the unocculted star and κ is the limb darkening coefficient. Now, the problem reduces to generating a model Fresnel diffraction pattern modified with the source brightness distribution and a set of scaling factors. Essentially, one has to run an iterative algorithm with five free parameters namely, the angular size of the source, the stellar intensity, the geometric time of occultation, the velocity component of the lunar shadow in the direction of occultation and the background light level. The aim is to obtain best estimates of these parameters simultaneously via a χ^2 minimization technique.

At any given instant of time t, the light curve of any stellar source occulted by the moon is the Fresnel diffraction pattern convolved with the source brightness profile and the instrumental averaging effects. The resulting light curve can then be written in the form

$$I(t) = \int_{-\infty}^{+\infty} d\phi \int_{-\frac{A}{2}}^{+\frac{A}{2}} d\alpha \int_{\lambda_1}^{\lambda_2} d\lambda \int_{-\Delta\tau}^{0} d\tau \; S(\phi)O(\alpha)\Lambda(\lambda)T(\tau)F(\omega) \; + \beta(t) \tag{2.2}$$

where, $F(\omega)$ is the diffraction pattern for a monochromatic point source, $S(\phi)$ is the assumed uniform disk brightness profile of the source along the direction of occultation, $O(\alpha)$ is the integrated area of the telescope mirror (including the central obstruction) along the direction of lunar motion, $\Lambda(\lambda)$ is the spectral response of the system, $T(\tau)$ is the time response of the detector and $\beta(t)$ is the time dependent background light level.

$$F(\omega) = 0.5[(0.5 + c(\omega))^2 + (0.5 + s(\omega))^2] \tag{2.3}$$

where $c(\omega)$ and $s(\omega)$ are the Fresnel integrals and ω is the dimensionless Fresnel number. The Fresnel number is given by

$$\omega = (\frac{2}{\lambda d})^{\frac{1}{2}}[v(t - t_0) + (d\tan(\phi)) + \alpha] \tag{2.4}$$

where, d is the distance to the moon, λ is the wavelength of observation, t_0 is the time of geometrical occultation, v is the velocity of the lunar shadow and α is the linear displacement term used to account for the averaging effect of the telescope. The effects of the functions $S(\phi)$, $O(\alpha)$, $\Lambda(\lambda)$ and $T(\tau)$ are to smear the monochromatic point source pattern. The modelling approach of each of these averaging effects is individually described below.

Finite source size

The finite size of the sources results in smearing the fringes. The larger the size, the greater is the smearing effect. As the angular diameter of the source increases,

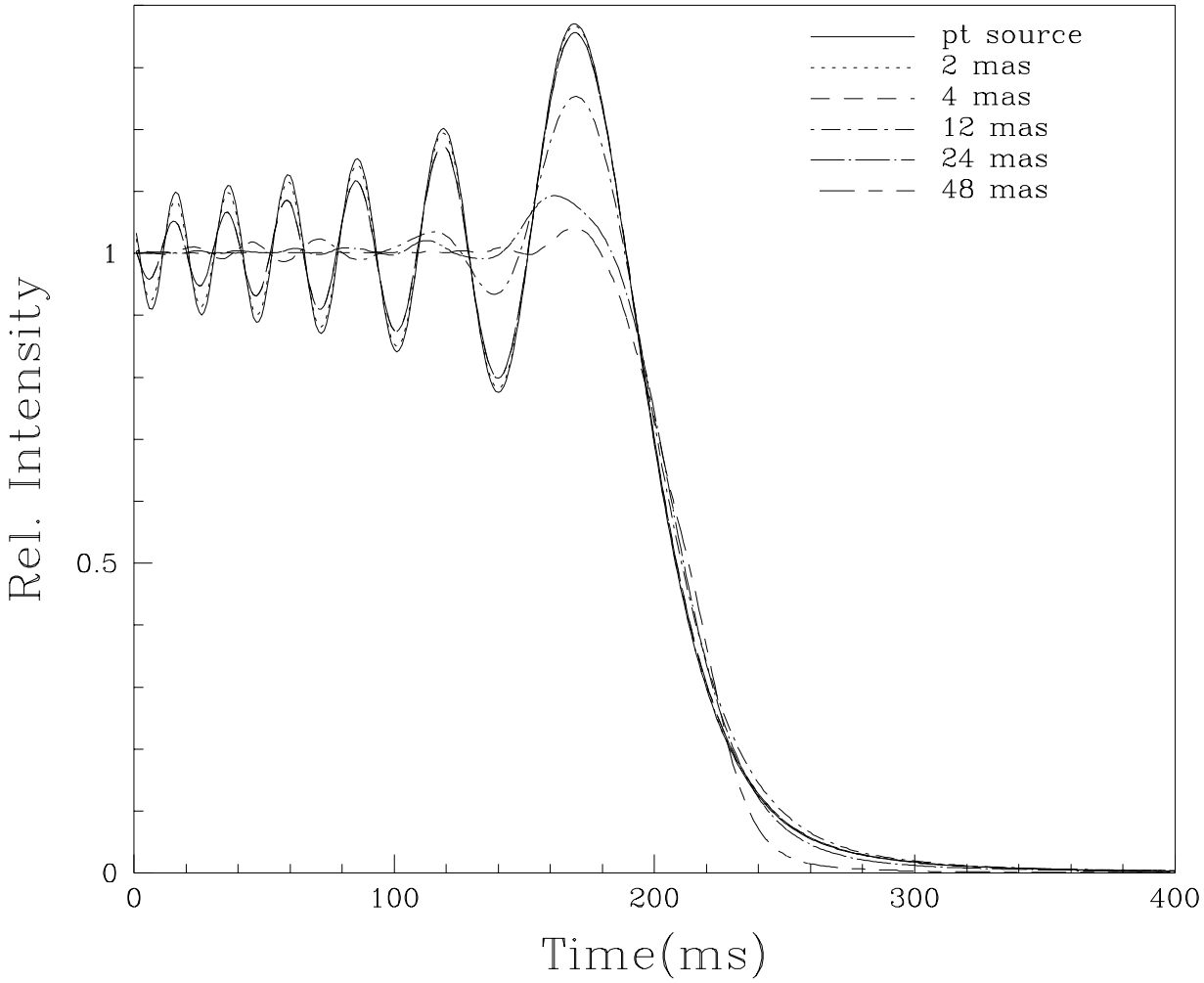

Figure 2.6: The simulated monochromatic curves at 2.2 μm for different source sizes. The velocity component of the lunar shadow here is fixed at 0.5 km/s.

visibility of the fringes decreases until for very large sources (> 40 mas), a purely geometrical curve results. Fig. 2.6 shows the simulated curves for monochromatic sources with different angular sizes. The method used here to model this effect was first suggested by Evans in 1952. The basic principle is that any extended source can be divided into equal strips parallel to the lunar limb. The lunar limb is assumed to be linear at the scale of tens of milli arcseconds. Fig. 2.7 shows the modelling aspect. Each strip then behaves, during the occultation, as though it were a centered point source whose intensity is weighted by the normalized area of the corresponding strip. The fringe patterns from all these point sources are then superimposed in the final tracing of the intensity variations. The integration in Eqn. 2.2 is performed numerically.

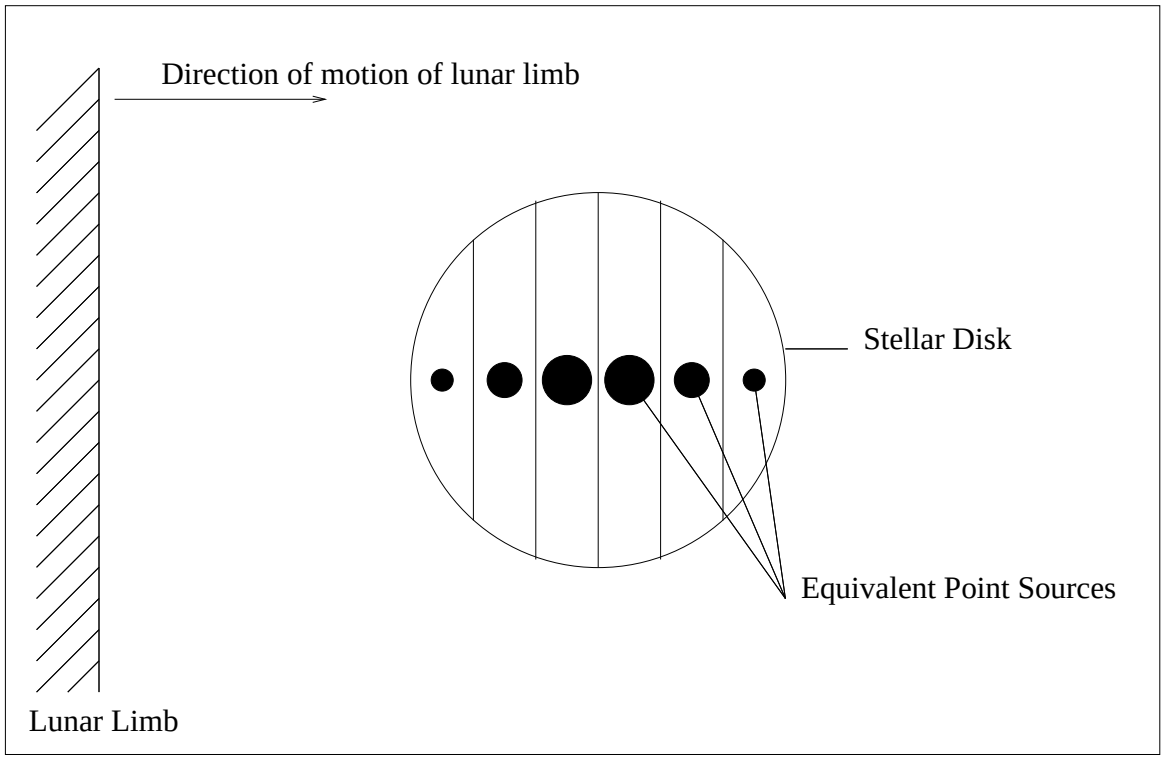

Figure 2.7: The modelling approach for the finite source size.

Slow detector time response

Amongst the three instrumental averaging effects, the finite time response of the system is a crucial factor. As has already been emphasized in Chapter 1 (Table 1.2), lunar occultation is a fast event ($\sim$ 200-300 ms) and hence the need for a fast sampling rate during data acquisition. The contact angle also plays an important role in deciding the time scale of the event. The effective time of fringe passage, as seen from the earth, will be lengthened by the factor $\sec(\beta)$, β being the contact angle. Grazing occultations are hence best suited for observations. For observations in the K band a sampling as fast as 1-2 ms is essential to obtain a proper light trace without losing any information. Data sampling is done at 1 KHz. For occultation observations one should ideally use detectors which have a flat response upto the cut off frequency set by the data sampling rate. But in our case, the detectors used do not have a flat response up to 1 KHz. This results in smearing of the fringes. This effect has to be accurately taken care of in the data analysis procedure and

for this the shape of the time response curve becomes important. It has to be determined experimentally after every event and this experimental response curve is convolved with the point spread function to account for this smearing effect.

Effect of filter bandwidth and system wavelength response

The system wavelength response has three components. The filter characteristics $f(\lambda)$, the wavelength response of the detector $l(\lambda)$ and the spectral energy distribution $b(\lambda)$ of the the star. The filter effect is due to the finite bandwidth of the broad band filter used in recording occultation events. The filter calibration curve is used to take care of this. The detector sensitivity is not limited to a single wavelength. Within the K band, the wavelength response of the InSb detector can be approximated by

$$l(\lambda) \propto \lambda \tag{2.5}$$

The spectral energy distribution of the source is assumed to be a blackbody distribution. The total wavelength response of the system is then given by

$$\Lambda(\lambda) = f(\lambda)l(\lambda)b(\lambda) \tag{2.6}$$

The integration over the required wavelength zone in Eqn. 2.2 is replaced by a summation and is carried out numerically.

Effect of telescope size

An occultation observation is the record of the details of the lunar shadow cast by the star as it passes across the telescope aperture. The telescope aperture averages out the diffraction pattern. This effect is very nominal ($\sim$ 0.2 mas) for a 1m class telescope but a larger aperture ($\sim$ 4m) smears the light curve to a great extent and hence this should be carefully taken care of in the data analysis procedure. The modelling approach adopted to account for this effect is similar to the one used for the finite size of the source. Here, the telescope aperture is considered as consisting of a series of slices aligned in the direction of the shadow passage. The

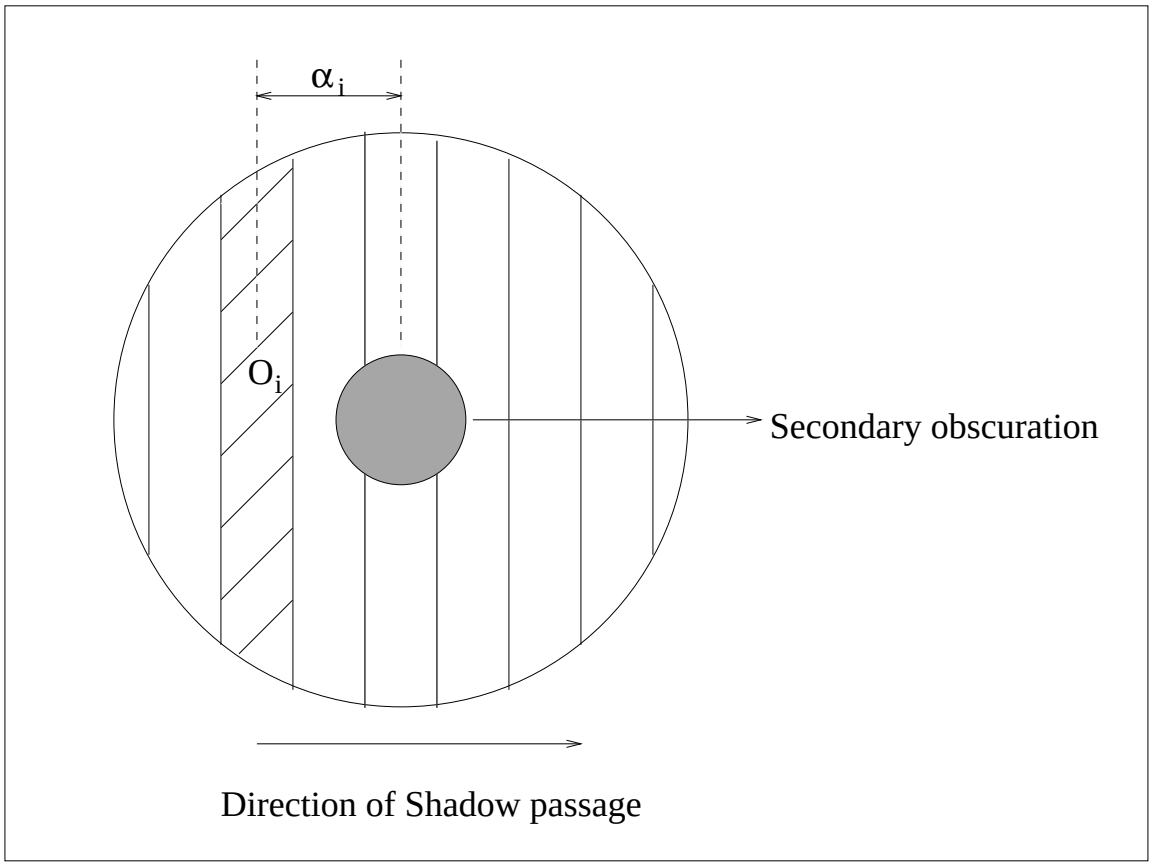

Figure 2.8: The modelling approach of the telescope aperture.

occultation pattern will then be seen by each slice at a slightly different time as the shadow sweeps past the telescope. In case of Cassegrain reflectors the secondary obscuration is also taken into account. The model is shown in Fig. 2.8. The function $O(\alpha)$ takes the form

$$\begin{aligned} O(\alpha) &= [1-(\frac{\alpha}{T_p})^2]^{\frac{1}{2}} - [1-(\frac{\alpha}{T_s})^2]^{\frac{1}{2}} \quad for \quad \alpha \leq T_s \\ &= [1-(\frac{\alpha}{T_p})^2]^{\frac{1}{2}} \quad for \quad T_s \leq \alpha \leq T_p \end{aligned} \tag{2.7}$$

where, T_p and T_s are the radii of the primary and the secondary mirrors of the telescope. Like in the other averaging effects, this integration is also performed numerically.

Varying background light

In occultation light traces often we encounter a varying background light level, which depends on many factors, like the lunar phase, position angle of observation, position angle of the lunar terminator, atmospheric condition, presence of aerosols and other particulate matter, air mass and the wavelength of observation. Hence, it is event dependent. Modelling this parameter is not trivial and can be best approximated by a polynomial series. However, a slowly varying background can be determined observationally from portions of the light curve. The model parameter has the form

$$\beta(t) = \sum_{i=0}^{n} a_i x^i(t) \tag{2.8}$$

The degree of the polynomial is decided by the nature of the individual light curves. Usually, a simple slope with $i = 1$ is sufficient but there are cases where one has to use higher order polynomials to account for the variation in the background signal. Nevertheless, care is taken to ensure that the nature of the polynomial does not change abruptly in the event portion.

Scintillation noise

The occultation light curve, as recorded, is not the Fresnel fringe pattern, which originates at the lunar limb, but is affected by turbulence in the Earth's atmosphere. The time scales involved in occultations are such that the atmosphere can be considered generally to be frozen in this time frame. But, it has been seen that it does affect some of the light curves. The fluctuations seen in the light traces are due to rapid scintillation effects, which is severe for bright stars, variations in atmospheric transmission due to thin passing clouds etc. It is seen that for bright stars ($m_k \leq 0$) the scintillation effects dominate.

Knoechel & von der Heide (1978) have also shown from theoretical simulations that the presence of scintillation noise tends to bias the angular diameter estimation to a large extent. In order to get a statistically correct estimate of the angular

diameter, this effect has to be taken into account in the data analysis. The modelling aspect for both the cases described is the same. The fluctuations involved in occultation light traces are best modelled by a sum of orthogonal (Legendre-) polynomials. This is because low frequencies dominate the trace and the essential part of typical length of a lunar occultation light curve is well represented by a linear slope. After disappearance or before reappearance of the source the scintillation noise vanishes. To account for this, Richichi et al. (1992) have suggested the use of a dampened low-frequency term to ensure a more stable solution. Both the terms come as multiplicative factors in the Eqn. 2.2. The normalized Legendre polynomial has the form

$$L'(t) = \left[1 + \sum_{i=1}^{m} b_i L_i(t)\right] \tag{2.9}$$

and the damping term has the form

$$\begin{aligned} \rho(t) &= 1 \qquad when \qquad t \leq t_0 \\ &= I(t) - \beta(t) \qquad when \qquad t > t_0 \end{aligned} \tag{2.10}$$

Care is taken in using this polynomial because by increasing the order of the polynomial, the fit becomes better but it may give some spurious results. The nature of the polynomial should be carefully studied during the event time and there should not be any abrupt change and also it should not start taking the shape of the fringe pattern.

2.2.2 Alternate approach of data analysis

The basic principle is the same. Here, we take care of the smearing effects in a different way. Instead of generating the Fresnel diffraction pattern and carrying out the integration given in Eqn. 2.2 involving the different functions explained in the previous section, here we choose the point source pattern from our data sample. IRC+10032 is a point source and the best fit to this data with the non linear least squares fit is taken as the point source function. This is shown in Fig. 2.9. This is a point source which is inherently convolved with the telescope function, the

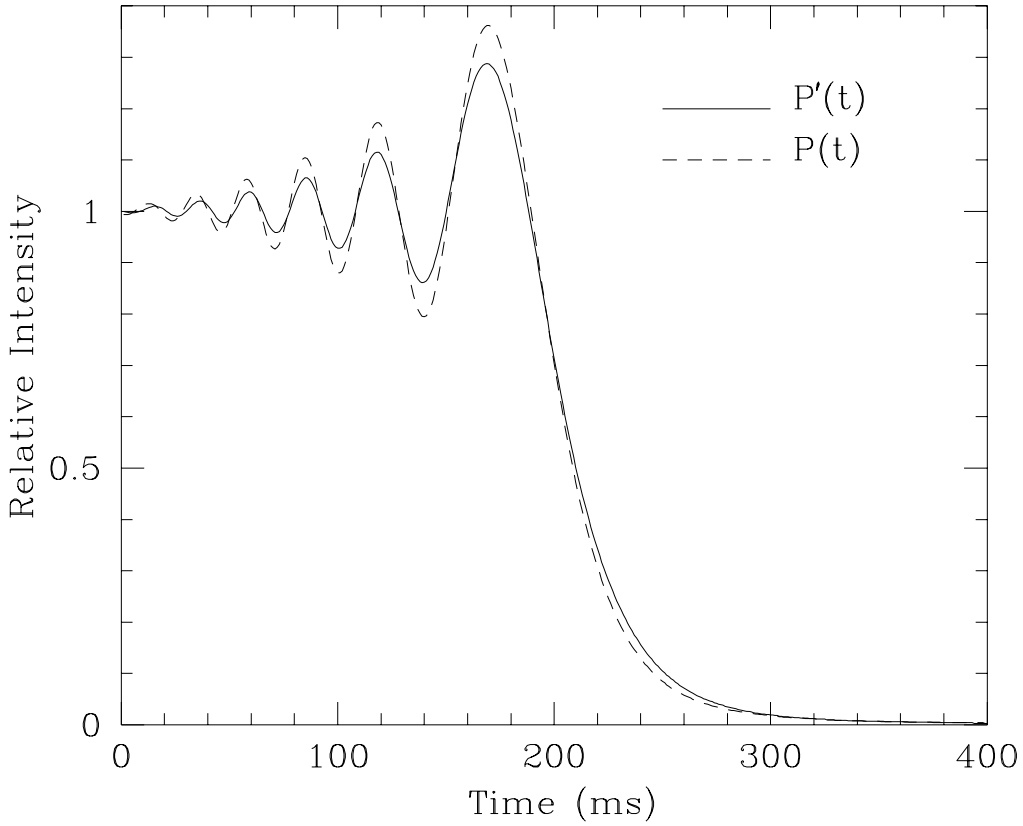

Figure 2.9: The observed point source curve $P'(t)$ and the time response deconvolved curve $P(t)$.

filter bandwidth curve, the time response for this particular event and the x-axis is scaled to the velocity component of the event. Let us denote it as $P'(t)$.

The time response curve $T'(\tau)$ for the occultation event of IRC+10032 is shown in Fig. 2.10. To remove the averaging caused due to the system time response we deconvolve $T'(\tau)$ from $P'(t)$, i.e.,

$$P'(t) \oplus T'(\tau) = P(t) \tag{2.11}$$

where, $\oplus$ denotes deconvolution and $P(t)$ is now the basic point source function which is used as the starting function for the analysis of the light curves. Fig. 2.9 shows the curve $P(t)$. In our case, the telescope and the system used are same for all the occultation observations and hence, the averaging effect due to these two instrumental factors will be identical in all the light curves. So, one doesn't need to account for these in the data analysis. This is the key point in this method of analysing the data.

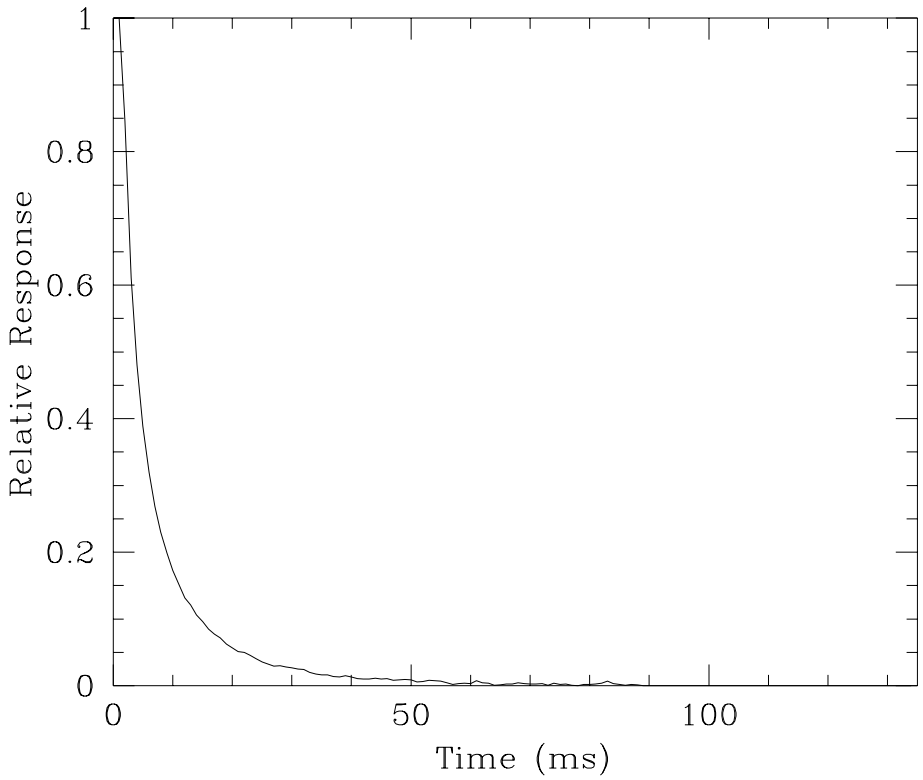

Figure 2.10: The time response curve for IRC-10032.

To obtain the diameter information of a source, we need the time response curve $T(\tau)$ of the particular event. We can generate the source profiles ($S(\phi)$) using Eqn. 2.1. $I(t)$ is given by

$$I(t) = P(t) * T(\tau) * S(\phi) \tag{2.12}$$

where, $*$ denotes convolution. To get a best fit to the observed data one has to change the angular size and scale the x-axis to account for the velocity. The validity of this approach has been extensively tested on the light curve of IRC-20563 and the value obtained from this technique was consistent with that estimated from the non linear least squares method.

2.3 *Laboratory Calibration of the system*

The main objective of this calibration is to determine the response of the detector to an instantaneous change in the light level. A simple but effective experimental set up is used. Fig. 2.11 shows the block diagram of the set up.

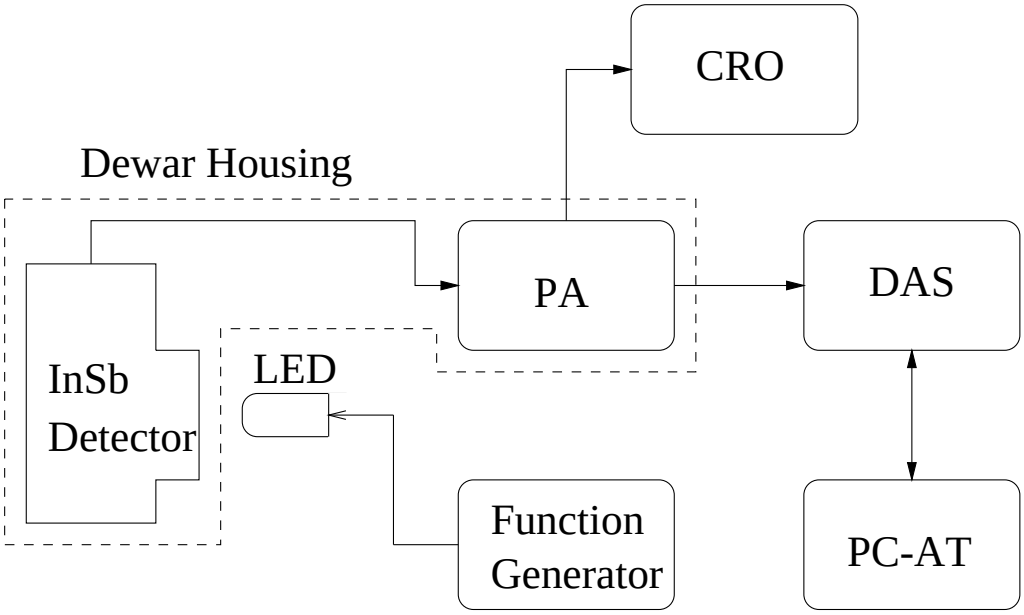

Figure 2.11: The block diagram for the experimental set up for system calibration.

An IR light emitting diode (LED) is placed in front of the dewar window in a fashion suiting the fact that it is a front looking one. A square pulse is fed to the LED from a function generator. Care is taken to choose LEDs with fast time response. This was verified by operating dewar D1 in the low R_f mode and sampling at 0.1ms. The transition of LED on/off is experimentally found to be $<$ 0.1ms. This ensures that the LED response does not interfere in determining the detector response.

It was found that there is no unique response curve for the entire operating zone of the detector and that the response curve is sensitive to the bias voltage given to the preamplifier. The following calibrations were performed to study the behaviour of the time response over the dynamic range of the detector.

2.3.1 *Time response calibration*

In the InSb dewar, the preamplifier output was adjusted to zero by moving the bias potentiometer. A fixed square pulse of frequency 2 Hz was fed to the LED from the function generator. The peak-to-peak (p-p) value of the preamplifier output was set to 1 volt by adjusting the output of the function generator. After fixing these levels, care was taken to maintain the mechanical stability of the LED throughout the course of the experiment. This is essential to avoid any change in the signal level due to misalignment of the LED. The K filter and 2mm (26 arcsec in the sky) aperture were chosen to mimic the occultation events. The bias voltage was varied from 0.1V to 2.1V in steps of 0.1V for the fast dewar and varied from 4.4V to -2.8V in steps of 0.4V for the CVF dewar. The preamplifier output was recorded using the same data acquisition system which is used for recording occultation events. Data sampling was done at 1 KHz. Four pulses from each data set were chosen. The response curve was extracted from each pulse. The mean of these four were taken and normalized to give the time response curve for the particular bias position. This averaging takes care of the spread or noise in each data set. Fig. 2.12 shows the actual data and the exponential fit to it. As is clearly seen the time response does not follow the exponential curve. Figs. 2.13 and 2.14 show a sample of the time response curves for Dewar 1 and Dewar 2 respectively covering the entire range. As seen, they are spread over a wide range of values being critically dependent on the bias level. Data sets contaminated with saturation effects at both the ends of the dynamic range were discarded. Table 2.3 and Table 2.4 list the time constant values as a function of the bias voltage for the two dewars.

Fig. 2.15 shows the signal amplitude as a function of the bias voltage. It is seen that it increases, reaches a maximum and then decreases again. This clearly indicates the gain variability of the detector over the dynamic range. The time response also follows the same trend.

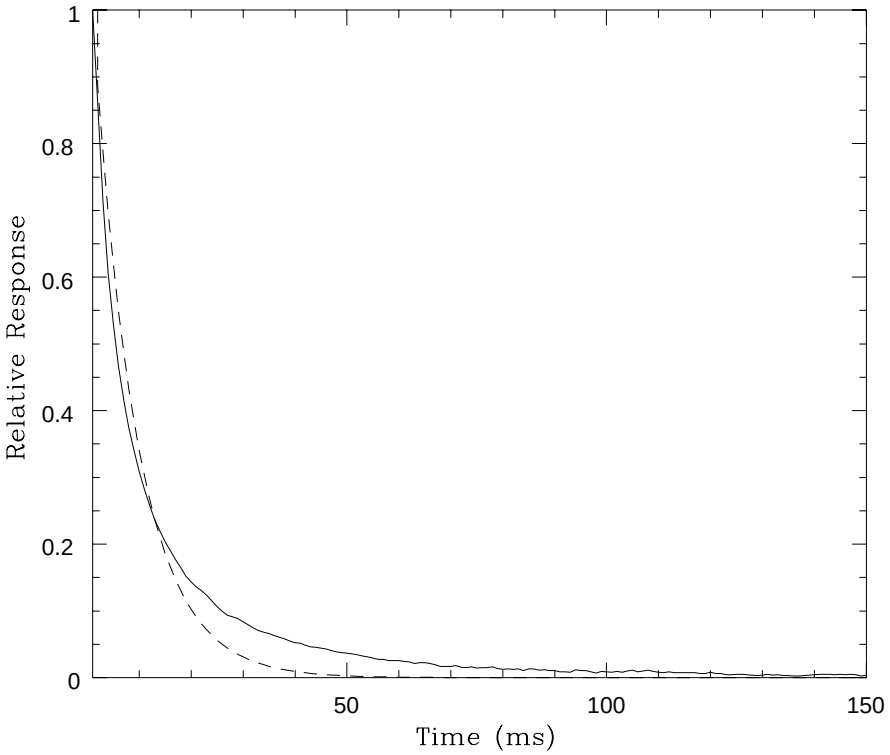

Figure 2.12: The actual time response (solid line) and the exponential fit to it (dashed line).

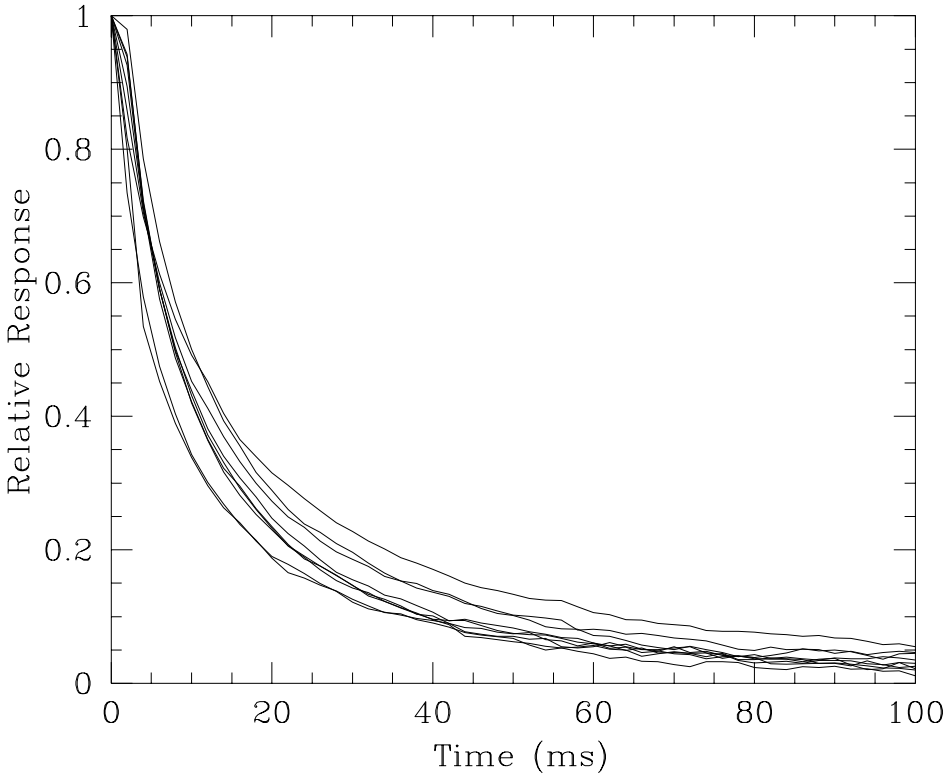

Figure 2.13: The time response curves over the dynamic range of the Fast Dewar.

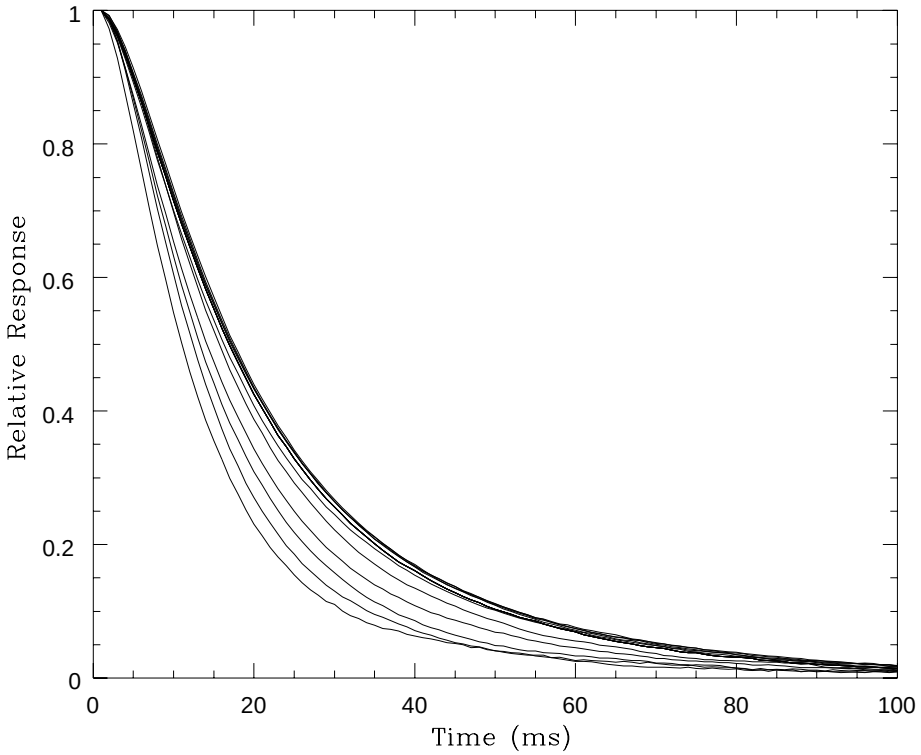

Figure 2.14: Same as in Fig. 2.13 but for the CVF Dewar.

2.3.2 *Gain variability of the Detector*

To establish the gain variability aspect the experiment was repeated at a higher sensitivity level with a (p-p) voltage of 0.3V. A similar trend was seen. Mostly, our operating zone is between base levels of 30000 and 45000. To get a variability curve in this region, the experiment was done with a (p-p) voltage of 1 volt and the base level varying between 30000 to 42000 in steps of thousand. This is same as varying the bias voltage. Fig. 2.16 shows the variability curve and the straight line fit to it. With reference to Fig. 2.15 the bias voltage covered for Fig. 2.16 is the portion from 1.6V and beyond. This non-linearity affects the observations of bright stars and it has to be corrected. Fig. 2.17 shows the data of IRC-20563 ($m_k = 0.79$) and also the data after correcting for the variation in the gain. The angular size value obtained without the correction was 4.8 mas and after correcting for the gain variability it is 4.4 mas.

Table 2.3: Time constants with bias voltages for Dewar 1.

Bias Voltage (volts)	Time constant range (ms)
0.3	5.5
0.4	5.5
0.5	5.5
0.6	6.5
0.7	6.5
0.8	6.5
0.9	7.5
1.0	7.5
1.1	7.5
1.2	7.5
1.3	8.5
1.4	8.5
1.5	8.5
1.6	9.5
1.7	8.5
1.8	7.5
1.9	6.5
2.0	5.5

2.3.3 *Corollary Experiments*

1. The sensitivity of the LED used is found to be very poor in the L band probably due to envelope absorption. The difficulty arose in determining the time response of the R Leo event recorded at 3.36 μm. However, it was experimentally determined that the time response of the system is independent of the filter used. Fig. 2.18 shows the time responses in the JHK bands with the levels being same in all. Within measurement errors, the curves are identical. Hence, a K band time response curve was used for the analysis of the light curve of R Leo.

2. In this experiment an additional LED is placed near the first one. A constant adjustable dc voltage is supplied to it from a regulated power supply. Let us refer to it as the background LED.

Table 2.4: Time constants with bias voltages for Dewar 2.

Bias Voltage (volts)	Time constant range (ms)
4.4	22.5
4.0	22.5
3.6	22.5
3.2	23.5
2.8	23.5
2.4	23.5
2.0	23.5
1.6	23.5
1.2	23.5
0.8	23.5
0.4	23.5
0.0	23.5
-0.4	21.5
-0.8	20.5
-1.2	18.5
-1.6	17.5
-2.0	16.5
-2.4	14.5

First the preamplifier output is brought to zero offset level. The preamplifier output is then adjusted to 1V by supplying the required dc voltage to the background LED. A square pulse of frequency 2 Hz is fed to the other LED. Let us refer to this as the pulsating LED. The (p-p) voltage of the preamplifier output was set to 1V for this square pulse. The time response curve was recorded. Now, the background LED was removed and the dc offset of 1V was given by changing the bias voltage and the time response was recorded. It is seen that the time response is the same for both the cases. This implies that the background level can be set eiter by moving the bias potentiometer (which means changing the bias voltage) or by adjusting the light level from the background LED. The time responses for both the cases are shown in Fig. 2.19.

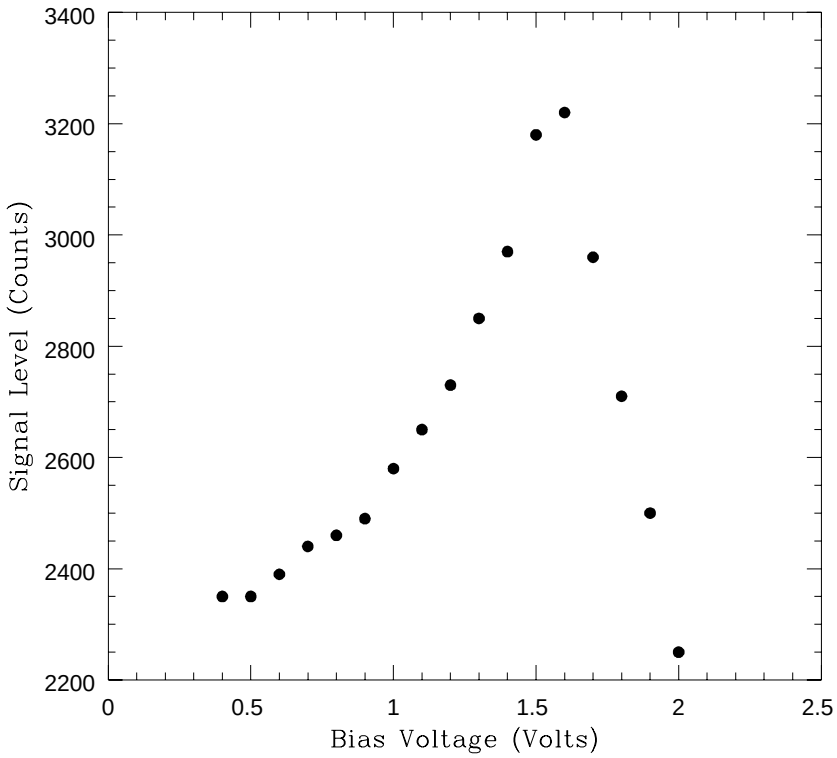

Figure 2.15: The signal level as a function of the bias voltage.

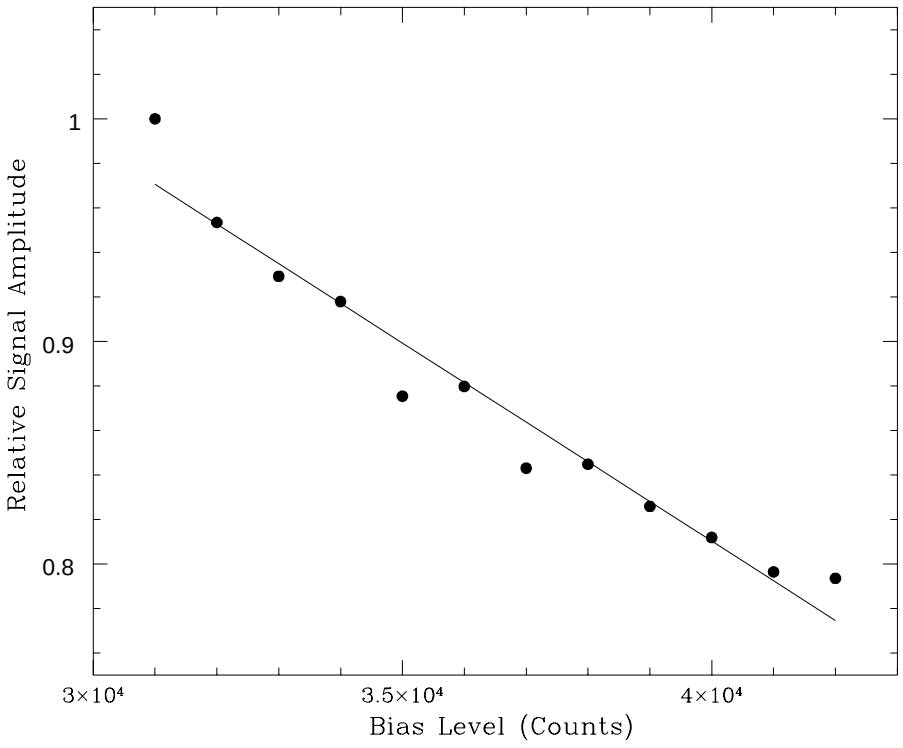

Figure 2.16: The relative signal amplitude as a function of the bias level. The solid line denotes the linear fit to the data.

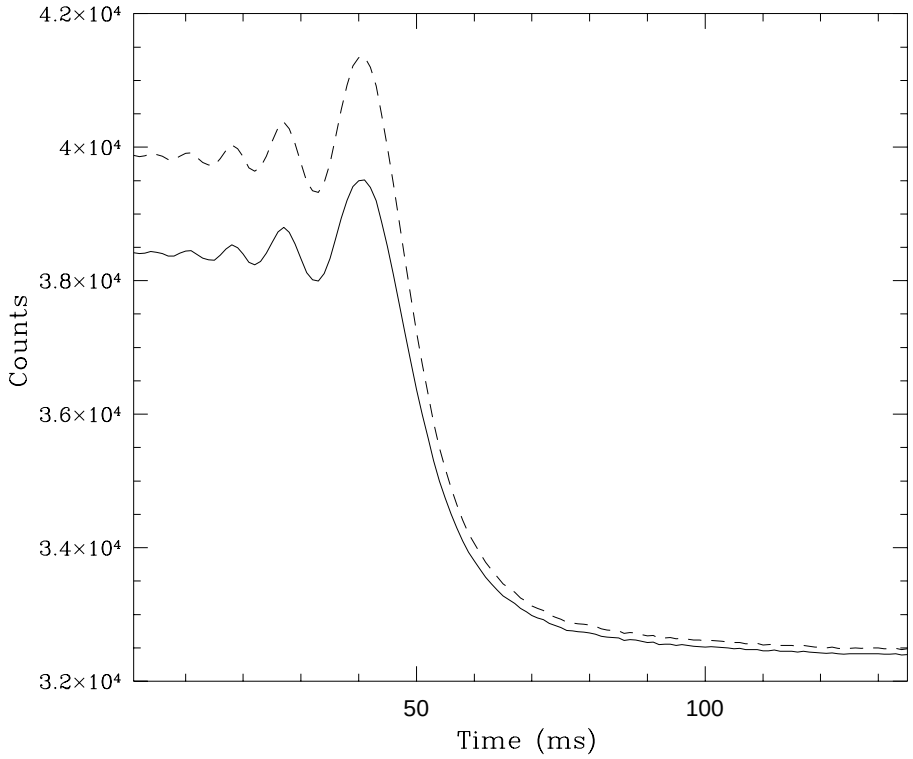

Figure 2.17: The original light curve of IRC-20563 (solid line) and the corrected light curve (dashed line).

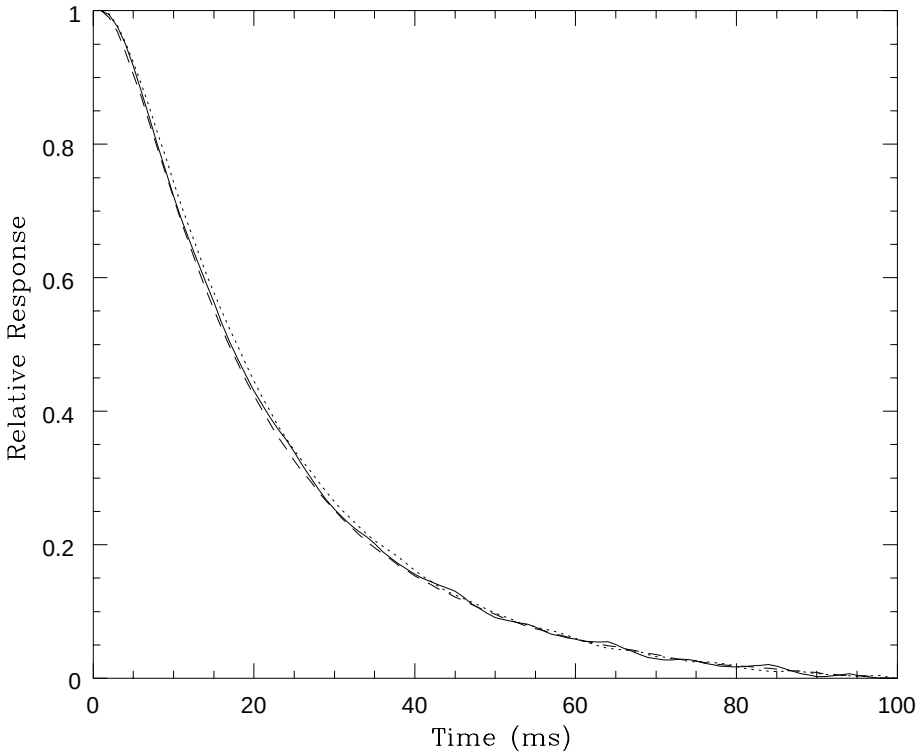

Figure 2.18: The time response curves in all the three JHK filters.

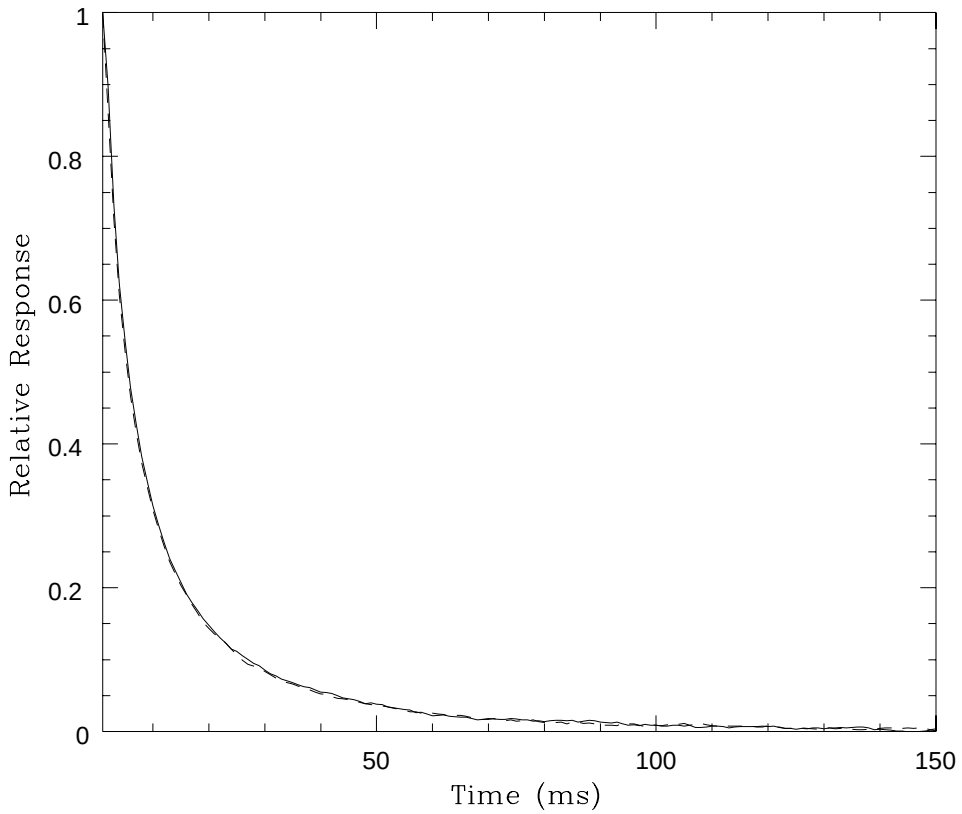

Figure 2.19: The time response curves for (i) offset set by the background LED (solid line) and (ii) offset set by adjusting the bias voltage (dashed line).

3. In this experiment only the pulsating LED is used. A similar square pulse is given. Maintaining the base level same, the preamplifier output was adjusted to a p-p voltage of 2 volts, 4 volts and 6 volts respectively and the time response curve was obtained in each case. As is seen clearly from Fig. 2.20 the time response curve remains essentially the same if the base level is constant, irrespective of the strength of the square pulse.

During any occultation event the bias voltage has to be properly adjusted to take care of the lunar background as the moon moves nearer to the aperture. This ensures that the system does not go into saturation. We have already noted that the time response curve is very sensitive to the bias voltage applied. This demands that the time response of the system should be measured immediately after every event with exactly the same setting of the bias level ensuring the same background level. This has thus become a regular feature of the observing schedule.

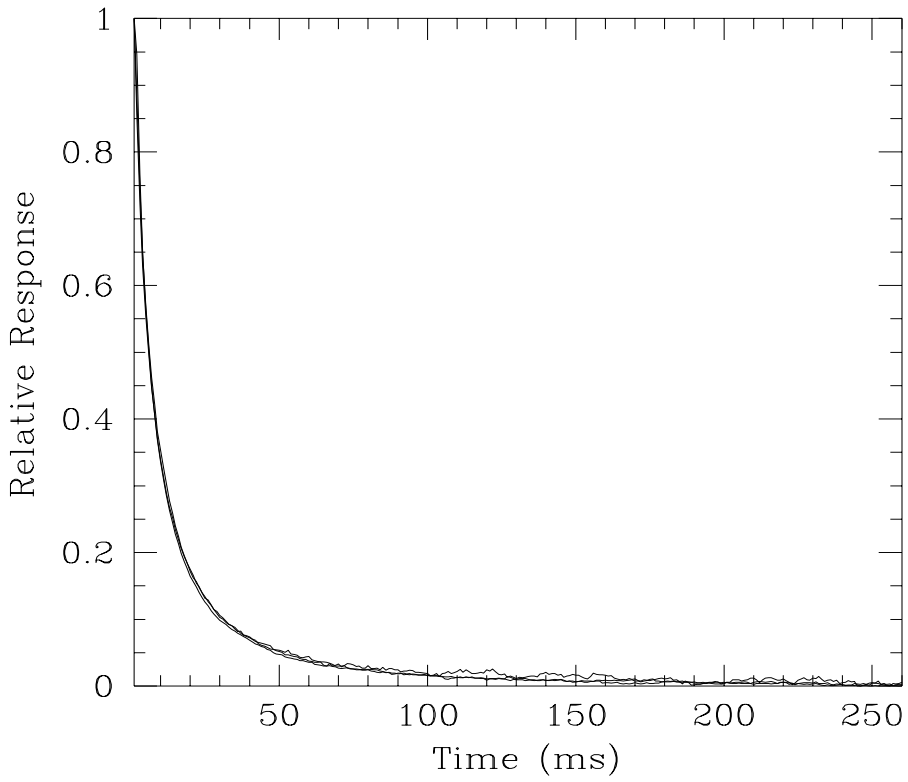

Figure 2.20: The time response curves for signal levels of 2 volts, 4 volts and 6 volts.

2.4 Remarks

In this chapter, we have described the instrument used for observations and the experiments done for system calibration. The principles of data analysis and the two algorithms used for the same have been explained in detail. In the following chapters we give the results obtained and discuss their importance in understanding the nature of late type stars.

Chapter 3

Mira variable R Leonis and bright IR source IRC-20563

3.1 Introduction

The high mass loss phase has been identified with long period variables (LPVs), OH/IR stars, cocoon stars and dust - gas envelope stars evolving along the AGB. They occupy a thin unstable strip at the tip of the AGB in the HR diagram where they undergo thermal pulsing (helium shell flashes). Observations reveal that a common feature of these late type stars is the occurrence of stellar pulsations with a typical period of $\sim$ 1 year. Studies of Mira variables are of considerable importance in stellar astrophysics as these are pulsating stars which enter a short-lived (2×10^5 years) phase during which they rapidly lose mass (10^{-7} – 10^{-6} $M_\odot yr^{-1}$). During a variability cycle which is typically 100 – 500 days, these stars undergo significant changes in their observable properties. An interesting implication of these pulsations is the intrinsic variation of the angular size of the source. This may be due to the shock waves generated in the stellar interior which may cause the photosphere itself to move in and out. Recent interferometric observations by Burns et al. (1998) and Tuthill et al. (1995) have shown variation in the angular diameters of Mira type variables. Tuthill et al. (1995) report from optical interferometric measurements the detection of a large and systematic increase in the angular diameter of the long period Mira variable *o* Ceti. The diameter increase

over a 25 month period was as much as 85 %. They have explained the large increase in the stellar size observed by them to be due to mass loss induced by an aperiodic shock propagating through the stellar atmosphere. Burns et al. (1998) find a cyclical increase in the angular diameter of R Leonis by 35 %. Richichi et al. (1988) have discussed the large variation in the size of RX Cnc - a M8 giant. While considerable amount of data exists in literature for photometric and spectroscopic studies of long period variables, HAR data for all these objects is still scarce, and mostly restricted to a few well known sources. Accurate determination of the sizes and shapes of these variables and the temporal variations of these quantities have the potential to resolve problems pertaining to the detailed atmospheric structure, mass loss, evolution and pulsational properties. Mira type variability is believed to be due to instabilities which are the direct manifestation of stellar pulsations. The mode of pulsation is still an unresolved problem (Haniff et al. 1995, Tuthill et al. 1994, van Belle et al. 1996) which calls for sustained HAR observations. The atmospheres of Mira variables are very deep and effective diameters change markedly with wavelength due to opacity effects of molecular absorption bands like TiO. These strong TiO features contaminate the optical pass bands. Hence, it is difficult to sample the true continuum in optical observations, even if narrow band filters are used. In contrast, at selected IR wavelengths, especially with small bandpasses, the true continuum can be sampled. Multiwavelength HAR observations can also be used to investigate the strong wavelength-dependent variation of angular size (Haniff et al. 1995, Tuthill et al. 1995, Labeyrie et al. 1977). In this chapter we discuss the HAR observations of R Leonis and IRC-20563.

3.2 Mira Variable R Leonis

R Leonis is one of the brightest and well studied oxygen-rich Mira variables, especially in the near infrared as its energy distribution peaks in this spectral region. The proximity of this source has made it a suitable target for HAR observations. Table 3.1 summarizes the important parameters of this source. Two occultations

Table 3.1: Source parameters of R Leo.

Parameter	Value	Reference
Spectral Type	M6.0 - M9.5IIIe	1
Period	309.95days	2
Initial Epoch	JD 2450747	2
V(max,min)	4.4, 11.3	3
3.5 μm(max,min)	-3.23, -2.68	4
2.2 μm(max,min)	-2.6, -2.3	5
m_b	0.69	6
Distance	114 $\pm$14pc	6

References: (1)Danchi et al. (1994);(2)J.Mattei 1998, private communication;(3)Kukarkin et al. (1969);(4)Forest et al. (1975);(5)Gezari et al. (1993);(6)van Leeuwen et al. (1997)

of this source were observed in collaboration with Dr. Andrea Richichi and Dr. Sam Ragland of Osservatorio Astrofisico di Arcetri, Italy. Observations were carried out at 3.36 μm with a narrow bandwidth of 0.05 μm at Gurushikhar and in the standard K band at 2.2 μm from Calar Alto Observatory. The two events are separated by a time difference of 82 days, which is a significant part of the 310 day period of variability of this source. Hence, phase dependent variation in the size can also be investigated. Recent optical and NIR interferometric observations of R Leo also permit a comparison of the angular diameter values determined by interferometric and lunar occultation techniques.

3.2.1 Observations

A reappearance lunar occultation of R Leo was successfully observed on 19 December 1997 at 3.36 μm (event 1) at the 1.2m telescope at Gurushikhar, Mt. Abu. Observations were taken in the transmission channel of the recently developed

two channel IR photometer using a LN_2 cooled InSb detector dewar. It is an extension of the photometer described in Chapter2. The details of the instrument can be found in Mondal et al. (1998). The use of a CVF permitted a narrow bandwidth with a full width half maximum (FWHM) of $\sim 0.05\,\mu$m at $3.36\,\mu$m. Event details and other observing parameters are listed in Table 3.2. The occultation event was

Table 3.2: Event details and other observing parameters for the two events of R Leo.

Details	Event 1	Event 2
Date	1997 Dec 19	1998 Mar 10
Time(UT)	00h 17m 42s	20h 33m 30s
Position Angle	305.39^o	121^o
Contact Angle	189.2^o	14^o
Predicted Velocity Comp.(km/s)	0.6036	0.6530
Altitude(star)	68.4^o	51^o
Lunar phase (days after new moon)	18.85	13.44
Variability Phase	0.17	0.44
Data sampling rate	1ms	2ms
Diaphragm (arcsecs)	26	14
Filter $\lambda/\Delta\lambda$ (μm)	3.36/0.05	2.36/0.46

sampled at one millisecond. The observed light curve was contaminated with 50 cycle modulation from the mains power line. This dominant frequency component was effectively filtered out from the light trace using one of the two techniques mentioned below. The first one is a simple method where a twenty point running average is taken of the data to give a smooth curve. In the absence of any fringe pattern in the occultation trace, this method is quite accurate. The other approach involves a FFT of the data set. The 50 cycle pick up shows up as a spike with a finite width in the power spectrum. This is component is manually filtered by removing both the real and the imaginary part of the Fourier coefficients corresponding to

this feature in the Fourier domain. Then the filtering is done by taking an inverse FFT of the modified data set. Both the methods give consistent results. Fig. 3.1 shows the filtered data. The dominant noise in the data is mainly due to scintillation which is due to poor sky conditions prevailing during the observation and residuals if any after the 50 Hz filtering.

Nearly three months later, on 10 March 1998 a disappearance event of R Leo occurred at Gurushikhar but was unfortunately clouded out. However, this same event (event 2) was successfully observed at the 1.23m telescope at the Calar Alto observatory (2^o 32′ 12″.0 W, 37^o 2′ 42″.2 N; 2168m). This event was recorded in a standard broad band K filter with FIRPO – a fast photometer extensively used for lunar occultation work (Richichi et al. 1996b). The observing conditions were not ideal and the event was recorded through thin clouds. Nevertheless, the quality of the data is sufficient to achieve $\pm$2 mas accuracy in the derived angular size. The light curve also suffers from the effect of detector non-linearity, R Leo being too bright in the near infrared. This non-linearity in the FIRPO system has been discussed in Richichi et al. (1994a). It manifests itself only in connection with sudden changes of the signal, causing an overshoot in the signal drop followed by an asymptotic recovery to the correct level. In our case, this effect caused some distortion in a small portion of the light curve after disappearance (well away from the diffraction fringes) at the level of $\sim$ 5% of the stellar brightness. This effect has been carefully taken into account in the data reduction procedure in order to avoid any systematic bias in the angular diameter estimation. Fig. 3.2 shows the light curve for event 2. The details of this event are also given in Table 3.2. In addition, near infrared photometry was carried out one day before event 2 at the TIRGO 1.5m telescope using the facility photometer FIRT (Richichi et al. 1996b). The JHK magnitudes obtained are -0.50$\pm$0.05, -1.77$\pm$0.05 and -2.49$\pm$0.05 respectively. The phase calculation of R Leo in this work is based on the initial epoch and the period information obtained from American Association of Variable Star Observers (AAVSO, Mattei 1998).

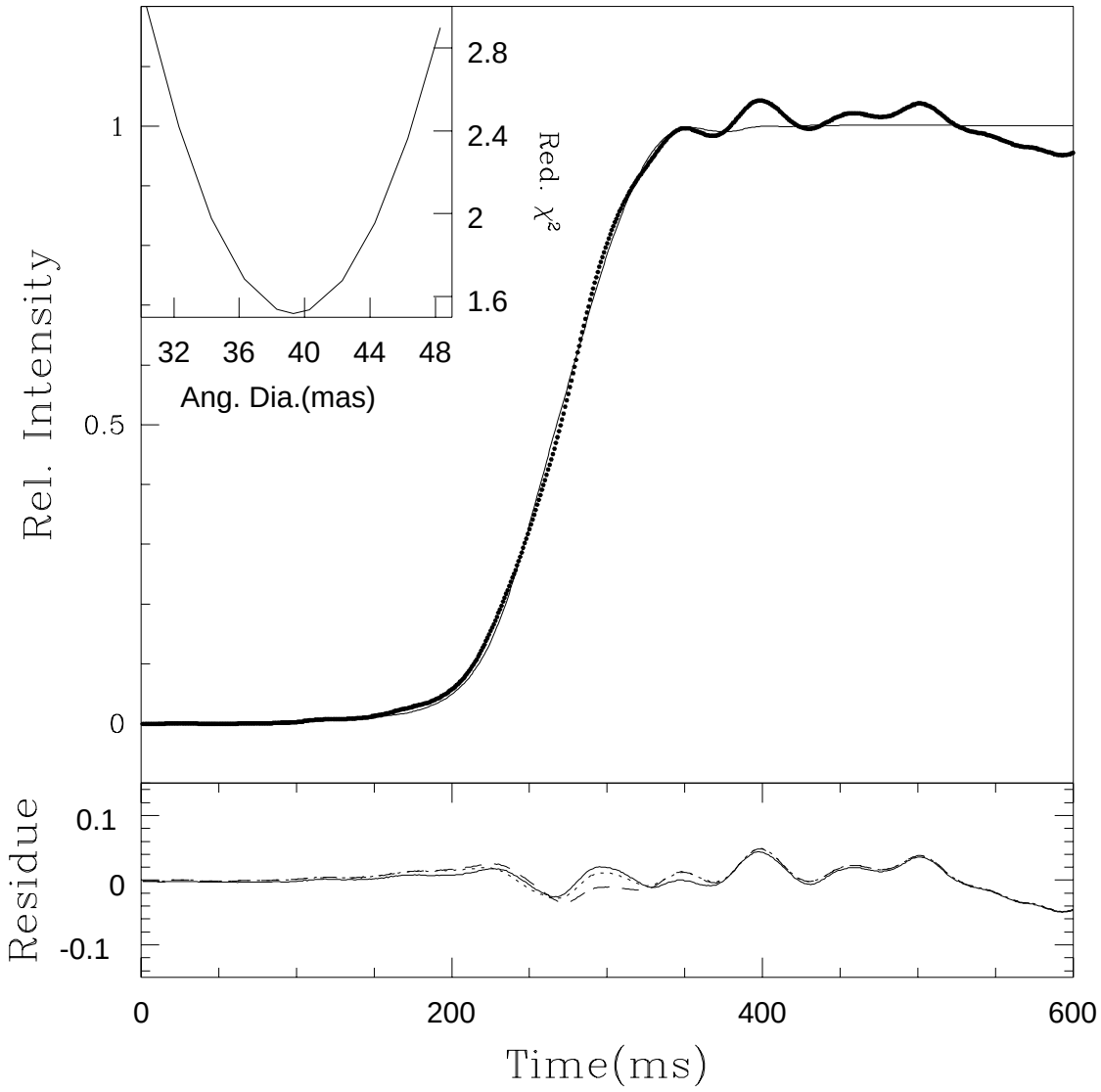

Figure 3.1: Occultation light curve of the reappearance event. The data (dots) and the uniform disk model fit to it (solid line). The inset shows the convergence of χ^2 to the minimum at 39 mas.

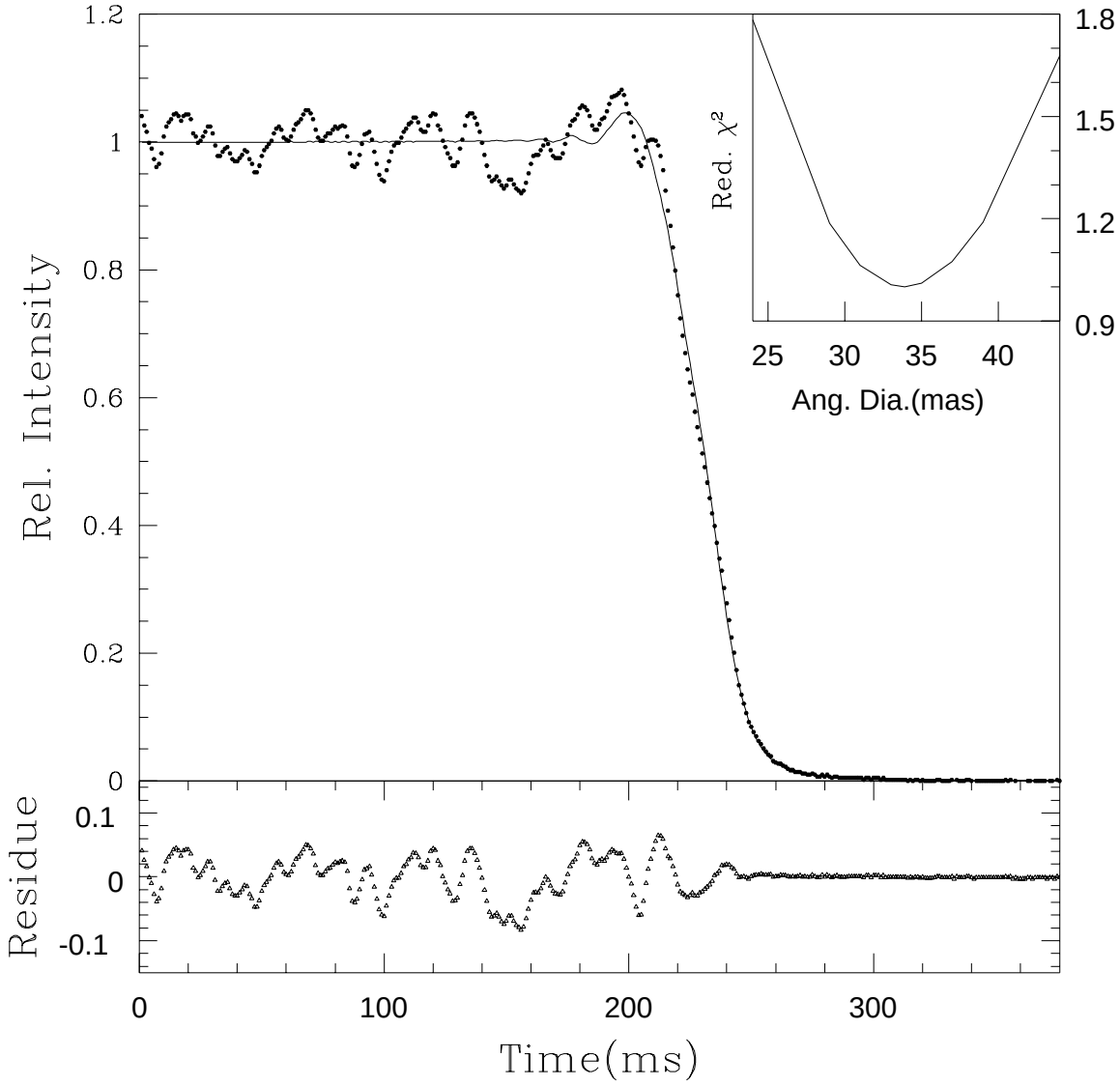

Figure 3.2: Occultation light curve of the disappearance event. The data (dots) and the uniform disk model fit to it (solid line). The inset shows the convergence of χ^2 to the minimum at 34 mas.

3.2.2 *Previous High Angular Resolution Observations*

High angular resolution observations over a wide spectral range are available for R Leo. They include direct observations by lunar occulations and optical interferometry and indirect estimations from colour temperature, model atmosphere etc. A detailed survey of the available literature was done and is discussed below.

It is interesting to note that the earliest estimate of the angular size of R Leo was given by Pettit & Nicholson (1933) from radiometric observations. They gave a value of 63 mas at the visual variability phase of 0.3. Neugebauer et al. (1973) had observed lunar occultations of R Leo in the three infrared bands of 3.5, 4.8 and 11 μm. The values quoted by them are 50 mas for the first two wavelengths and 300 mas for the 11 μm observations. In the absence of any published light curve it is not possible to comment on the accuracy of these values except that it agrees well with the source scenario of circumstellar dust which overwhelms the stellar component at longer wavelengths. Nather & Wild (1973) had observed a dark disappearance at the variability phase of 0.27 on 19 May 1972. Observations were taken through a clear filter with an 18 inch telescope at SAAO. They got a uniform disk diameter of 67$\pm$5 mas. This value is on the higher side and this may be due to the error in fitting where one has to rely on the predicted rate in the absence of any fringes. The large size may be due to TiO contamination also. Another occultation of R Leo was recorded by Di Giacomo et al. (1991) with the TIRGO infrared telescope through a CVF ($\lambda/\Delta\lambda = 62.5$) filter centered on the Brγ line of atomic hydrogen at 2.16 μm. The visual variability phase of R Leo during this observation was 0.18. The signal-to-noise ratio of the light trace was extremely good and the scintilation noise was of low frequency. They used the Model Independent Algorithm (Richichi, 1989) to obtain an angular size of 33$\pm$1.3 mas and it was a much better fit compared to the least squares fit which gave a value in the range 30-35mas. The brightness profile reconstructed by them from the deconvolution algorithm was largely symmetric.

Speckle interferometric observations were made at the 5m Palomar telescope (Blazit et al. 1977). A photon counting version of the speckle interferometer giving accurate digital results was used to resolve the disk of R Leo. The correlation profiles show a wide central peak which indicates a resolved disk. The diameter was derived by fitting the correlation profile to theoretical profiles obtained by convolving disk and Airy pattern autocorrelation of different sizes. The four filters used were centered at 0.54 μm, 0.716 μm, 0.730 μm and 0.74 μm with a bandwidth of 0.02 μm. The UD values obtained were 32$\pm$5 mas, 49$\pm$9 mas, 54$\pm$9 mas and 30$\pm$7 mas respectively. Labeyrie et al. (1977) have pointed out the abrupt variation in the angular size with wavelength seen in these narrow band observations. By theoretical modelling of the optical depth in the TiO features as a function of wavelength, these variations are interpreted as due to large opacity of TiO and that in strong TiO features the diameter is larger by a factor of 2. Mariotti et al. (1983) observed R Leo in the CO first overtone spectral region (λ=2.38 μm, $\Delta\lambda$=0.11 μm) on 12 May 1981. They arrived at an upper limit of 75 mas for this source. This is larger than the values of Labeyrie et al. (1977) which implies that the extension of the atmospheric region optically thick at the wavelength of the first overtone CO feature is not much larger than that where the TiO bands are optically thick. This is quite consistent with the fact that the first overtone CO bands are formed relatively deep in the stellar atmosphere. They conclude that narrow band observations are essential for investigating the wavelength dependent variations due to the CO absorption because the contamination coming from the continuum will be removed.

McCarthy & Low (1975) give an upper limit to the 5 μm observations with the Spatial Interferometer. They derive an upper limit of 280$\pm$50 mas. The 10 μm silicate excess is common to these late type variables. The silicate excess accounts for 35% of the 11 μm flux (Merrill & Stein 1976). A uniform circular shell of diameter 280$\pm$90 mas was obtained by fitting the data recorded by the Spatial Heterodyne Interferometer (Sutton et al. 1977). This implies that the silicate emission comes from material within 5 $R_\star$ as compared to 12 $R_\star$ for M supergiants like α Ori

and α Sco. This result for R Leo is consistent with that of Neugebauer et al. (1973).

There is a large dispersion in the published measurements that cannot be entirely attributed to the intrinsic expansion and contraction of R Leo itself. The widely accepted suggestion is that the scatter in the angular diameter measurements may be due a real wavelength-dependent variation in conjunction with the pulsational cycle. Many interferometric groups have been systematically monitoring the diameter of many LPVs including R Leo. Tuthill et al. (1994) and Haniff et al. (1995) have studied R Leo with the non-redundant mask (NRM) method at the Ground-based High Resolution Imaging Laboratory (GHRIL) of the William Herschel Telescope (WHT). They have pointed out that Gaussian profiles fit better to the data as compared to the uniform disk. Burns et al. (1998) present observations spanning two pulsation cycle of the star taken with the COAST and the WHT. Observations were centered around 940nm and 830nm. They have fitted both Gaussian profiles as well as UD profiles to the data and have re-emphasized the fact that Gaussian profiles fit better and the ratio between the UD diameter to the FWHM of the Gaussian fits remains constant. The variations in both the bands were around 15 mas. The most important feature of their analysis was the large phase-coherent modulation of the angular sizes. In both the colours the brightest phases of the star corresponded to the smallest angular size. Such variations in the angular sizes were seen in *o* Ceti (Tuthill et al. 1995). But the fluctuations in the diameter in this case had no relationship with the variability period. A selected sample of the interferometric and occultation results are shown in Table 3.3.

Apart from these direct angular size measurements a lot of work has been done to estimate this fundamental parameter by indirect methods. Infrared (1.2 – 4 μm) spectra of R Leo was obtained by KAO at the phase of 0.51 (Strecker et al. 1978). Uniform disk diameter of 41 mas was obtained for all the three bands of 1.4 μm, 1.9 μm and 2.7 μm. The fitting of a single temperature blackbody to the continuum points of the spectra resulted in these wavelength independent values.

Table 3.3: Selected examples of previous high angular resolution observations of R Leo.

Date	Phase	Technique	λ (μm)	UD(mas)	Ref.
1990 May 2	0.18	Lunar Occul.(TIRGO)	2.16	33.1 ± 1.3	(1)
1992 Jan. 20	0.21	Optical Interf.(WHT)	0.833	44.9 ± 2.0	(2)
1992 Jan. 20	0.21	Optical Interf.(WHT)	0.902	43.3 ± 2.0	(2)
1993 Jun. 10	0.84	Optical Interf.(WHT)	0.700	64.2 ± 5.7	(2)
1993 Jun. 10	0.84	Optical Interf.(WHT)	0.710	67.9 ± 7.0	(2)
1996 Feb. 26	0.04	Optical Interf.(COAST)	0.940	36.3 ± 1.3	(3)
1996 Feb. 26	0.04	Optical Interf.(COAST)	0.830	36.3 ± 1.3	(3)
1996 May 3	0.26	Optical Interf.(COAST)	0.940	40.3 ± 0.7	(3)
1997 Jan. 24	0.11	Optical Interf.(COAST)	0.940	38.0 ± 2.0	(3)
1997 Apr. 15	0.38	Optical Interf.(COAST)	0.940	43.5 ± 1.3	(3)
1997 Apr. 15	0.38	Optical Interf.(COAST)	0.830	45.2 ± 1.0	(3)
1997 Apr. 30	0.42	Optical Interf.(COAST)	0.940	41.2 ± 2.0	(3)
1997 Apr. 30	0.42	Optical Interf.(COAST)	0.830	45.4 ± 2.0	(3)
1997 May 12	0.46	Optical Interf.(COAST)	0.940	51.2 ± 3.0	(3)
1997 Jun. 22	0.60	Optical Interf.(WHT)	0.940	50.2 ± 2.8	(3)
1997 Jun. 22	0.60	Optical Interf.(WHT)	0.830	50.8 ± 1.6	(3)

References: (1) Di Giacomo et al. (1991); (2) Haniff et al. (1995); (3) Burns et al. (1998).

From the $1 - 5\,\mu$m flux curve obtained at KAO Scargle & Strecker (1979) have computed models for the atmospheres of Miras. Fitting the observed flux curve and interpolating with a nearby model curve gave values of 56.3 mas and 39.7 mas at phases 0.51 and 0.18 respectively. But the fitted reddening values were too high for the distance of R Leo. In the absence of this extinction term the values derived were 35.6 and 23.9 mas. Robertson & Feast (1981) have calculated the blackbody angular size of R Leo to be 37 mas. By comparing the lunar occultation observations of Ridgway et al. (1979) and the derived blackbody sizes of their sample

they have shown that the blackbody temperature and the effective temperature are the same and have justified the use of the blackbody temperature for deriving the angular diameter. Adopting a model for the circumstellar dust shells made up of 'dirty' silicate grains (Jones & Merrill 1976), with a grain size of 0.1 μm and the density distribution compatible with a constant mass flow at uniform velocity, Rowan-Robinson & Harris (1983) derive a 11μm shell size of 320 mas and 41 mas for a stellar disk at visual wavelengths.

3.2.3 *Data Analysis*

The analysis is generally along the lines of the standard non linear least squares method discussed in Chapter 2. The filter used at Gurushikhar is not a standard one, hence the optical bandwidth effects have been incorporated in the analysis assuming a Gaussian shape of the circular variable filter response with a FWHM value of 0.05 μm corresponding to the resolving power ($\lambda/\Delta\lambda$) of 70 at the wavelength of 3.36 μm. In the absence of fringes to define the component velocity, we have used the predicted value in the analysis. For this particular source we have tried out three different source brightness profiles, namely (a) a uniformly illuminated disk, (b) a fully limb darkened disk and (c) a source profile with a Gaussian radial variation of intensity. For the first two cases the source profiles are obtained from Eqn. 2.1 by putting $\kappa = 0$ and $\kappa = 1$ respectively for the uniform disk and the limb darkened model. In case of a Gaussian model assuming that the radial intensity variation is a Gaussian we obtain the one dimensional brightness profile in the form

$$S(\phi) = 2I_0 e^{-a\phi^2/\Omega^2} \int_0^{z=(\Omega^2-\phi^2)^{1/2}} e^{-az^2/\Omega^2} dz \tag{3.1}$$

where

$$a = 4\ ln\ 2 \Big/ (\frac{FWHM}{\Omega})^2 \tag{3.2}$$

The FWHM here refers to that of the Gaussian variation of intensity across the radial strip. It should be noted here that this FWHM is different from that of the resultant one-dimensional source brightness profile as is evident from Eqn. 3.1.

The integration in Eqn. 3.1 is done numerically.

3.2.4 *Results and Discussion*

Angular Diameter

Fig. 3.1 shows the occultation data and the best fit for event 1. The derived uniform disk angular diameter is 39±3 mas. The inset is the error curve which shows the relative χ^2 as a function of angular diameter. It can be seen that the χ^2 reaches a clear minimum at 39 mas. The light curve at 2.2 μm (event 2) along with the best fit uniformly illuminated disk model is shown in Fig. 3.2. The uniform disk angular diameter derived for this event is 34 ± 2 mas . The error curve (inset) again clearly shows the convergence of the χ^2 to a minimum at this value. The main source of error in both the data sets is the presence of large scintillation noise arising out of less than optimum observing conditions. This is evident from the residuals of the fit shown in the lower panel of the Figs. 3.1 and 3.2.

The previous 2 μm observations of Di Giacomo et al. (1991) gave a value of 33±1.3 mas using the model-independent algorithm given in Richichi (1989). However, the least squares method leads to diameters in the range 30 – 35 mas. Comparing either of these two values with the current measurement (event 2), we see that there is no appreciable change of the angular size with phase at 2.2 μm, unlike that seen in the optical region. In Table 3.4 we compare our occultation results with interferometric values obtained at nearly the same phase. To compare our derived values with the optical interferometric values at the same phase, we have to convert the UD values to the photospheric angular sizes. This refers to the diameter at which the Rosseland mean opacity equals unity. Measurements in the NIR are generally expected to be less affected by atomic and molecular absorption, and probe the underlying continuum emission. Furthermore, limb darkening effects decrease with increasing wavelength. Hence the angular diameter obtained at NIR wavelengths is expected to be close to the Rosseland photospheric diameter, and

Table 3.4: Comparison of NIR results of R Leo with interferometry results at nearly the same phase.

Date	Phase	Technique	Filter ($\lambda/\Delta\lambda$)	UD (mas)	Photospheric Diameter(mas)	Refs.
1997 Feb 7	0.16	Optical Interf.	0.94/0.05	39.8±4.0	37.4 ±4.0	1
1996 Mar 29	0.16	Optical Interf.	0.94/0.05	37.8±1.0	35.5±1	1
1997 Dec 19	0.17	Lunar Occul.	3.36/0.05	39.0±3.0	39.0±3	2
1997 Apr 23	0.40	Optical Interf.	0.94/0.05	48.2±2.5	45.8±2.5	1
1997 Apr 30	0.43	Optical Interf.	0.94/0.05	41.2±2.0	39.1±2.0	1
1997 May 12	0.46	Optical Interf.	0.94/0.05	51.2±3.4	48.6±3.4	1
1998 Mar 10	0.44	Lunar Occul.	2.2/0.46	34±2.0	36±2.0	2

References: (1) Burns et al. (1998); (2) Tej et al. (1999).

the corrections for the atmospheric extension and limb darkening are small. This is borne out in the 2 μm region by the infrared spectra of R Leo taken with the Kuiper Airborne Observatory (Strecker et al. 1978). The stellar continuum is well represented at 2.2 μm. However, at 3.36 μm the problem is more complicated as it lies in the long wavelength wing of the very strong absorption centered at 2.7 μm due to water vapour in the R Leo atmosphere. The Rosseland diameter is ill-defined at this wavelength and the angular diameter needs to be carefully interpreted. In the optical region the corrections for limb darkening and atmospheric extension are more severe especially for stars like R Leo with an extended atmosphere. In Table 3.4 we have listed the UD and the Rosseland (photospheric) diameter values as well as the optical interferometric observation of Burns et al. (1998) taken at nearly the same phase of the previous two cycles. The optical UD values are converted to the photospheric values using averaged conversion factors listed in Tuthill et al. (1994). A conversion factor of 1.05 (Hofmann et al. 1998) is used for our 2.2 μm measurement. In the absence of specific information, the conversion factor for the

3.36 μm region is taken to be unity. It can be seen that the photospheric diameter values determined by the occultation and interferometric methods are in good agreement for event 1. Comparing the true physical diameters we see that the optical values near the phase of event 2 (0.40 – 0.46) are distinctly larger than the K band angular size by more than 20%. This indicates that at 2 μm we are looking deeper into the atmospheric layers, closer to the true stellar continuum.

Comparing the 2 μm diameter values at the two phases (0.18 and 0.44), the 3.36 μm diameter at phase 0.17 and the optical values over two pulsational cycles, we infer that the periodic variation in the angular diameter with phase is more pronounced in the optical than in the NIR. The phase and cycle dependence of the photospheric structure and observable properties of Mira variables has been addressed in the recent time-resolved models of Bessell et al. (1996). They identify three different types of behaviour of the angular diameter variation of a LPV: a) small amplitude ($\sim$10%) modulations associated with continuum layers; b) large aperiodic fluctuations due to irregular behavioiur of the shock fronts in the uppermost region of the extended atmosphere; and c) very large variations ($\sim$50%) in bandpasses contaminated by TiO absorption features. In case of both continuum layers or moderately contaminated bands, these models relate the periodic variation of the angular diameters with the outward motion of the innermost shock front in the stellar atmosphere. Based on this, one expects a maximum apparent size at phase $\sim$0.2 and then a decrease through and beyond phase 0.5. The optical observations presented in Burns et al. (1998), however, contradict this prediction. In these optical measurements, we see the brightest phases corresponding to smallest angular size and a rapid increase in the size from visual variability phase 0.35 to 0.45. This can be perhaps explained with a combination of the movement of the inner shock and the strengthening of the TiO absorption feature during the photometric cycle. de Laverney et al. (1997) have also shown that for Mira variables the coolest spectral types are found at minimum phase. Strecker (1973) has also derived the angular size based on the colour temperature from the 3.5 μm and 1.04 μm colour indices. He shows that there is a steady increase in the size from

zero phase to a phase of 0.35 and then there is a gradual decrease. Our values of 39 mas at phase 0.17 and 36 mas at phase 0.44 of the same cycle imply a possible variation in angular diameter of 3$\pm$3.6 mas. This value appears to be consistent with Bessell's predictions of the continuum diameter variation. However, the errors involved in the measurements preclude a definitive conclusion. The problem is further complicated by water vapour absorption effects at 3.36μm, which prevent a true continuum measurement at this wavelength. The small apparent increase in the measured angular size from 2.2μm to 3.36μm could also be partially due to this water vapour absorption layer and cannot be attributed totally to the continuum variation. In any case we do not definitely see the large phase coherent angular diameter variations reported in the optical region. The blackbody distribution of the spectral energy also gives a possible explanation to the small variation seen in the infrared as this part of the spectrum is less sensitive to temperature changes. Further true continuum measurements at 2.2μm with a narrow bandwidth and with good precision (a few %) are needed to test the models of Bessell et al. (1996). In a recent work, Perrin et al. (1999) have discussed the interferometric observations of R Leo in the K band with the FLOUR beam combiner at the IOTA interferometer. They present observations at two different epochs in 1996 and 1997 at visual variability phases of 0.24 and 0.28 respectively. Uniform disk models fitted to the low spatial frequencies yield diameter values of 28.18$\pm$0.05 mas and 30.68$\pm$0.05 mas respectively for both the epochs. They conclude a variation in the angular diameter which they suggest is due to the apparent pulsation of the atmospheric layers very close to the stellar photosphere.

Prompted by the suggestions of Haniff et al. (1995) and Burns et al. (1998) we tried fitting a Gaussian source profile to our occultation data. We also tried out the fully limb darkened profile. The nature of the two profiles are discussed in the previous section. Fig. 3.3 gives the one-dimensional source intensity distribution function S(ϕ) for the three cases which provide best fit to the data in their respective domains. From the fits we could not discern any substantial difference beyond the noise level as seen clearly seen from the lower panel of Fig.3.1. The

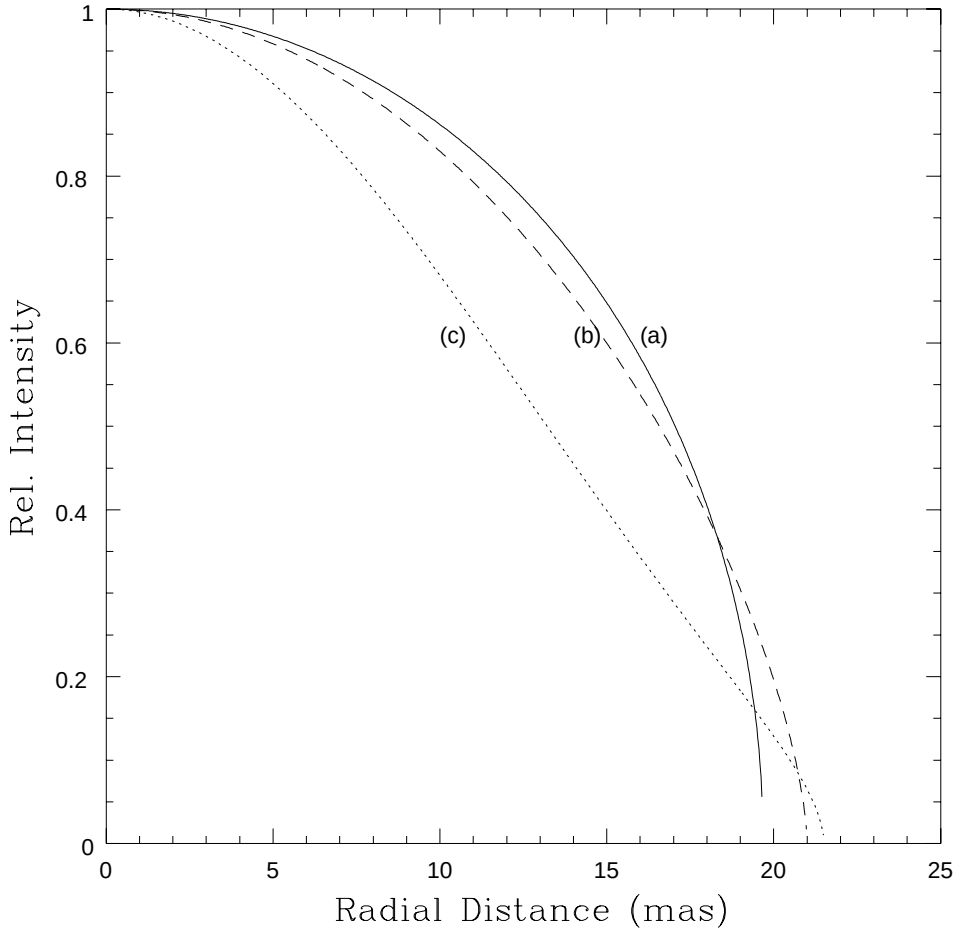

Figure 3.3: Source profiles for the three case. (a). The uniform disk (b). The fully limb darkened disk and (c). The Gaussian intensity profile.

best fit Gaussian has a FWHM of 26.4 mas and the fully limb darkened disk gives a value of 41 mas. However, we wish to point out that recent interferometric observations of R Leo using the Fine Guide Sensor of Hubble Space Telescope (Lattanzi et al. 1997) indicate clear departures from circular symmetry in the atmosphere of R Leo. The major axis is found to exceed the minor axis by 11%. Evidence also exists for asymmetric brightness distribution across the stellar disk. However, possible departures from circular symmetry at the photospheric level could be due to temperature excesses of a few hundred degrees on the stellar surface. Such excesses could result in a bright spot in the visible region, but may not be detectable in the NIR near the peak of the blackbody distribution corresponding to the star,

which makes circular symmetry a reasonable assumption in the infrared. However, recent measurements on o Ceti with the COME-ON$_+$ adaptive optics system (Cruzalèbes et al. 1998), show evidence of asymmetric distribution of circumstellar matter in the J,H and K images but it is not established that this asymmetry continues up to the photospheric level. Nonspherical structure due to inhomogeneities and clumps in the dust shell of o Ceti has also been seen in the 11 μm observations reported by Lopez et al. (1997). Hence, a circularly symmetric Gaussian profile may not be strictly true in case of R Leo. There is evidence for a possible asymmetric brightness profile also from our 2.2μm data, but this is not conclusive due to the limited signal-to-noise ratio.

Effective Temperature and Linear Radius

The effective temperature is calculated using the relation

$$T_{eff} = 1655.3(F_{bol}/\phi^2)^{1/4} \tag{3.3}$$

where F_{bol} is the apparent bolometric flux in units of 10^{-8} erg cm^{-2} s^{-1} and 2ϕ is the angular diameter in mas. Most of the energy of LPVs is emitted in the near infrared, hence the bolometric magnitude can be calculated with good accuracy by fitting a blackbody function to the measured $JHKL$ photometry. Adopting the apparent bolometric magnitude (m_b) value of 0.69 (corresponding to a bolometric flux of 1.314 $\times$ 10^{-5} erg cm^{-2} s^{-1}) derived by van Leeuwen et al. (1997) and our event 1 diameter value of 39$\pm$3 mas, we obtain the effective temperature as 2257$\pm$110 K . For event 2, using the measured JHK magnitudes and the IRAS flux values, the bolometric flux was calculated to be 1.34$\pm$0.22 $\times$ 10^{-5} erg cm^{-2} s^{-1}. The corresponding value of the effective temperature for the Rosseland diameter of 36 mas is 2363$\pm$120 K.

The distance estimates of R Leo have ranged from 102 pc (Rowan-Robinson & Harris 1983) to 304 pc (Knapp & Morris 1985). Danchi et al. (1994) in their analysis have adopted a value of 120$\pm$15 pc derived from the trigonometric parallax of

8.3±1.0 mas obtained by Gatewood (1992). This was the only trigonometric parallax measurement of any Mira prior to the Hipparcos observations. This parallax value matches well with the Hipparcos value of 9.87±2.07 mas. van Leeuwen et al. (1997) adopt a weighted value of the two parallax measurements of 8.81±1.0 mas. In our calculations we use this value, which corresponds to a distance of 114±14 pc. Taking this distance and our photospheric angular diameter values, we obtain a linear radius of 478±50 $R_\odot$ for event 1, and 441±50 $R_\odot$ for event 2. These values of the linear radii along with the derived effective temperatures are consistent with the radius versus effective temperature relation given in van Belle et al. (1996), after correcting for the linear radii of their sample with a uniform disk to Rosseland diameter conversion factor of 1.05.

Mode of pulsation

The mode of pulsation in Miras has been uncertain for a long time. The driving mechanism for the pulsations is probably due to the combined action of partial H and He I ionization. In the atmospheres of these variables, convection is the dominant mode of energy transport and the timescale of the convective overturn is of the same order as the pulsational cycle. Hence, to understand the mechanism of pulsation in Mira type variables it is important to first understand its coupling with the convection and the influence of convection on the equilibrium structure of the star. Both aspects are not well comprehended at present. This leaves the results of pulsational studies stubbornly inconclusive till date. Balmforth et al. (1990) showed that the inclusion of turbulent pressure in their models alters the equilibrium state. Hence, the excitation rates and the periods of radial pulsations are considerably influenced. Accounting for both the perturbed convective energy flux and the turbulent pressure to couple the pulsation and convection in the envelopes, they have obtained the first overtone as the dominantly destabilized pulsation mode. Fox & Wood (1982) had deduced similar results by including the time dependence of the convective flux in a kind of flux retardation model. They

suggest that only at luminosities leading to periods of about 320 days, the fundamental mode grows faster. Based on this they had concluded that that most Miras pulsate in the first overtone. However, Ostlie & Cox (1986) concluded from their linear pulsation calculations that Mira-type variability is consistent with the fundamental mode. Similar scenario was also suggested by Wood (1990). Suppressing the growth of the fundamental mode and forcing the first overtone mode in his Mira models resulted in velocity fields which were incompatible with the observations. Tuchman (1991) rejected the possibility of the fundamental mode based on his acceleration analysis to the observed CO molecular lines in Mira variables. But in a recent paper Yaári & Tuchman (1999), have concluded that the radii observations of Mira variables are compatible with the theoretical nonlinear models pulsating in the fundamental mode. Bessell et al. (1996) have also shown that their nonlinear pulsation models, using the first overtone mode, do not accurately produce typical Mira variable properties.Some earlier studies based on photometry and the empirical Period-Luminosity relation indicate first overtone mode (Wood 1975, Robertson & Feast 1981); however, the dynamical behavior of these LPVs are well explained from CO velocities assuming the fundamental mode (Wilson 1983).

Spatial high resolution interferometric observations of Mira variables alongwith the accurate parallax measurements have gone a long way in constraining this debate. Based on linear pulsation models Tuthill et al. (1994) and Haniff et al. (1995) have presented evidence for Mira type variables to be either first overtone or higher overtone pulsators. Perrin et al. (1999) present recent K band measurements of R Leo taken with the FLOUR beam combiner of the IOTA. Taking the low (< 40 cycles/arcsec) spatial frequencies, and after correcting for limb darkening, they derive linear radii values of 315 ± 84 $R_\odot$ and 343 ± 91 $R_\odot$ respectively for the two epochs of their observations. These values are appreciably low compared to previous determinations and fall in the overlapping zone of first overtone and fundamental mode in the period-linear radii plot. Scattering by molecular species has been suggested to partly explain the high frequency excess. Taking this excess into account further decreases the radii value (22-24 mas) and makes it clearly a

fundamental pulsator. But general models of Mira photospheres fail to reproduce the high frequency visibilities seen in the FLOUR data. However, we wish to point out that there is a need for more visibility points in order to get an accurate fit and obtain an accurate diameter value. In their analysis of the angular sizes of 18 Miras variables at 2.2 μm, van Belle et al. (1996) find that these variables can oscillate in both the fundamental as well as the first overtone mode depending on the mass and the radius of the individual star. They have used the Period-Mass-Radius relation of Ostlie & Cox (1986) to estimate the pulsational mode of Miras. For the fundamental mode and first-overtone pulsators, respectively:

$$log\ P = 1.86\ log\ R - 0.73\ log\ M - 1.92 \tag{3.4}$$

$$log\ P = 1.59\ log\ R - 0.51\ log\ M - 1.60 \tag{3.5}$$

where M and R are in solar units and P in days. Van Belle et al. (1996) derive a plot of radius versus period for different mass ranges. This requires an acceptable mass range, which is quite uncertain for Mira variables. Haniff et al. (1995) prefer the range 1.0 $M_\odot$ < M < 1.5 $M_\odot$ taking into account the high mass loss associated with this class of variables. Van Belle et al. (1996), however, have taken the mass range of 0.8 $M_\odot$ < M < 3.0 $M_\odot$ as suggested by Wilson (1983) and Wood (1982). In a modified version of Fig. 5 of van Belle et al. (1996), we have plotted in Fig. 3.4 the position of R Leo for both the events and few other representative stars from van Belle et al. (1996) and Haniff et al. (1995). The Ostlie & Cox relationship for the mass range 0.8 $M_\odot$ < M < 3.0 $M_\odot$ is also shown for both the fundamental and the first overtone regions. Our derived values of linear radii of R Leo, for both the events and with a period of 309.95 days, precludes the fundamental mode and puts it in the first overtone region. This is consistent with the findings of Tuthill et al. (1994). We conclude from our observations that the first overtone mode is the prefered mode of oscillation in R Leo. As is clear from all the above discussions, continuous monitoring of Mira systems over the entire pulsation cycle with high accuracy measurements is required to explain the actual scenario.

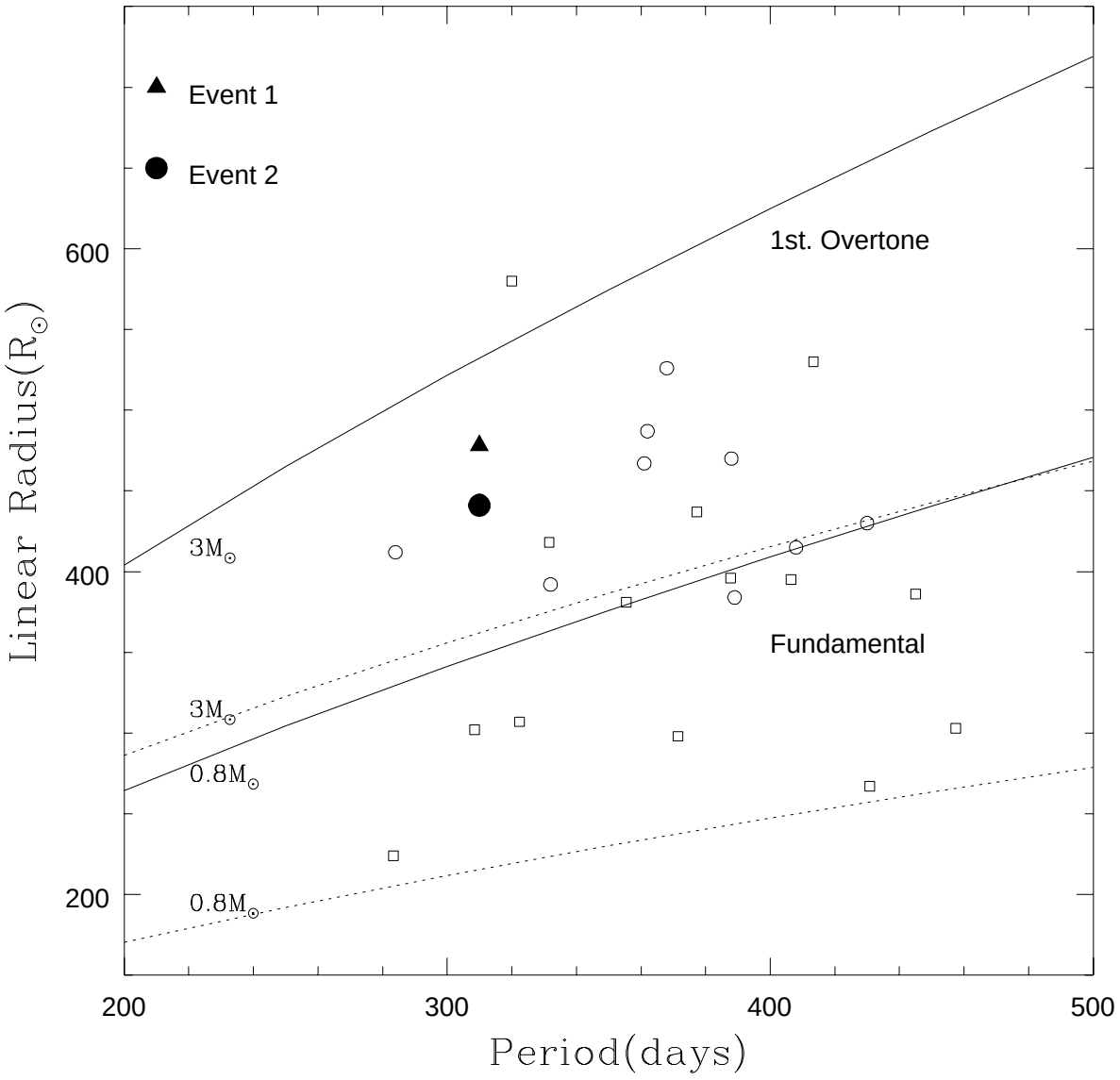

Figure 3.4: A plot of the linear radius versus the period for Mira variables. The closed triangle and circle represent our data. The lines indicate the Ostlie-Cox relation discussed in the text for the mass range 0.8 $M_{\odot}$ < M < 3.0$M_{\odot}$ for both fundamental (dotted line) and first overtone (solid line) modes. Overplotted are the 2.2 μm Mira data from van Belle et al.(1996) (open squares) and visible Mira data from Haniff et al.(1995) (open circles).

The distribution of dust surrounding R Leo has been studied at high spatial resolution using the Berkeley Infrared Spatial Interferometer at 11.5μm by Sutton et al. (1977), McCarthy & Low (1977) and Danchi et al. (1994). Danchi et al. (1994) list R Leo and o Ceti as the clearest cases for dust formation within the extended atmospheres of these stars. The mean distance of the inner radius of dust from the photosphere is $< 1.7R_\star$ where $R_\star$ corresponds to one stellar radius. This is consistent with the theoretical expectation (Draine 1981) that the dust may condense as close as $0.3R_\star$ from the photosphere of the star, which has an effective black body temperature of 2500 K and a hydrogen density of 10^{14}cm^{-3} at the photospheric radius. Further, dust is found to be closest to the star during times of lowest luminosity suggesting that the initial condensation occurs during the low luminosity phase. Danchi et al. (1994) find, with their best fit radiative transfer model for minimum phase of R Leo, an inner radius for the dust of 70 mas, an outer radius at 2500 mas with a stellar radius of 26.3 mas and a rather low stellar temperature of 1500 K. The dust is assumed to be a mixture of graphites and silicates to fit the IRAS spectrum which exhibits only a weak silicate signature.

In Fig. 3.5 we have plotted the spectral energy distribution (SED) of R Leo. The observational points are taken from literature and so we have only an average picture without taking into account the pulsational cycle of R Leo. As can be seen from Table 3.1 and the SED, the photometric variability of R Leo is small in the infrared compared to the optical region. This is explained from the nature of its black body distribution. The infrared part of the curve is less sensitive to temperature changes. For typical minima and maxima temperatures of 1700 K and 2700 K, the V band flux changes by a factor of $\sim$580 whereas the L band flux variation is only by a factor of $\sim$3.5. This accounts for the small photometric variability seen in the infrared. We have superimposed, using our results for event 1, a blackbody spectrum at the deduced effective temperature of 2257 K and a linear radius of 478 $R_\odot$

at a distance of 114 pc. It can be seen that there is an IR excess due to the circumstellar shell. Since our observations are at a wavelength of 3.36 μm, we estimated the expected shell contribution at this wavelength in order to establish whether the circumstellar dust could be detected in our occultation light curve. A shell spectrum has been fitted to the data with a radius of 50 mas using an optical depth of 0.1 at 11 μm from the observations of Danchi et al. (1994). The optical depth at other wavelengths have been calculated using the Q_{abs} values from Draine (1985). We have assumed the dust to be made up of astronomical silicate with a grain radius of 0.1 μm. It can be seen that the IR excess longward of 10 μm is adequately represented by the shell. The star-to-shell flux ratio at 3.36 μm is calculated to be $\sim$ 200 and is estimated to be uncertain by a factor of two. We have attempted to fit our 3.36 μm light curve with a star + shell model by taking the upper limit ($\sim$ 100) of the flux ratio estimate and a shell diameter of 140 mas. The residuals of this fit are comparable to the single star model. No significant change in the residuals of the two models is seen by increasing the shell contribution up to a star-to-shell ratio of $\sim$ 40. Considering the expected shell contribution, we infer that at 3.36 μm the detection of a shell component is beyond the limit of our instrument. Hence, the measured uniform disk angular diameter at 3.36 μm of 39$\pm$3 mas can be taken to represent the true stellar diameter without any circumstellar contribution.

3.2.5 Summary

1. We have carried out lunar occultation observations of R Leo at 3.36 μm (phase 0.17) and 2.2 μm (phase 0.44) which yield uniform disk diameters respectively 39$\pm$3 mas and 34$\pm$2 mas. The effective temperatures derived are 2257$\pm$110 K for event 1 and 2363$\pm$120 K for event 2.

2. Using an accurate distance value of 114$\pm$14 pc from recent parallax measurements, the linear radii of R Leo are derived to be 478$\pm$50 $R_\odot$ for event 1 and 441$\pm$50 $R_\odot$ for event 2 . These values constrain the pulsation mode in R Leo to be first overtone or higher and not the fundamental mode.

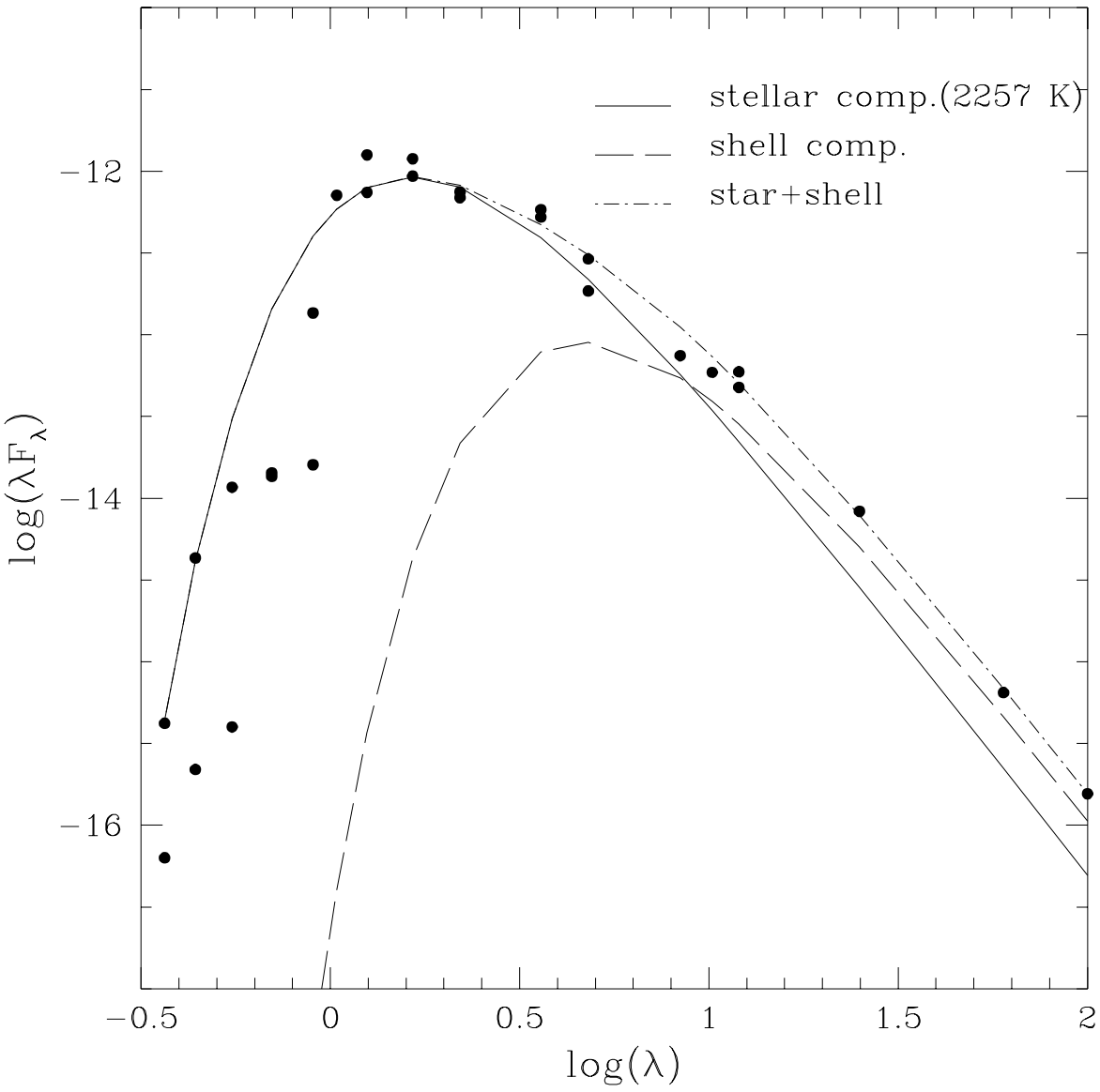

Figure 3.5: The spectral energy distribution of R Leo. The relative contribution of the star and the circumstellar shell along with photometric values over the optical/IR wavelength region are shown. The stellar component superimposed refers to the values of temperature and angular size derived from event 1, and corresponds to the phase near maximum temperature. The large photometric variation in the visible region is clearly seen.

3. The angular diameter at 3.36 μm is in good agreement with the optical interferometric determinations at nearly the same phase (0.17) which is close to the temperature maximum. The photospheric diameter derived at 2.2 μm is significantly smaller than the optical determinations at nearly the same phase(0.44). Along with the 3.36 μm measurement this result implies that the NIR angular diameter variation of R Leo with phase is small ($< 5\%$) unlike in the optical region. Detailed interferometric monitoring of R Leo at 2 μm in a narrow bandwidth free from absorption effects can give further insight into the pulsational scenario. Further, it would be interesting to measure the diameter at 2.38 μm with a narrow bandwidth to determine the extent of the CO atmosphere. Presently, we have only an upper limit of 75 mas (Mariotti et al. 1983).

3.3 Bright infrared source IRC-20563

Two 2.2μm lunar occultation observations of the bright IR source IRC-20563 separated by 219 days are discussed here. The possiblity of an intrinsic variation in the angular size has been investigated.

3.3.1 Observation

The two lunar occultation events of IRC-20563 were successfully observed with good S/N ratio with the 1.2m telescope at Gurushikhar, Mt. Abu. Table 3.5. gives the details of the two events. Both the events were observed in the K band with the instrument described in Chapter 2. Data sampling was done at 2ms for 120s centered around the predicted event time for both the events. Subsequent to the occultation, JHK photometry and CVF spectrophotometry were obtained for this source.

Table 3.5: Event details of IRC-20563.

Details	Event 1	Event 2
Date	1996 Apr. 10	1996 Nov. 15
Time (UT)	$22^h21^m34^s$	$14^h54^m30^s$
Altitude (star)	29.8^o	18.5^o
Position angle	259.28^o	76.55^o
Contact angle	173.95^o	1.96^o
Pred. Vel. Comp. (km/s)	0.7462	0.8715
Lunar Phase (days after new moon)	22.43	4.44
Event type	Reappearance	Disappearance
Focal plane aperture (arcsec)	65	26

3.3.2 *A Brief Source History*

IRC-20563(IRAS 19247-1722, AFGL 2391) has been classified as a M8.3 giant with a visual magnitude of 11.1 (Lockwood 1985). The other spectral classification is M8 (Hansen & Blanco 1975). Ridgway et al. (1979) have raised the question of this source being a suitable candidate for a Mira type because a clear variation of 0.14 mag in the J band is seen from their NIR photometry. No other variability study exists on this source. However, IRC-20563 falls in the class IIIa of the van der Veen and Habing (1988) classification based on the IRAS two color diagram. The objects in this class show a small increase of the [25]-[60] color as a function of the [12]-[25] color which signifies a large mass loss rate. Along this track there is also an increase in the variability which agrees well with the increase in mass loss.

From the earlier occultation observations of this source by Ridgway et al. (1979) the possibility of an intrinsic variation in the angular diameter of the source

cannot be ruled out. The earlier observations by Ridgway et al. (1979) in the K band are shown in Table 3.6. It should be noted that the noise is quite high in all

Table 3.6: Journal of earlier observations of IRC-20563.

Date	Angular Diameter (mas)
1976 Sept. 04	7.07±0.31
1977 Jun. 04	7.75±0.94
1978 Apr. 28	5.47±0.24

the three light curves. But taking the two best ones of Sept. 1976 and Apr. 1978, it can be seen that the difference in the diameter values are more than the formal error in the estimates.

IRC-20563 has the IRAS LRS class 23 which comprises of sources with oxygen rich circumstellar envelopes. The IRAS LRS of this source shows a broad emission at 9.8 μm indicative of the silicate feature (Olnon et al. 1986) common to stars of this class. Volk & Kwok (1987) have established the circumstellar origin of this feature. The colour temperature derived by them from the four IRAS fluxes is 480 K. IRC-20563 has been detected in CO emission. The line profile is parabolic and has a single peak indicating an optically thick CO emission which is not resolved by the telescope (Nyman et al. 1992). Taking the IRAS fluxes and assuming a bolometric luminosity of $10^4 L_{\odot}$, the distance estimate to this source is 0.86 kpc. There is no detection of SiO or OH masers in this source. No Hipparcos parallax measurement is available on this source.

3.3.3 Data Analysis

An extensive data analysis with both the methods described in Chapter 2 has been carried out on this source to investigate the possibility of detecting a variation in

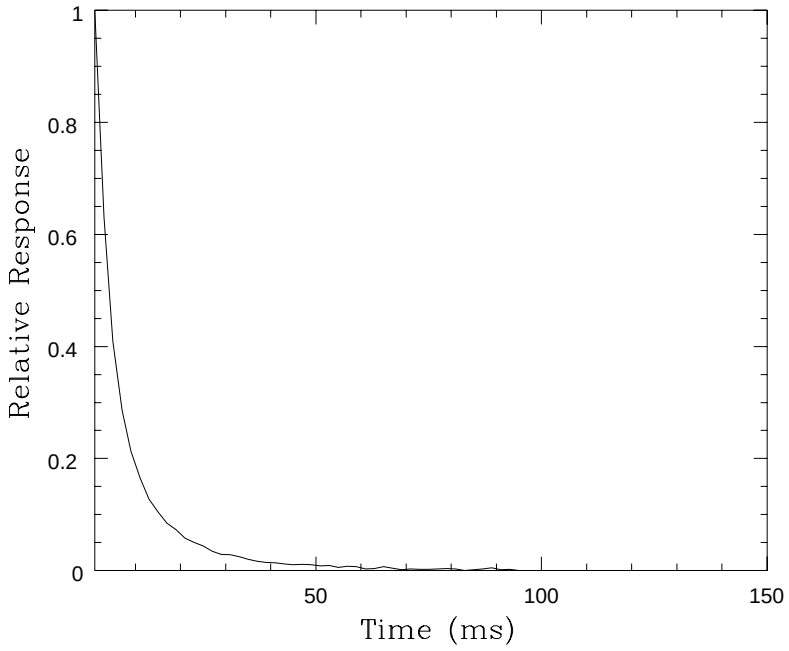

Figure 3.6: The corrected time response of IRC-20563

the angular size. In this section we discuss in detail the alternate approach of data analysis.

The signal level for the second event was almost 2.5 times higher than that of the first event. Cleaning of the primary mirror, better alignment of the instrument, different position of the bias and better sky condition must have contributed to the increase of the flux level. Because of this large signal, the data of the second event was corrected for the effect of signal variability of the detector which is discussed in Chapter 2. The time response curve which is recorded with the same signal level was also corrected. The original data and the corrected one are shown in Fig. 2.20 of Chapter 2. The corrected time response is shown in Fig. 3.6. This is the curve $\tau(t)$. In order to achieve high resolution the curve $P(t)$ (introduced in Chapter 2) and the time response curve $\tau(t)$ were interpolated to 0.1ms. The time response being a typical response curve which is one sided and falls to zero only in one direction, the convolution of $P(t)$ and $\tau(t)$ was performed based on the simple definition of convolution given in the following equation

$$P(t) * \tau(t) = \int_{-\infty}^{+\infty} P(z)\tau(t-z)dz \tag{3.6}$$

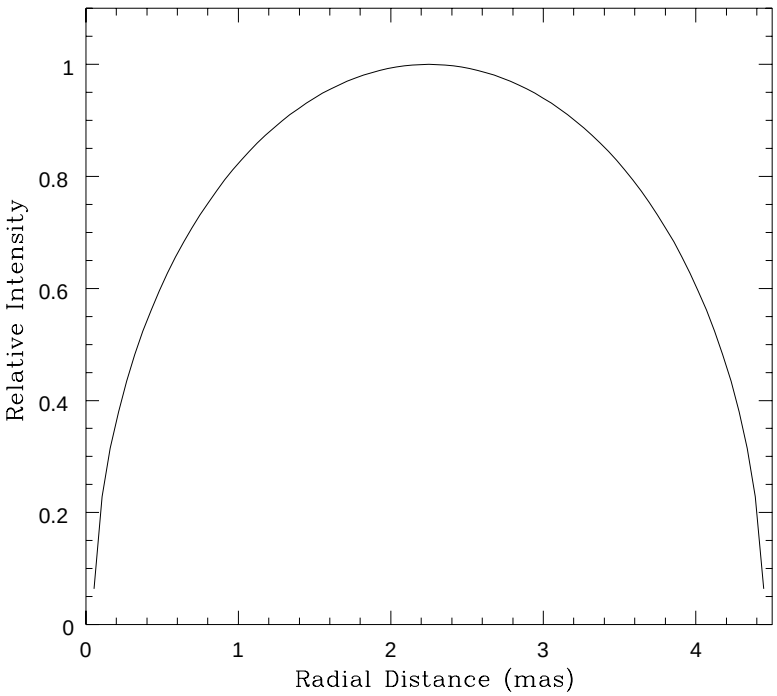

Figure 3.7: The generated source profile for 4.4 mas.

The integration was replaced by summation and was carried out numerically. It essentially means that the curve $P(t)$ is convolved with the time response by a shift and smear. The convolved output is given by

$$Q(t) = P(t) * \tau(t) \tag{3.7}$$

The source profile $S(\phi)$ was generated using Eqn. 2.1 for a uniformly illuminated disk. It was translated to the time frame of IRC-20563 by taking the predicted distance to the moon and the fitted velocity component obtained from nonlinear least squares method. Fig. 3.7 shows a generated source profile. It is a peaked function that goes to zero on both sides of the maximum. The convolution of $Q(t)$ and $S(\phi)$ was done by using the standard subroutine CONVLV of Numerical Recipes (Press et al. 1992). The subroutine demands the response function to be stored in the wrap-around manner. Zero padding of the data and the response function was done to avoid pollution of the output channels.

$$Q(t) * S(\phi) = I(t) \tag{3.8}$$

The output $I(t)$ is truncated manually to remove edge effects arising due to the

convolution. The angular size $S(\phi)$ is varied in discrete steps and the amplitude matching of the fringes to the data of IRC-20563 is done. To account for the velocity component of the event we start with a first approximation of the ratio of the fitted velocities (as obtained from the nonlinear least squares technique) of IRC+10032 and IRC-20563. Finer scaling of the x-axis is done to give the best fit.

3.3.4 Results and Discussion

Angular Diameter

We derive uniform disk values of 4.4±0.4 mas and 4.4±0.3 mas for the two events. Both the methods gave consistent values. The point to be noted is that not only did we obtain a consistent value of angular diameter from the two methods discussed but also the fitted velocity component values were consistent with each other. Fig. 3.8 and Fig. 3.9 show the data and the best fit uniform disk models to them. As is clearly noted, we do not see any variation in the angular size. We have also tried fitting the Gaussian source profile to the data. In this case also we could not discern between the fits. The uniform disk seemed to fit marginally better than the Gausian disk. The earlier observations listed in Table 3.6 are appreciably larger than the value we obtain. In the absence of any variability study and period measurement of this source, it is difficult to specify the phase of the two observations and hence any comment on the phase dependent variation of the size will not be justified. However, we wish to point out that the results of Rigdway et al. (1979) may not be accurate as the fits to the data were not good. Whereas, the fits shown in Fig. 3.8 and 3.9 are of high quality. The fact that we do not detect any variation in a span of 217 days is consistent with our results on R Leo, where the angular size variation is very small in the near infrared (Tej et al. 1999). Perrin et al. (1999) have also pointed out that pulsations of the central core induce large variations of brightness of Miras in the visible and smaller modulations of infrared magnitudes.

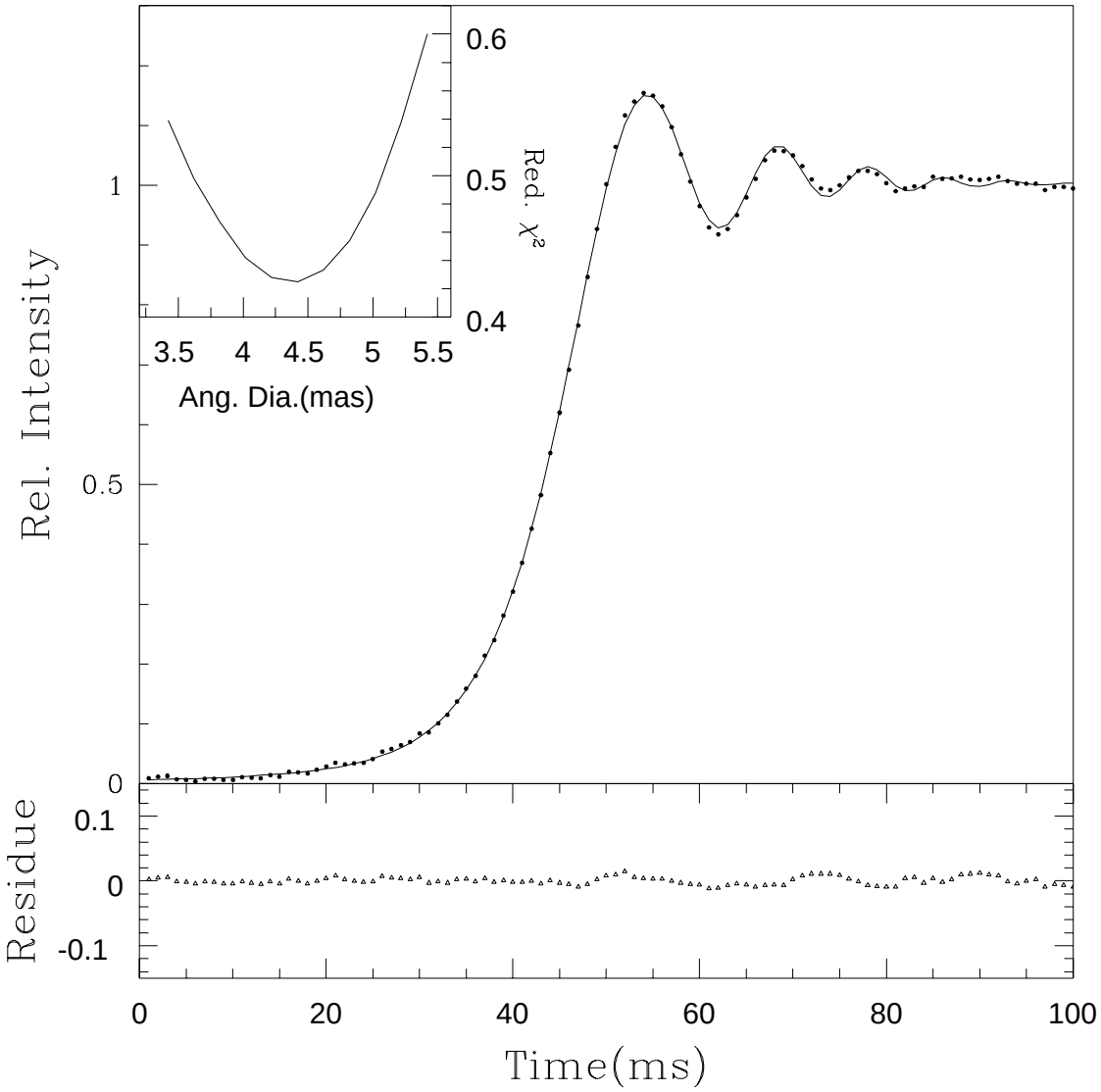

Figure 3.8: The occultation light curve for the reappearance event of IRC-20563. The data (dots) and the model fit to it (solid line) are shown alongwith the error curve (inset).

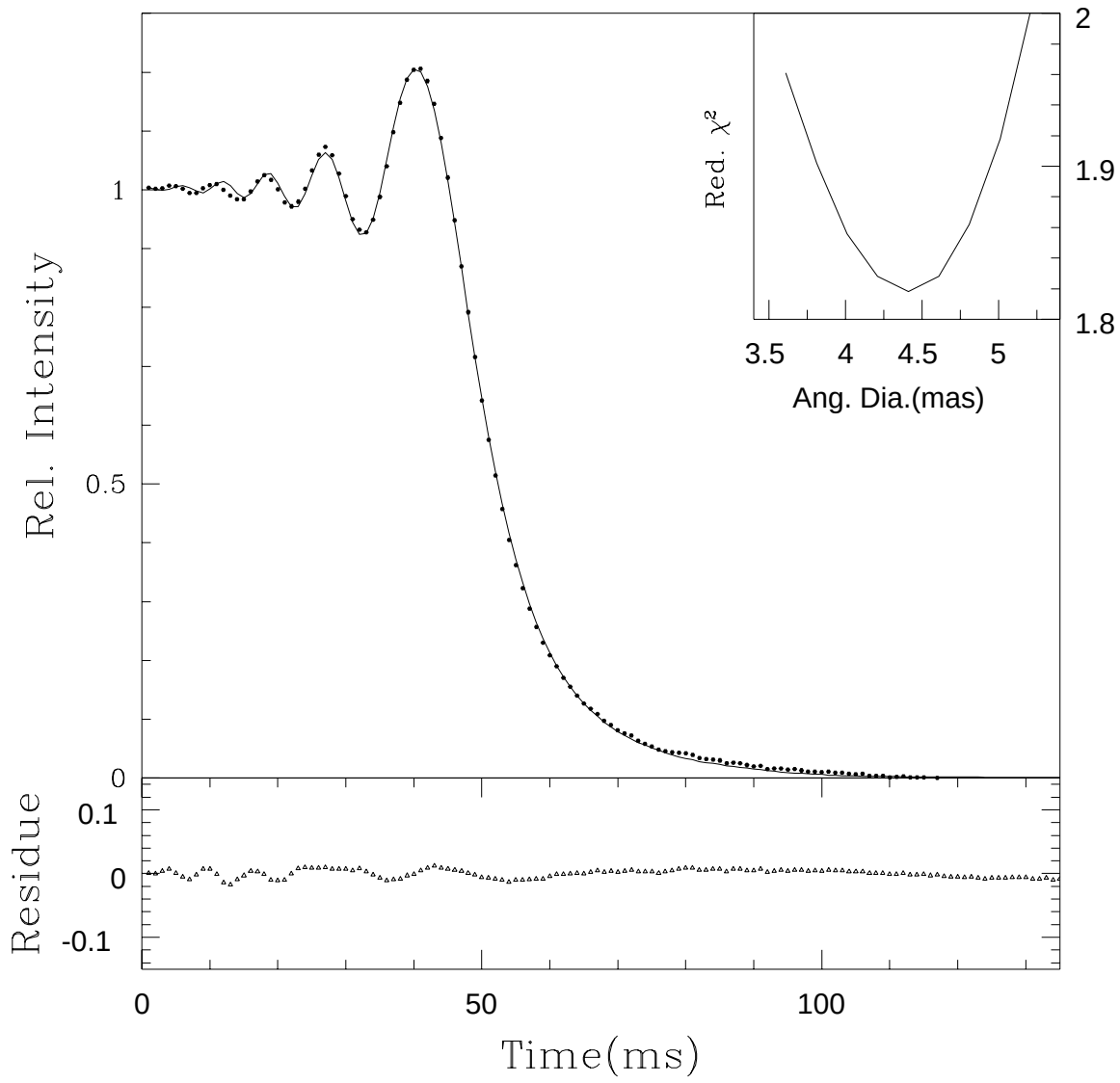

Figure 3.9: The occultation light curve for the disappearance event of IRC-20563. The data (dots) and the model fit to it (solid line) are shown alongwith the error curve (inset).

Table 3.7: JHK magnitudes and colours (IRC-20563)

Epoch (JD)	J	H	K	$J-H$	$J-K$	$H-K$
2450554.5	2.38±0.02	1.29±0.02	-	1.09	-	-
2450584.5	2.31±0.02	1.28±0.03	0.77±0.03	1.03	1.54	0.51
2450590.5	2.29±0.02	1.27±0.02	0.78±0.03	1.02	1.51	0.49

Possibilty of IRC-20563 being a Mira Variable

The suggestion by Ridgway et al. (1979) about IRC-20563 being a possible Mira prompted us to look into this aspect. We have carried out JHK photometry of this source on several occasions. The best three observations are listed in Table 3.7. As has been earlier pointed out by Ridgway et al. (1979), we too see a variation $\sim$0.1 magnitude in J which is the typical variation seen in Miras. Taking our JHK magintudes and other photometric data from literature we derive a bolometric flux of 6.032±0.6 $\times$ 10^{-7} erg cm^{-2} s^{-1}, which gives an effective temperature of 3110±131 K for this source. The infrared colours derived from our photometry and the effective temperature puts this source in the Mira zone in the two colour diagram of Feast et al. (1982) and the $\log T_{eff}$ versus the $(J-K)$ plot of Feast (1996). According to the colours in Perrin et al. (1998), IRC-20563 has a spectral type later than M8 in the epoch of our JHK photometric observations.

3.3.5 *CVF spectrophotometry*

CVF spectrophotometry of the source was also taken during the epoch JD 2450592.5. Standard procedure for the reduction of CVF data was adopted. Several scans of the source were taken and coadded. Removal of atmospheric absorption features and correction for variations in the instrumental sensitivity were accomplished by taking the ratio with respect to a star of early spectral type. This is because the

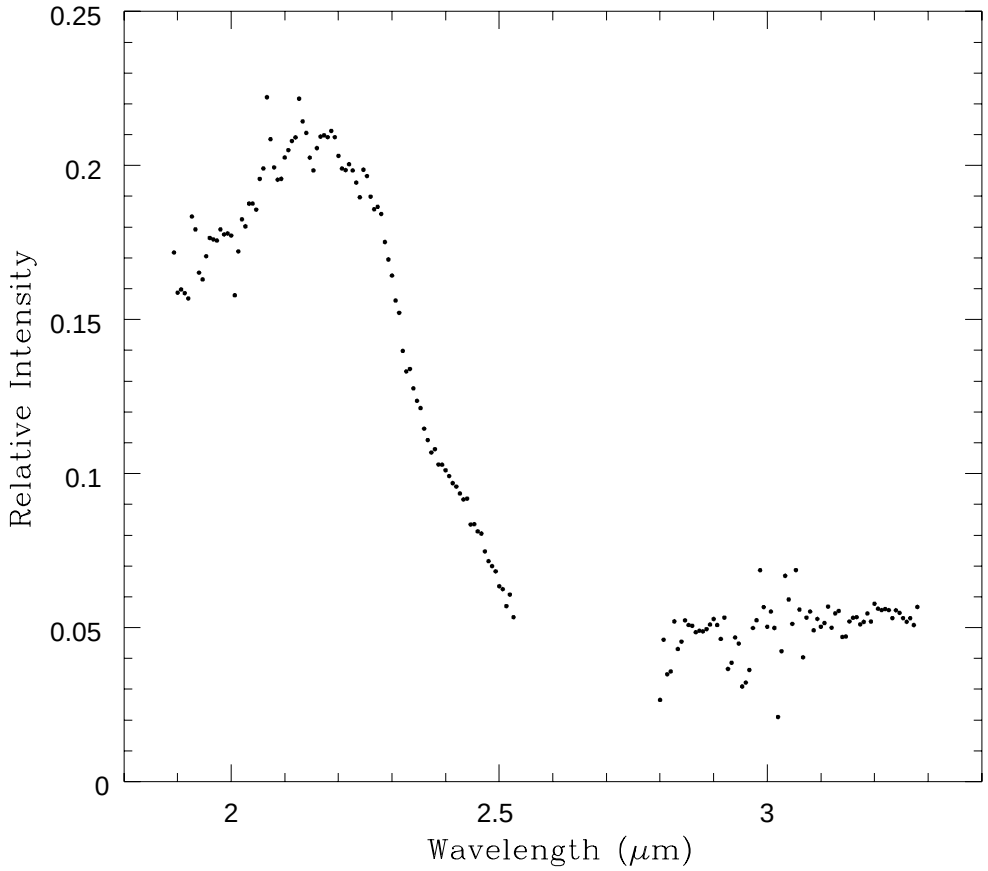

Figure 3.10: The CVF spectrum of IRC-20563.

spectra of early type stars are more or less featureless. At each wavelength the stellar flux was computed from the equation

$$F_{star} = F_{comp} \ \ (S_{star} - S_{sky})/(S_{comp} - S_{sky}) \tag{3.9}$$

where, S_{star}, S_{comp}, and S_{sky} are the signals from the program star, the comparison star and a nearby blank portion of the sky respectively and F_{comp} is the intrinsic flux of the comparison star which is taken to be a black body at the effective temperature of the star. We have taken α Lyrae as the comparison star. Fig. 3.10 shows the CVF spectrum of IRC-20563.

The 2.35μm CO absorption is very common to late M type giants and supergiants. The strength of the CO index is a signature of the spectral class of the

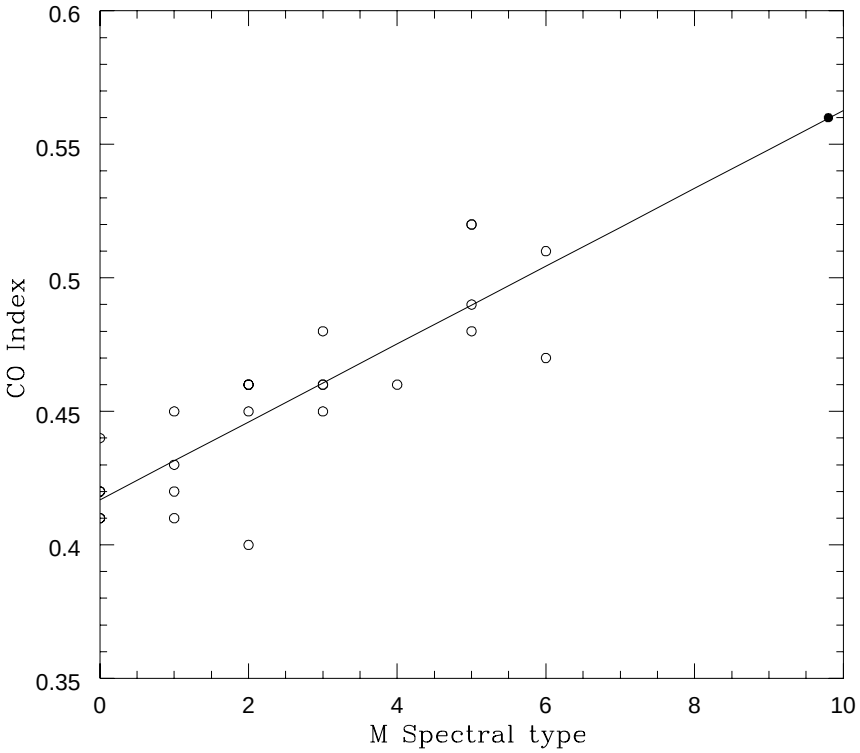

Figure 3.11: The plot of the M spectral type versus the CO index. The open circles are data points from Kenyon & Gallagher (1983). The closed circle is for the derived spectral type of IRC-20563. The line represents the linear regression fit to the data points of Kenyon & Gallagher (1983).

star. The CO index is given by the expression

$$CO\ index = [2.35] - [2.2] \tag{3.10}$$

where, the quantities in the [] are the respective monochromatic magnitudes. For IRC-20536 we get a value of 0.56 for the CO index. We have taken the CO index of a sample of 24 M giants from Kenyon & Gallagher (1983) and plotted the M spectral type versus the CO index. Fig. 3.11 shows the CO index and the M spectral type for the this sample. The linear regression fit to their data is given by

$$CO\ Index = 0.01457(M\ spectral\ type) + 0.4169 \tag{3.11}$$

From Eqn. 3.11 we derive a spectral type of M9.8 for IRC-20563. This is consistent with the spectral type derived for this epoch from the infrared colours.

3.4 Remarks

In this chapter we have presented results on Mira variable R Leonis and the suspected mira variable IRC-20563. We have discussed the variation in the angular diameter with phase for R leo and have derived the mode of pulsation of this star based on our angular diameter measurements. For IRC-20563 we have investigated the possible variation and arrive at a conclusion that from our data we do not see any variation in the angular size of this source. We have also speculated on it being a Mira variable from our infrared photometry and have derived the spectral type of IRC-20563 from CO absorption feature from the CVF spectrophotometry. The next chapter deals with the results on M giants.

Chapter 4

M Giants

4.1 Introduction

As hydrogen burning in the core of a 1 $M_\odot$ star ceases, the core contracts due to gravity and the temperature begins to rise until hydrostatic equilibrium is restored when helium ignites. The hot core causes the outer layers to expand and in this expansion the layers become relatively cold. And the star enters the red giant phase. These stars occupy the cool end of the HR diagram. Fig. 4.1 shows the post main sequence evolution of giants in the HR diagram. The red giant branch is marked RGB in the diagram. The M giant region {log T, M_{bol}} $\sim$ {3.4,-7} – {3.6,0} of the HR diagram hasn't been well explored as the evolutionary scenario still fails to produce very red objects and the bolometric corrections of these objects are needed to plot this part of the diagram. These are high luminosity ($\sim 100 - 1000\, L_\odot$) stars spread over the spectral types G – M. M giant stars represent the major part of these red giant stars. They are intrinsically interesting and can provide important information on stellar and galaxy evolution. When a star reaches the bottom of the red giant branch, a convective "dredge up" transports hydrogen rich material from the outer envelope to the deeper layers and processed material to the surface. Stellar winds which are important in this phase transport the material to the interstellar medium. Studies of M giants are therefore important for understanding the chemical evolution of our galaxy. From the apparent distribution of stars of various spectral types it is seen that the number of M stars is less compared to that of other spectral types. M giants constitute 4% of the total number of giants and

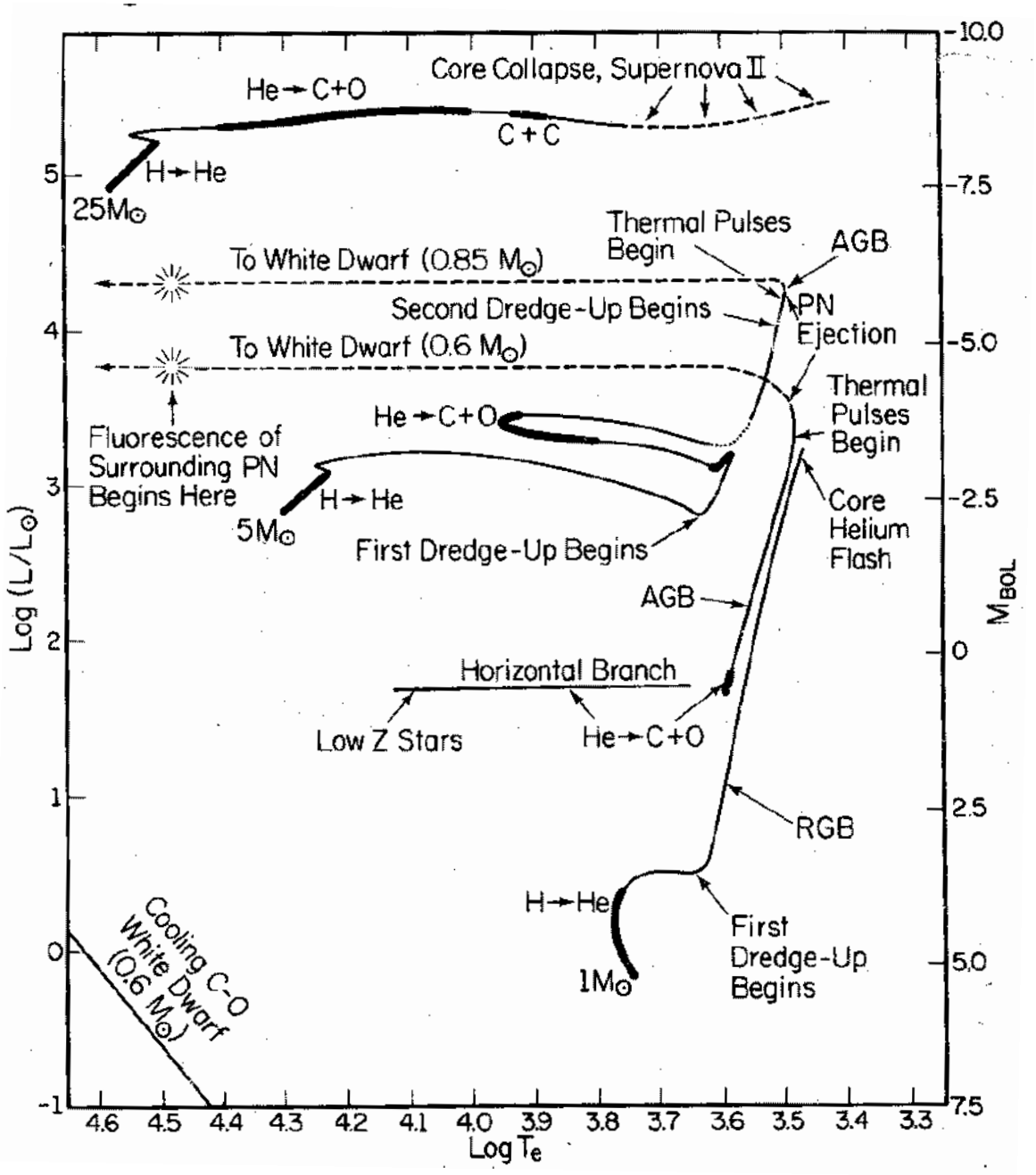

Figure 4.1: The Post-main sequence evolution of giants in the HR diagram (Iben 1985a & b).

supergiants in the solar neighbourhood. Among the M type stars present in the low galactic latitudes 93% are giants. M giants are relatively faint in the visible. Hence, compared to the early type giants they have not been the subject of intense scrutiny during the classical era of optical stellar astronomy. The most challenging problem is the detailed study of the surface structure of these stars. Extensive photometric and spectroscopic studies of this group of stars have been done in recent years (Fluks et al. 1994; Thé et al. 1990), but there is still a dearth of HAR observations. HAR studies in the NIR coupled with conventional photometry has gone a long way in determining the angular diameter and the effective temperature of this group of stars. With the advancement of lunar occultation technique and long-baseline interferometric methods in the NIR, a more focussed study of this class of stars is becoming possible. Absolute radii of stars are fundamental quantities which are very difficult to determine owing to the lack of accurate diameter measurements and proper distance determinations. Until recently, there has been only limited stellar radii values available in the literature for normal M type giants. A standard reference work like the "Astrophysical Data" of Lang (1992) has its last entry at spectral type M0III. The situation has greatly improved with the availability of the Hipparcos parallaxes. A recent work by Dumm & Schild (1998) gives the radii for 350 M giants. Their calculation is indirect, based on the empirical relation between the visual surface brightness and the Cousins (V-I) colour index. van Belle et al. (1999) give a more direct determination of linear radii of a sample of M giants from the angular diameter measurements by interferometric methods at 2.2 μm. With more reliable angular diameter measurements being made, a consistent calibration of the temperature scale can be attempted for this class of objects.

The effective temperature of stars characterizes the radiometric properties of the stellar atmosphere. It is the measure of total energy, integrated over the entire spectrum, radiated from a surface of unit area. In the model computations of stellar atmospheres, the effective temperature is a fundamental parameter and as one of the coordinates of the HR diagram, it plays an important role in the discussions of stellar evolution. Its accurate determination provides a decisive test

for the relevance of various stellar models (Blackwell & Lynas-Gray 1994). Even-though, its value is fixed by the radius and luminosity of the star, its computation from models is not straight forward as it is important to satisfy the physical criteria and the boundary values. Böhm-Vitense (1981) reviews various indirect methods of estimation of T_{eff} based on photometric and spectroscopic data. T_{eff} being a global property of the star, cannot in general be determined either from photometric colours or from atomic and molecular excitation. These give temperatures which are only indirectly related to the T_{eff}. Moreover, the spectra of M type giants are severely affected by molecular absorption. Due to strong molecular band opacities the spectral energy distribution curve deviates significantly from that of a blackbody. Fig. 4.2 shows the spectral energy distribution of the M8.3 giant IRC-20563 and the black body curve at the derived T_{eff}. Signatures of molecular opacities are seen in the shorter wavelength part of the distribution which clearly deviates from the black body curve. The longer wavelength IR excess is also apparent from this figure. Hence, the only direct means of obtaining the effective temperature of the star is from the measured angular diameter and the bolometric flux. This gives a hypothesis-free value of the T_{eff} which is completely independent of the distance to the star and hence is a powerful tool to test theoretical models on a large sample of stars.

The T_{eff} scale, i.e the calibration of the T_{eff} with spectral classification of the stars is of prime importance in investigating stellar populations and is also potentially useful in galactic and extragalactic studies. For early spectral types, this scale is well established either empirically or from suitable models. Barnes & Evans (1976) have shown a correlation between the visual surface brightness and the colours which gives an accurate estimate of the temperature of stars of early spectral type. Initially, lunar occultation and, more recently, long baseline interferometry results, have progressively contributed towards the accumulation of reliable values for the stellar angular diameters of late type stars and have pushed the calibration of T_{eff} scale to late M spectral types. Ridgway et al. (1980) were the first to give the temperature calibration from K0 to M6 based on lunar occultation

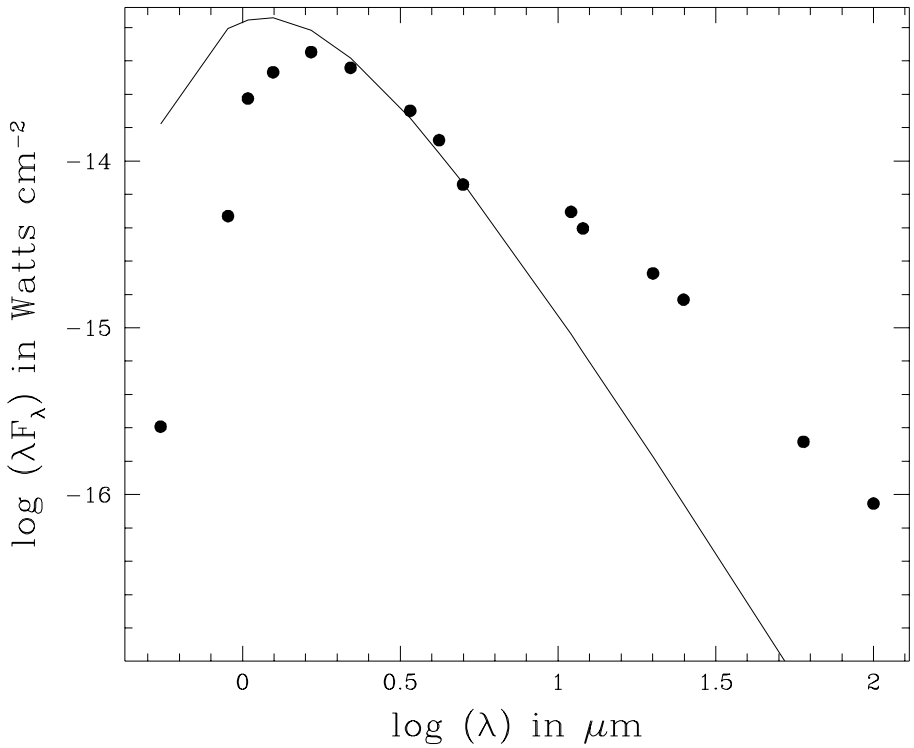

Figure 4.2: The spectral energy distribution for IRC-20563. The solid curve is the blackbody of 3100 K.

diameter measurements of 31 giants of luminosity class III and II mainly in the H band. Prior to this calibration the most widely accepted one was given by Johnson (1966) which was based on broad band multicolour photometry. He gave the mean T_{eff} values from the study of 225 stars of luminosity class III and ranging in spectral type from G5 to M6 . Hayes (1978) too derived a temperature scale based on occultation diameters. The temperatures derived by Ridgway et al. (1980) agree well with that of Johnson (1966) for K0 – K3 but an appreciable departure is seen beyond this. For M type stars their calibration gives a hotter temperature scale than Johnson's. For K4 the scale derived by Ridgway et al. (1980) is higher by 85 K and this difference increases with later spectral type and becomes $\sim$ 450 K for M6. This scale is even hotter than that derived by Hayes. The results obtained by Ridgway et al. (1980) show a lot of scatter. Nevertheless, it is a great pioneering work and the mean temperature scale derived is consistent with the more recent calibrations. About a decade later calibrations derived from the results of long

baseline interferometry began to appear. Di Benedetto & Rabbia (1987) give a temperature scale for stars cooler than K0 and upto M3 based on measurements taken at CERGA by Michelson interferometry. Their calibration is based on diameter measurements of 11 giant stars ranging from K0 to M3. With an internal accuracy of $\pm$65 K their derived T_{eff} matches well with that of Ridgway et al. (1980) outside the spectral class of M0 – M2, but yields a significantly lower temperature ($\sim$ 160 K) for the M0 spectral type. Later, additional results by Dyck et al. (1996) based on IOTA measurements of 29 K and M giants extended the calibration to spectral type M7 with an estimated uncertainty of $\pm$95 K for each spectral type. Dyck et al. (1998) give the temperature scale based on new visibility data from IOTA. This includes 74 evolved stars of luminosity class II and III. The effective temperartures derived by them fall in the same band as that of Ridgway et al. (1980) and there is a uniform mix of the two data sets. Combining these results with that of Dyck et al. (1996) and Ridgway et al. (1980) gives a data base of 91 stars of luminosity class III. Of these, 83 stars approximately define a linear relationship between the effective temperature and the spectral type with a mean dispersion of 192 K at each spectral type. The other eight yield temperatures which are $\sim$ 750 K lower for their spectral type. A linear decrease of temperature is seen from spectral type G8 to M8. The fitted regression is of the form

$$T_{eff} = -106 \text{ ST} + 4580 \text{ K} \tag{4.1}$$

where the index ST has the values -2,...,0,...,5,6,...,8, corresponding to spectral classes G8,...,K0,...,K5,M0,...,M8, respectively. Perrin et al. (1998) too derive an extension of the temperature scale beyond M6. They have used the effective temperature of nine stars derived from the FLOUR beam combiner on the IOTA interferometer. Their result agrees well with that of Ridgway et al. (1980) and the temperatures of stars later than M6 are found to extend well the occultation data law. In a recent work, van Belle et al. (1998) give a temperature calibration which is consistent with that of Dyck et al. (1998). They have used interferometrically determined angular

diameter of 69 evolved stars at the PTI. They obtain a linear relation given by

$$T_{eff} = -109 \text{ ST} + 4570 \text{ K} \tag{4.2}$$

The fit is statistically identical to that obtained by Dyck et al. (1998) and is only marginally cooler ($\sim$ 60 K) for the the later spectral type M7.

A homogeneous temperature calibration, ensuring uniformity in details of data acquisition and analysis, has been recently reported by Richichi et al. (1999). It is based on lunar occultation diameters at 2.2 μm of 32 giant stars in the spectral range K0 to M10 which also includes 4 Miras. For their derived effective temperatures a cubic curve best represents the relation between the spectral type and the T_{eff}. However, seven stars in their sample (between K1 and M8) exhibit significantly lower temperature values ($\sim$ 900 K).

A consistent temperature calibration for the M type giants is difficult to establish. There are mainly three parameters involved in doing so. The spectral class of the source, the bolometric flux and the angular diameter. All three of them have few uncertainties attached with them. These uncertainties may be due to the difficulties in measuring or estimating these quantities or it may be related to the basic definition or it may be due to the complications arising from the intrinsic nature of the sources. The problems associated with each are discussed briefly below.

4.2 Uncertainties involved in T_{eff} calibration

4.2.1 Spectral Classification

In order to obtain a well defined temperature scale one should have accurate spectral classification of the sources under study. It is noted that the spectral classifications from the sources consulted are not entirely consistent. Discrepancies such as multiple classification for the same star, inconsistency with the observed colours or accuracy of the original source of classification are seen. The intrinsic variability of the star also changes the spectral type.

It is the molecules that give the spectra of M type stars their very charateristic banded appearance. The difficulties with having an accurate classification for this group of stars are:

- Lack of proper standards.
- Variability of the source.
- The range K4 to M1 offers most difficulties because TiO bands just begin to be visible and can be confused with nearby groups of atomic lines unless very high dispersion is used.
- Absorption bands of TiO become very strong beyond M4, hence it becomes difficult to find stretches of continuum where atomic lines can be reliably compared.
- Early M types have problems of TiO line blanketting.

Moreover, all these classifications are based on observations restricted to the visual or very NIR ($\sim 1.06\,\mu m$). For M giants this part of the spectrum is very sensitive to stellar conditions. The continuum is high, line opacity effects are large and also this region lying on the exponential part of the Planck's curve is quite sensitive to temperature. If IR spectra in the 1.0-3.0 μm region are used then the classification will be more reliable. Opacities being less, emission from a deeper and more stable part of the atmosphere can be sampled. This spectral region offers strong absorption lines like the CO overtone bands, FeI, NaI doublets, CaI triplet, MgI etc as spectral type indicators. But there is still no consensus in the literature on spectral typing based on infrared high resolution spectra. This uncertainty in the spectral classification makes it difficult to get a well defined calibration of the temperature versus the spectral type.

Table 4.1: Derived JHK magnitudes for our sample of M giants.

Source	JD	J	H	K
IRC-10301	2450590.5	2.77±0.03	1.85±0.03	1.56±0.03
IRC-10305	2450590.5	3.47±0.03	2.63±0.03	2.37±0.03
IRC+10032	2450473.5	3.82±0.03	2.90±0.03	2.64±0.03
IRC+10034	2450473.5	2.60±0.03	1.65±0.03	1.28±0.03
IRC+10194	2450916.5	3.04±0.02	2.18±0.03	1.87±0.03
IRC+20125	2450473.5	3.96±0.03	3.00±0.03	2.75±0.02
IRC+20111	2450473.5	2.66±0.03	1.72±0.03	1.35±0.03
IRC+20090	2450482.5	4.16±0.02	3.11±0.03	2.79±0.03
IRC-10580	2450590.5	1.84±0.02	0.85±0.03	0.47±0.03
IRC-20299	2450590.5	3.46±0.04	2.47±0.03	2.13±0.03
IRC-10308	2450919.5	1.44±0.03	0.46±0.03	0.15±0.03

4.2.2 Bolometric Flux

Inspite of the relatively weak (1/4th. power) dependence of T_{eff} on the bolometric flux, its accurate determination is an important criteria to get a reliable temperature scale. Bolometric fluxes are usually obtained by applying a bolometric correction to the measured V magnitudes. But this method fails for cool stars where the bolometric corrections are large and very sensitive to the spectral type. These cool stars radiate predominantly in the NIR, hence photometry in this critical spectral region where their flux distribution peaks helps in deriving the bolometric flux directly. We have carried out JHK photometry of most of the stars in our sample. The JHK magnitudes obtained by us are listed in Table 4.1. In case of the sources for which we failed to obtain an accurate JHK photometry, we have taken the magnitudes from the available literature. To complete the flux distribution curve, we have taken the other optical and infrared magnitudes from reliable published

sources. For the longer wavelength part of the curve we have consulted IRAS PSC and Gezari et al. (1993). We obtain the bolometric flux by either integrating from $\lambda = 0$ to $\lambda = \infty$ under the black body distribution curve after matching with the observed flux at 2.2 μm or by a simple trapezoidal rule. Both give consistent values.

Ideally, one should have the bolometric flux at the same epoch of the angular diameter measurement as these sources are known to be variables. But this has always not been possible. We have also used magnitude values which are spread over different epochs. Hence, the error in the bolometric flux includes the intrinsic variability of the source.

Feast et al. (1990) give a relation for interstellar extinction as follows

$$E(B-V) = 0.032\ (cosec|b| - 1)(1 - exp[-10\ r\ sin|b|]) \tag{4.3}$$

where, b is the galactic latitude and r is the distance to the source in kiloparsec. Taking,

$$A_V = 3.1E(B-V) \tag{4.4}$$

$$A_J = 0.265A_V \tag{4.5}$$

$$A_H = 0.155A_V \tag{4.6}$$

$$A_K = 0.090A_V \tag{4.7}$$

we derive the extinctions in different bands. Table 4.2 gives the source list with the derived extinctions and the distance estimates. The sources marked with a '$*$' have no parallax measurements available and hence the distance estimate of these sources are made using the absolute magnitudes given for their spectral class in Lang (1992). The uncertainty in the spectral classification of these sources is hence included in error of the distance estimates. As is seen from Table 4.2, the extinctions in the JHK bands are very nominal. As we are interested in the NIR part of the spectrum to derive the bolometric flux, the extinctions can be considered negligible since they are of the order of the errors involved in the magnitude estimation. Taking the case of IRC+20125 which has the highest extinction, we derive

Table 4.2: Derived extinction values for the M giants sample.

Source	Galactic latitude (Deg)	Distance (kpc)	A_V	A_J	A_H	A_K
IRC-10301	44.48	0.424	0.04	0.01	0.006	0.004
IRC-10305	43.32	0.459	0.04	0.01	0.007	0.004
IRC-10308	39.96	0.337	0.05	0.01	0.008	0.004
IRC-20299*	25.98	0.824	0.1	0.03	0.02	0.01
IRC-10580	-49.55	0.285	0.03	0.007	0.004	0.002
IRC+20067*	-28.47	0.870	0.1	0.03	0.02	0.01
IRC+10038*	-37.28	0.794	0.06	0.02	0.01	0.006
IRC+20125*	-3.65	0.631	0.5	0.1	0.07	0.04
IRC+10032	-45.58	0.637	0.04	0.01	0.006	0.004
IRC+10034*	-38.35	0.695	0.06	0.02	0.01	0.005
IRC+20111*	-8.32	0.525	0.3	0.08	0.04	0.03
IRC+10194	31.61	0.446	0.08	0.02	0.01	0.007

the bolometric flux after correcting for extinction and get difference of < 5 % in the absolute value, whereas the quoted errors in our bolometric fluxes is typically $\sim 10\%$. Hence, we conclude that our bolometric fluxes are free from bias of interstellar extinction. Circumstellar extinction is present in some of the giants in our sample (e.g. IRC-10580). In this case the absorbed photospheric radiation is re-emitted locally and shows up in the spectral energy distribution as an IR excess. A black body is fitted to this excess and added to the total stellar flux to get the original bolometric flux from the photosphere.

4.2.3 The Angular diameter

The data of most angular diameter observations are not reduced with specific limb darkening functions but with extreme assumptions of fully darkened or uniform

disks. The uniform disk assumption is a biased estimate of the real stellar diameter. Measuring a star's diameter by interferometric or lunar occultation technique amounts to observing the interference or diffraction pattern produced by the centre-to-limb variation or limb darkening of the intensity emitted by the star towards the observer. Reconstruction of this centre-to-limb variation from the occultation pattern is extremely difficult and has been attempted for very few stars (Richichi & Lisi 1990; Bogdanov & Cherepashchuk 1990) for which extremely good signal-to-noise ratio light curves are available. In practice, the amount of limb darkening is estimated from model atmospheres. In cool stars the separation of the total atmosphere into photosphere and outer (chromospheric, coronal, wind envelope,..) layers is not that well distinguished from each other and even the thickness of the photosphere may be non-negligible compared to the dimension of the star. In stars with compact photospheres the centre-to-limb variation curves drop steeply near the limb of the stellar disk and the stellar photospheric radius can be defined as the distance from the centre of the disk to where the intensity reaches a near zero level. Direct measurements refer to this intensity radii. But red giants are among those with geometrically extended photospheres. Hence, the radii should be defined for some particular and specific photospheric layer. Usually, one defines the physical radius of the star as the distance from the centre upto the point where the Rosseland mean opacity becomes unity. The diameter so derived is termed as the Rosseland diameter. This is a wavelength independent reference quantity which allows convenient comparison of the observed stars with the stellar interior models. But there exists no trivial correlation between the intensity radius and the Rosseland radius. The intensity radius depends on the monochromatic extinction coefficient at the wavelength of observation. Hence, it is customary to introduce wavelength dependent optical depth radii. But, for M giants the continuum forming layers are fairly compact regions because of the steep temperature increase of the absorption coefficient towards the deep layers (Scholz 1997). So conventionally, the Rosseland diameter is chosen and is the physical diameter refered to in this work.

Limb darkening affects the measurements of stellar diameters of cool stars mostly at visual wavelengths which are severely contaminated by molecular band absorption. In a recent work by Albrow et al. (1999), the novel method of gravitational lensing was used to derive limb darkening values for a K giant in the galactic bulge. They present the photometric dataset for the binary-lens microlensing event MACHO 97-BLG-28. Schmidtke et al. (1986) show that the effect of limb darkening in the NIR is typically around the 5% level. They have calculated the ratio of the limb darkened to the uniform disk diameter to be 1.028 in the K band for K4 giants and this value was adopted for other cool giants too. Perrin et al. (1998) fitted their interferometric data with limb darkened disk models (Manduca 1979; Scholz & Takeda 1987) in the K band in the 3000-4500 K range. They suggested a scaling factor of 1.035 to obtain the limb darkened diameter from the uniform disk value. This value of 1.035 has been adopted by us in deriving the stellar radii of our sample. At 2.2 μm this effect is well contained within the errors of this investigation but is included for completeness.

4.3 Results

In our sample of M giant stars we have 15 sources ranging from M2 to M9. The cross identification of the sources are given in Table 4.3. Table 4.4 gives the journal of observation and other source details. The spectral types listed in this table are the ones compiled from the literature. The dewar used for each event is also specified in this table. The CVF being a slower dewar, the light curve will appear to be more smoothened out in comparison with the ones obtained using the Fast dewar. The predicted parameters for the sources are listed in Table 4.5. The non linear least squares method described in Chapter 2 has been used for analysing these light curves. Among other parameters, the model is a function of the angular diameter ϕ. For resolved sources, the least squares fitting procedure converges towards an angular diamter value which gives minimum χ^2. For an unresolved

Table 4.3: Cross identification for our M giant sample.

Serial No.	TMSS	SAO	IRAS	HD	Other Names
1.	IRC-10301	158431	14104-1337	124304	EV Vir
2.	IRC-10305	158493	14165-1410	125357	MZ Vir
3.	IRC-20299	159577	15527-1838	142521	-
4.	IRC+10032	93166	02508+1427	17973	-
5.	IRC+10034	93196	02541+1424	18310	-
6.	IRC+10194	98143	08459+1243	75156	FX Cnc
7.	IRC+10038	-	03073+1315	-	ST Ari
8.	IRC+20067	93659	0351+1527	-	-
9.	IRC+20090	-	04410+1752	-	-
10.	IRC+20111	94604	0528+1831	36321	DV Tau
11.	IRC-10580	146043	22190-0751	212062	DZ Aqr
12.	IRC-10308	158929	14550-1214	132112	FY Lib
13.	IRC-20444	-	18090-1853	-	-
14.	IRC-20470	-	18197-1925	-	-
15.	IRC+20125	94956	05502+1856	248740	-

source ($\leq$ 2 mas in our case) it remains flat upto the resolution limit and then increases monotonically with diameter. This χ^2 convergence test was done for all the sources. This is shown as an inset in all the figures showing the data and the model fit to it. We broadly divide these 15 sources into two categories - the resolved sources (11) and the unresolved sources (4).

Table 4.4: Journal of observations and source details for the M giant sample.

Source Name	Date of Obsn.	Event Type	Dewar Used	Spectral Type	V	K	Hipparcos Parallax (mas)
IRC-10301	1995 Mar 20	R	Fast	M5 II M3 III M4.5 II-III	7.2	1.56	2.36±1.20
IRC-10305	1995 Mar 20	R	Fast	M1-M3 III	7.5	2.37	2.18±0.98
IRC-20299	1995 Jun 11	D	Fast	M4 III	9.08	2.13	-
IRC+10032	1995 Dec 04	D	Fast	M	7.58	2.64	1.57±1.06
IRC+10034	1995 Dec 04	D	Fast	M4 III	8.71	1.28	-
IRC+10194	1996 May 23	D	Fast	M3.3 III M3 III-II	6.8	1.87	2.24±1.08
IRC+10038	1997 Jan 17	D	CVF	M4	9.0	2.37	-
IRC+20067	1997 Feb 14	D	CVF	M2	9.1	2.75	-
IRC+20090	1996 Feb 26	D	Fast	M6	∼11	2.79	-
IRC+20111	1996 Feb 27	D	Fast	M6	8.4	1.35	-
IRC-10580	1996 Nov 18	D	Fast	M7	8.52	0.47	3.51±1.26
IRC-10308	1998 Jan 22	R	CVF	M5 III	7.1	0.15	2.97±1.19
IRC-20444	1996 May 06	R	Fast	M9	-	1.69	-
IRC-20470	1995 Mar 24	R	Fast	M7	-	2.36	-
IRC+20125	1995 Apr 06	D	Fast	M5	8.70	2.75	-

Table 4.5: Predicted circumstances of the events for the M giant sample.

Source	Time (UT) (hh mm ss)	Alt. of star (deg)	PA[1] (deg)	CA[2] (deg)	Vel. comp. (km/s)
IRC-10301	19 52 26	44.2	297.39	183.02	0.7255
IRC-10305	23 53 53	39.1	304.57	198.91	0.6746
IRC-20299	18 29 33	45.3	96.12	-3.07	0.6807
IRC+10032	14 11 00	46.7	18.79	-49.09	0.4741
IRC+10034	16 08 35	71.7	108.92	40.81	0.4591
IRC+10194	15 34 35	36.1	104.32	-8.23	0.7557
IRC+10038	13 01 29	66.1	102.2	34.58	0.5343
IRC+20067	17 07 04	37.1	60.59	-24.02	0.6945
IRC+20090	16 20 49	49.7	81.43	-9.53	0.6510
IRC+20111	13 22 35	76.8	69.06	-16.72	0.5337
IRC-10580	16 16 39	39.7	76.52	12.89	0.7446
IRC-20444	23 16 34	44.4	300.09	216.56	0.5333
IRC-20470	24 40 17	44.5	297.15	212.35	0.5395
IRC+20125	14 56 56	49.6	115.69	14.70	0.6492
IRC-10308	01 32 37	52.0	310.00	18.7	0.571

1. Position Angle 2.Contact Angle.

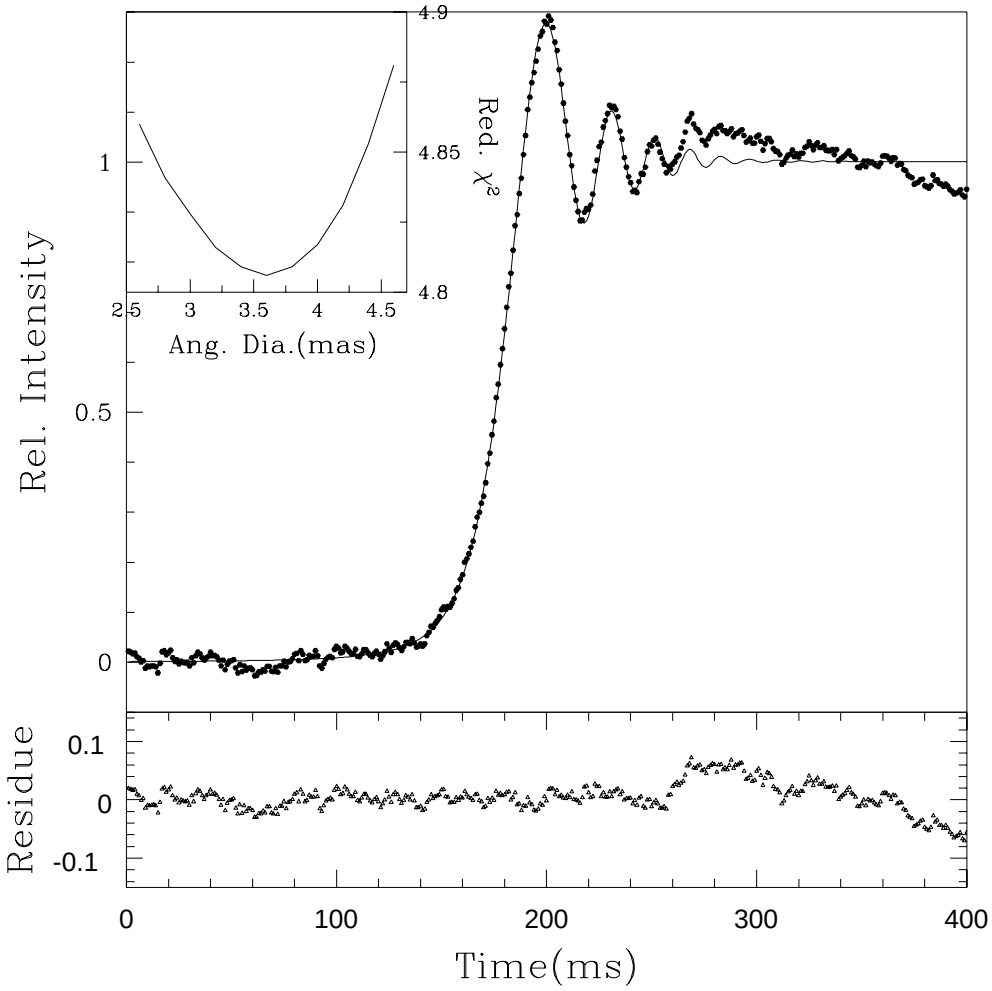

Figure 4.3: The data (dots) with the model fit to it (solid line) for IRC-10305. The inset shows the χ^2 convergence. The lower panel shows the residuals of the fit.

4.3.1 Resolved Sources

IRC-10305

It is classified as a M2/M3 giant. The occultation was recorded through thin clouds but it is possible to make a good fit to the first three fringes. The light curve alongwith the model fit to it is shown in Fig. 4.3. Addition of polynomials (either ordinary or Legendre) does not improve the quality of the fit. We obtain an angular size of 3.6±0.2 mas. This is the first angular diameter measurement of this source. The derived effective temperature is 2883±108 K. Using the recent Hipparcos parallax of 2.18±0.98 mas, we have derived a linear radius of 178±80 $R_\odot$.

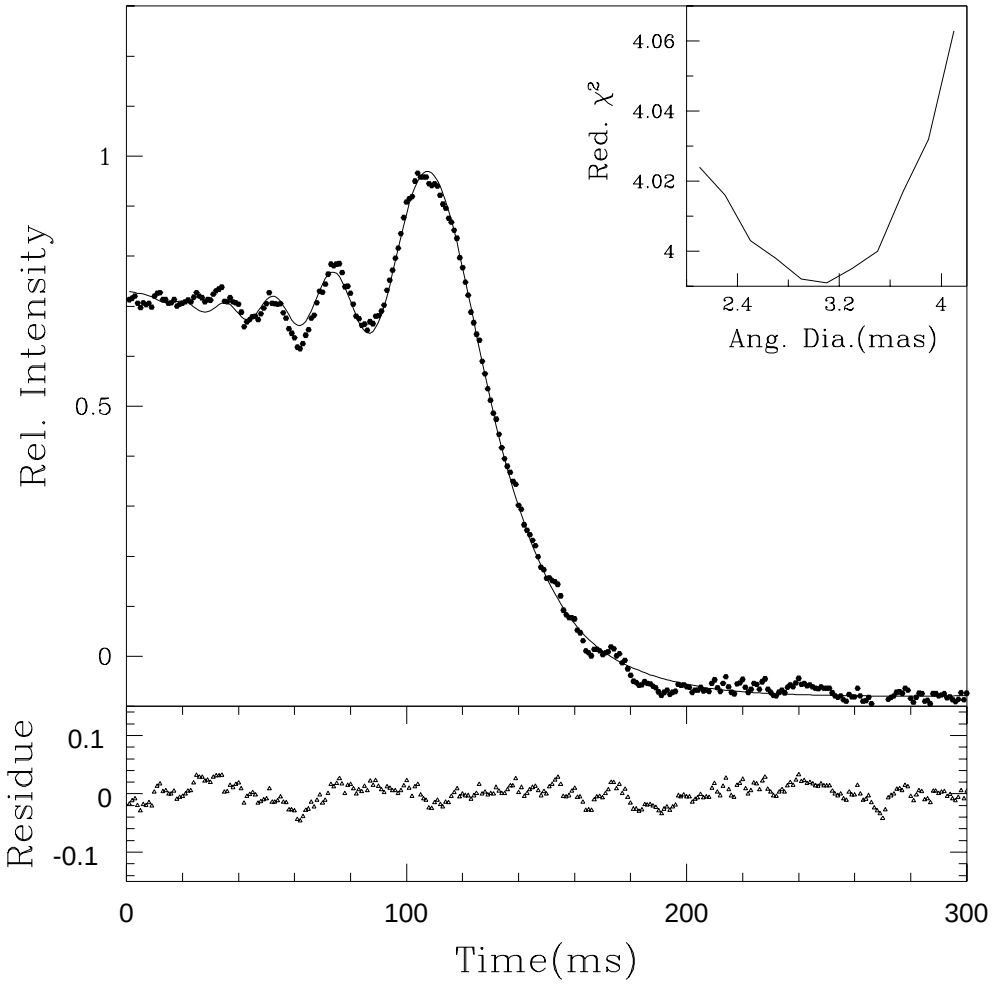

Figure 4.4: The data (dots) with the model fit to it (solid line) for IRC-20299. The inset shows the χ^2 convergence. The lower panel shows the residuals of the fit.

IRC-20299

This source is classified as M4 III. But from the colours given in Perrin et al. (1998) this source falls in the spectral class M6 – M8. The sky condition prevailing during the event was less than optimum. Portion of the light curve just before the event is noisy and hence only a truncated part of the light curve relatively free from fluctuation is used for data analysis. A linear slope is used to account for the varying background level and a 3rd order Legendre polynomial is used to account for the noise due to scintillation. We obtain a size of 3.1±0.4 mas for this source. This is

the first HAR observation of this source. The occultation light curve with the uniform disk model fit to it is shown in Fig. 4.4. The effective temperature is derived to be 3140 $\pm$216 K.

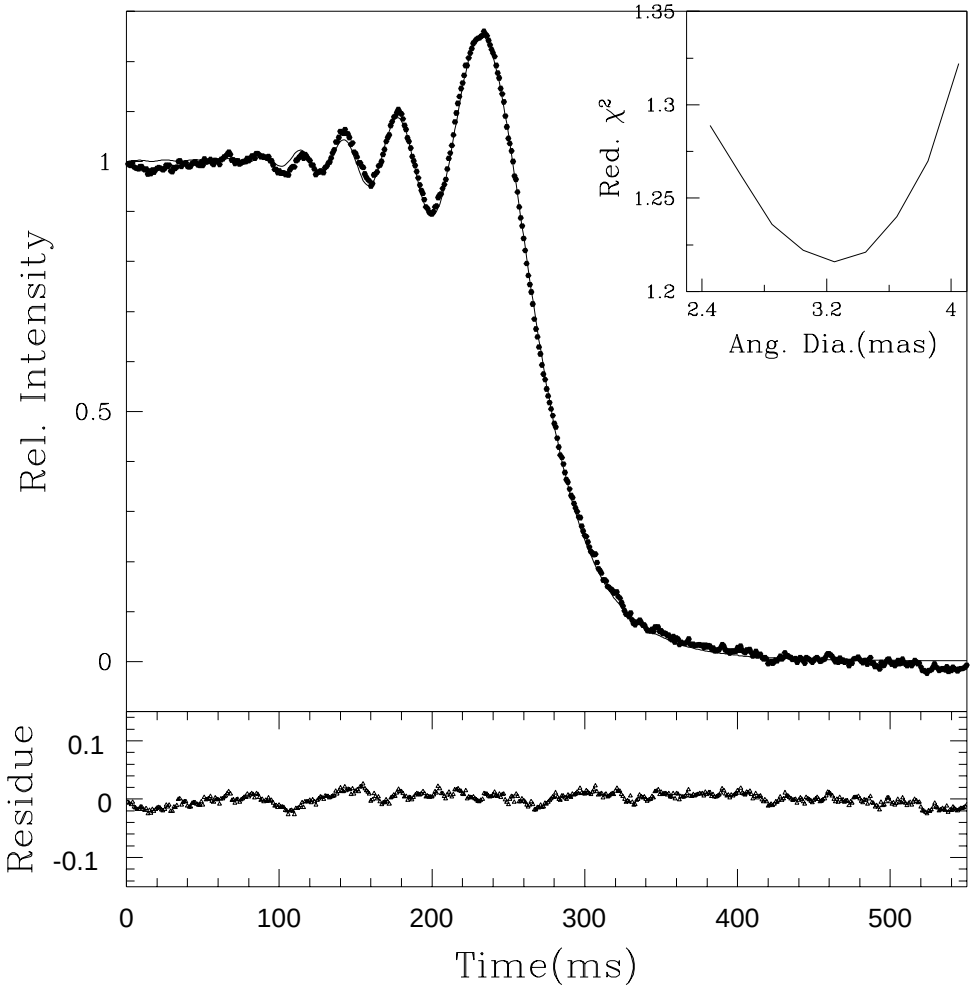

Figure 4.5: The data (dots) with the model fit to it (solid line) for IRC+10034. The inset shows the χ^2 convergence. The lower panel shows the residuals of the fit.

IRC+10034

IRC+10034 is classified as M4 III by Lahula (1987). Comparing the $(V-K)$, $(J-K)$ and $(H-K)$ colours with that listed in Perrin et al. (1998) gives a later spectral type (M6 – M8) for this source. We have a good quality light curve shown in Fig. 4.5. A slope is used to take care of the background variation. We obtain an angular diameter of 3.3$\pm$0.3 mas for this source. This value of the uniform disk diamter

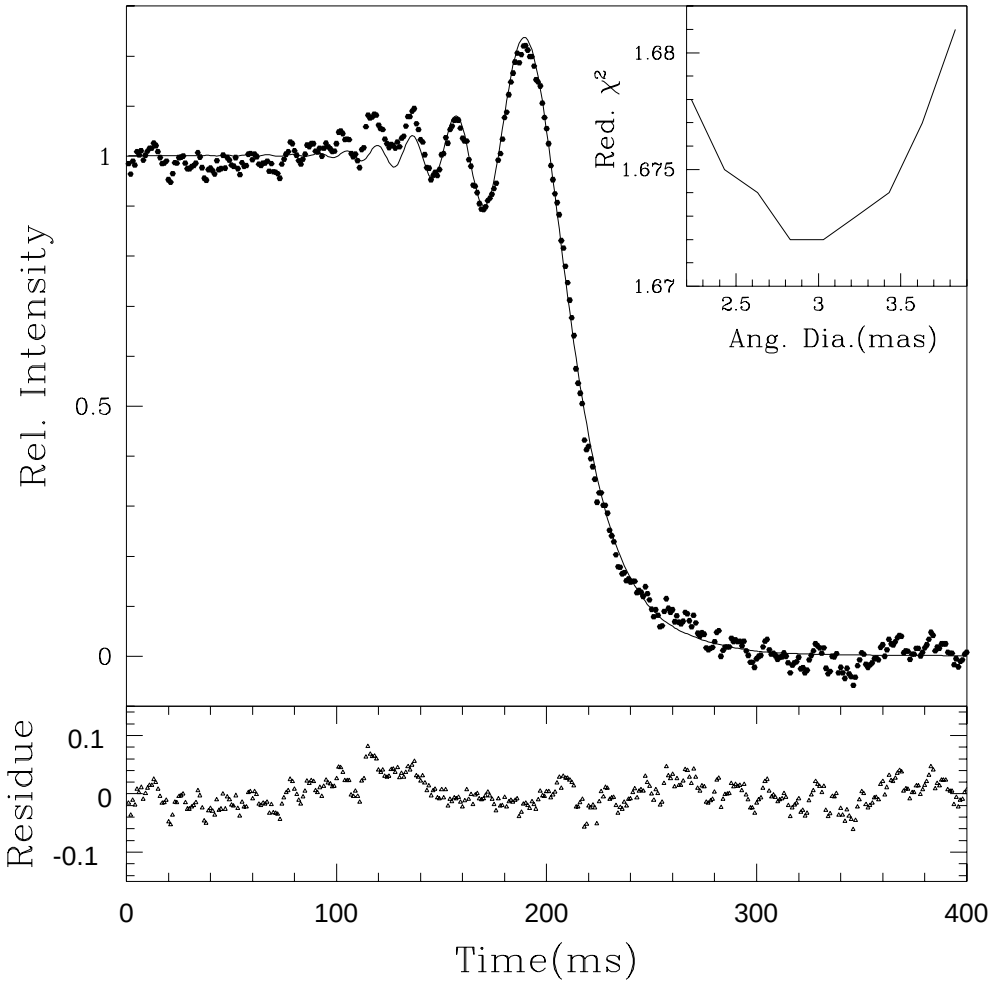

Figure 4.6: The data (dots) with the model fit to it (solid line) for IRC+10194. The inset shows the χ^2 convergence. The lower panel shows the residuals of the fit.

is consistent with that obtained by Richichi et al. (1998a). They quote a value of 3.64±0.07 mas. We derive an effective temperature of 3556±186 K for this source.

IRC+10194

This source is classified as M3.3 III by Kenyon & Fernandez-Castro (1987). The other classification is of M3 II-III (Keenan & McNeil 1989). There are several lunar occultation diameter measurements for this source. The journal of these previous values is given in Table 4.6. The light curve is shown in Fig. 4.6. As can be seen the light curve is affected by fluctuations due to thin clouds. Addition of polynomials

does not improve the quality of the fit. We get a uniform disk value of 3.0±0.3 mas and effective temperature of 3453±244 K for IRC+10194. Within errors this temperature is consistent with the spectral type M3 (Ridgway et al. 1980; Dyck et al. 1996). The spectral type and colour correlation is inconsistent for this source. The $(V-K)$ and $(J-H)$ colours are consistent with the current classification whereas the $(J-K)$ and the $(H-K)$ colour indices suggest a spectral type around M6 – M7 based on the classification of Perrin et al. (1998).

The relatively large diameter value obtained for this source by Ridgway et al. (1980) and Ragland et al. (1997a) translated to low temperatures of 2810±110 K and 2760±170 K respectively. These temperature values alongwith the infrared colours from Ridgway et al. (1980) displaced this source from the non-Mira M type stars towards the Mira type variables in the log T_{eff} versus the $(J-K)$ colour plot of Feast (1996). Similar displacement was also seen in the $(J-H)$ versus the $(H-K)$ diagram. But, this source is not a known Mira type variable.

Our photometric colours and derived effective temperatures however place it in the non-Mira strip. This suggests that this source might have been a Mira in the past (Feast 1996) and leaves open the possibility of a real change in the star between the two epochs of observations.

From the Hipparcos parallax of 2.24±1.08 mas we derive a linear radius value of 144±71 $R_{\odot}$ for this source.

IRC+10038

It is of spectral type M4. It is classified as a semiregular variable of type SRb (Kercshbaum & Hron 1994). Jura & Kleinman (1992) give a period of 99 days for IRC+10038 and a visual magnitude of 9.0. A variability in the visual range of amplitude ∼1.6 is also reported by them. The IRAS low resolution spectra is featureless. Except for a low frequency modulation seen after the fourth fringe, we have a good S/N ratio light curve. The data alongwith the model fit to it is shown

in Fig. 4.7. We obtain an angular size of 3.0±0.2 mas which is the first diameter measurement for this source. We derive an effective temperature of 3098±138 K. The infrared colour indices suggest a later spectral type for this source. The derived spectral type is between M5.5 – M8.

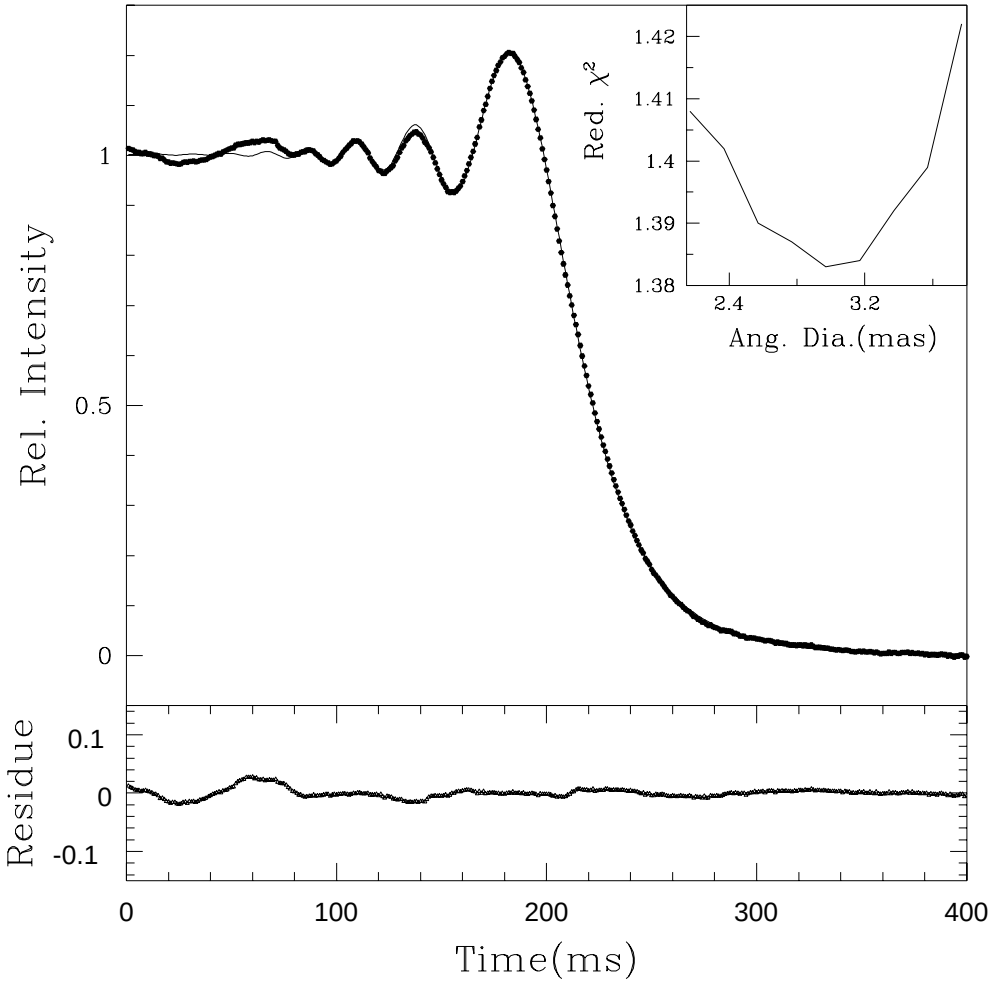

Figure 4.7: The data (dots) with the model fit to it (solid line) for IRC+10038. The inset shows the χ^2 convergence. The lower panel shows the residuals of the fit.

IRC+20067

This source is classified as M2. The light curve has large fluctuations due to bad sky conditions. Only a truncated part of the curve is used for analysis. Detailed data analysis yield a uniform disk angular diameter of 5.4±0.4 mas. A 4th order

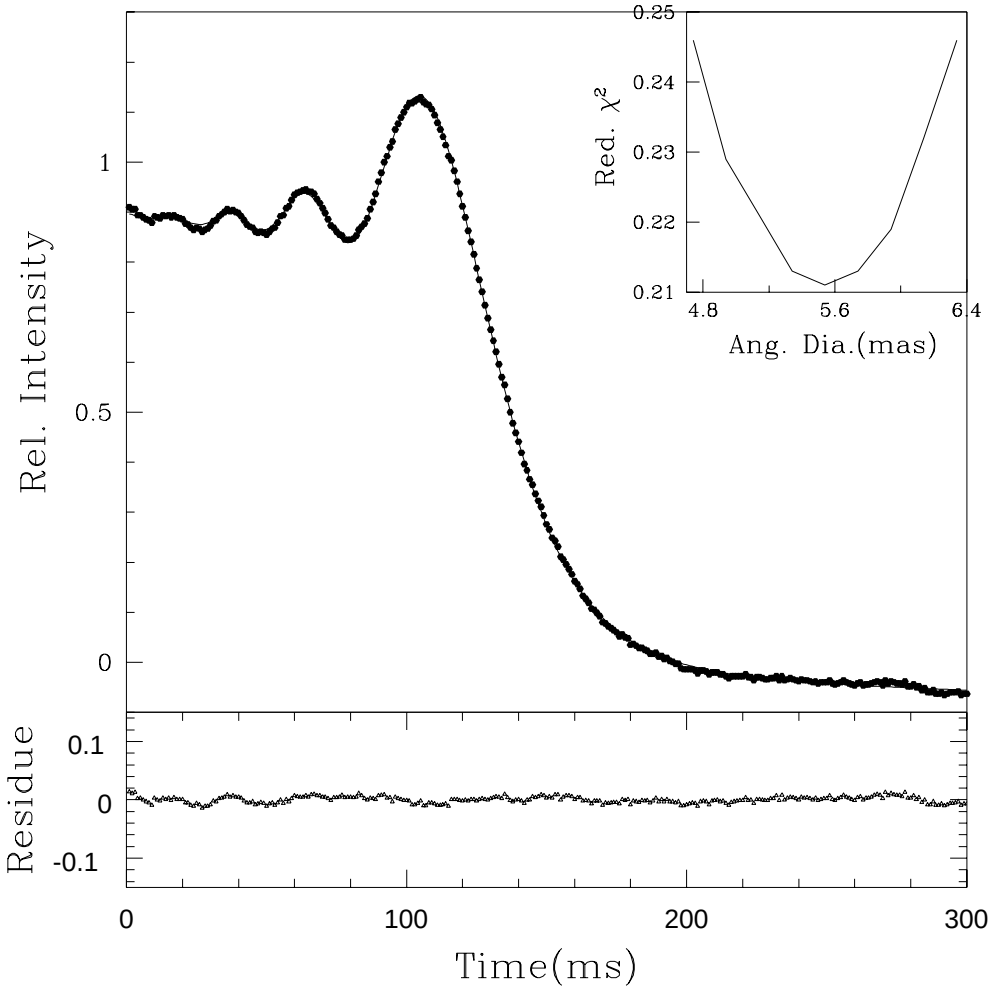

Figure 4.8: The data (dots) with the model fit to it (solid line) for IRC+20067. The inset shows the χ^2 convergence. The lower panel shows the residuals of the fit.

Legendre polynomial was used to account for the noise present in the data. The light curve and the model fit is shown in Fig. 4.8. Richichi et al. (1998b) quote a lower value of 3.68$\pm$0.24 mas for the angular size of IRC+20067. We derive an effective temperature of 2244$\pm$101 K. This temperature is appreciably low for this spectral type. However, the colour classification scheme of Perrin et al. (1998) puts this source between M7 – M8. In the log T_{eff} versus the $(J-K)$ colour index plot of Feast (1996), this source occupies a position in the Mira zone. Hence, one can speculate on this being a Mira type variable. That will adequately explain the low temperature obtained.

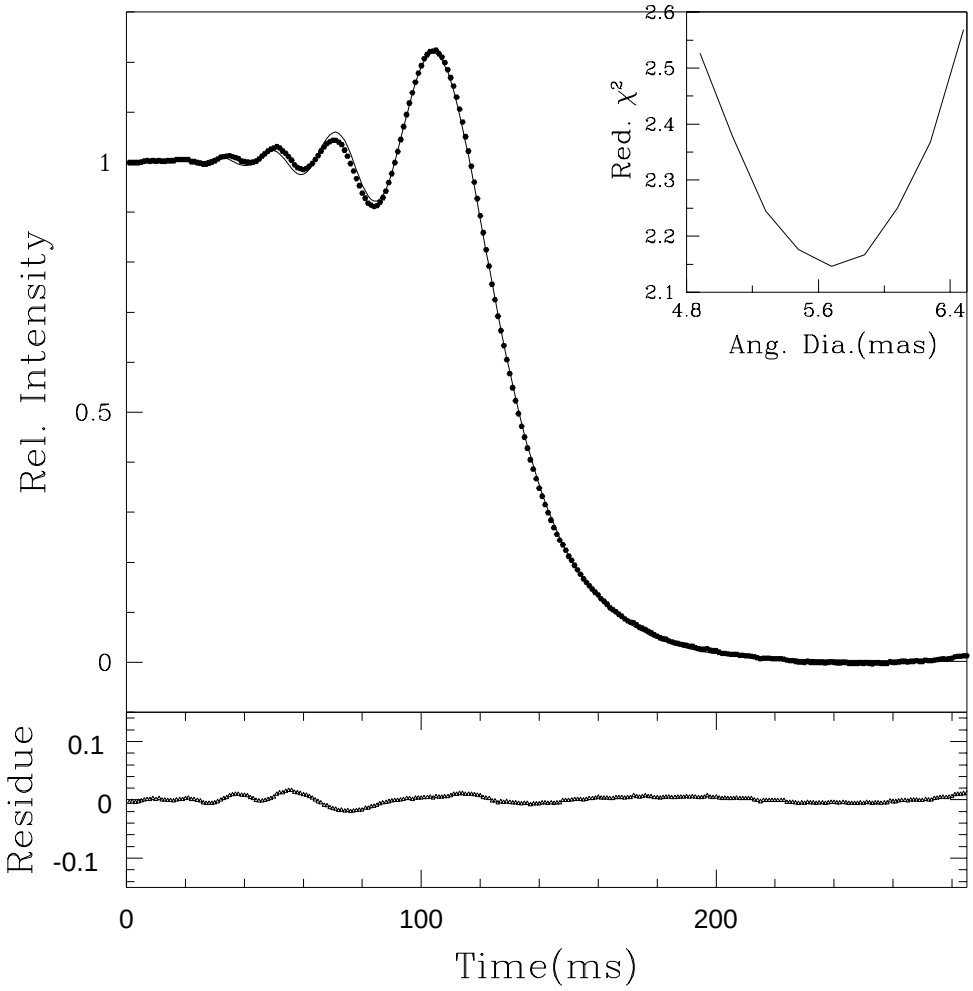

Figure 4.9: The data (dots) with the model fit to it (solid line) for IRC-10580. The inset shows the χ^2 convergence. The lower panel shows the residuals of the fit.

IRC-10580

IRC-10580 is a semiregular oxygen rich variable. Whitelock et al. (1995) list it as a M7 giant. The IRAS LRS spectra shows a strong and broad 10 μm emission feature. Hashimoto (1994) has fitted a radiative transfer model to the IRAS colours and the 10 μm silicate feature. He obtains an inner dust shell radius of $40R_\star$ at temperature 465 K and an outer dust shell of radius $1000R_\star$. Volk & Kwok (1987) derive a dust temperature of 515 K from the IRAS fluxes. From the model fit of the 60μm and 100μm data to a central unresolved source surrounded by a resolved isothermal shell, Young et al.(1993) have shown that DZ Aqr is not extended.

The light curve recorded has large low frequency scintillation present but the event portion was relatively free from this. We get a uniform disk value of 5.7±0.4 mas. Appropriate polynomial is used to account for the varying background and a 2nd order Legendre polynomial is used to take care of the distortions due to scintillation. Fig. 4.9 shows the light curve and the model fit to it. No previous diameter estimate exists for this source. Radick & Lien (1980) mention about a lunar occultation of IRC-10580 but have also remarked that the diameter of 9.6±1.3 mas obtained from the analysis of their data is possibly spurious. We estimate an effective temperature of 3088±134 K for this source. This temperature is consistent with the temperature derived for this spectral type by Perrin et al. (1998). The IR colours are also consistent with the spectral type assigned to this source.

Using the recent Hipparcos parallax measurement for IRC-10580 of 3.51±1.26 mas, we obtain a linear radius value of 175±64 $R_{\odot}$.

IRC+20111

DV Tau is classified as M6 (Bidelman 1980). The IRAS-LRS spectra of this source is featureless. The data and the non linear least squares fit to it is shown in Fig. 4.10. There is a distortion seen in the third fringe but other than this the fit is of good quality. We get an angular diameter value of 3.2±0.4 mas. Earlier, Ridgway et al. (1982) have resolved this source from lunar occultation observation at 1.618 μm. They get a UD value of 3.38 ±0.19 mas. Richichi et al. (1998b) give a 2.2 μm angular diameter value of 3.79±0.13 mas for IRC+20111. Within quoted errors our value is consistent with these two measurements. We derive a temperature of 3318±222 K, which is consistent with the temperature calibration for this spectral type. The IR colours assign a spectral type M7 – M8 to this source.

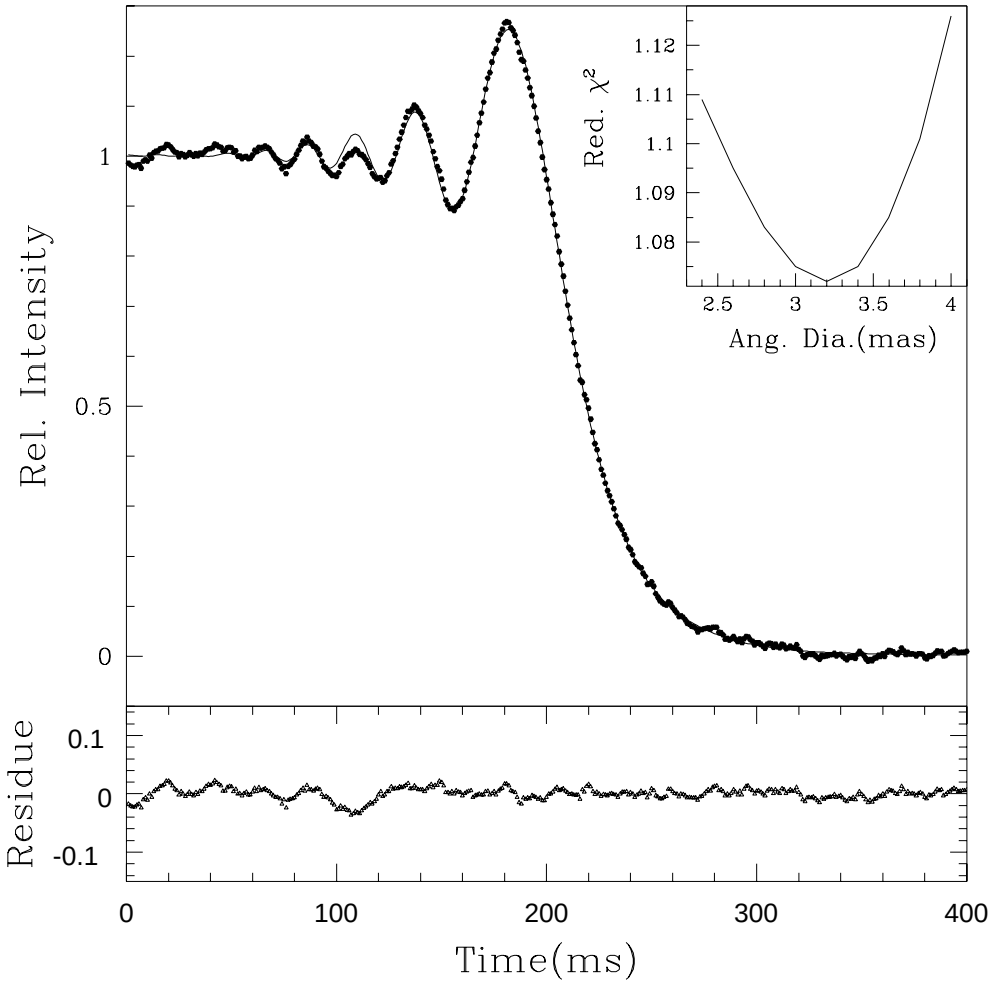

Figure 4.10: The data (dots) with the model fit to it (solid line) for IRC+20111. The inset shows the χ^2 convergence. The lower panel shows the residuals of the fit.

IRC+20090

This source is classified as M6 (Bidelman 1980). This oxygen rich giant has no previous angular diameter measurements. JHK and narrow band photometry by Noguchi (1989) show the signature of the strong 2.7 μm H_2O absorption band common to late type stars with oxygen rich envelopes. The light curve is shown in Fig. 4.11. We obtain an angular size of 3.7$\pm$0.3 mas and temperature of 2533$\pm$123 K. This temperature is significantly low for this spectral type. However, our infrared colours place it in the Mira zone of the log T_{eff} versus $(J-K)$ plot of Feast (1996) and assign a later (M8) spectral type consistent with the colour classification of

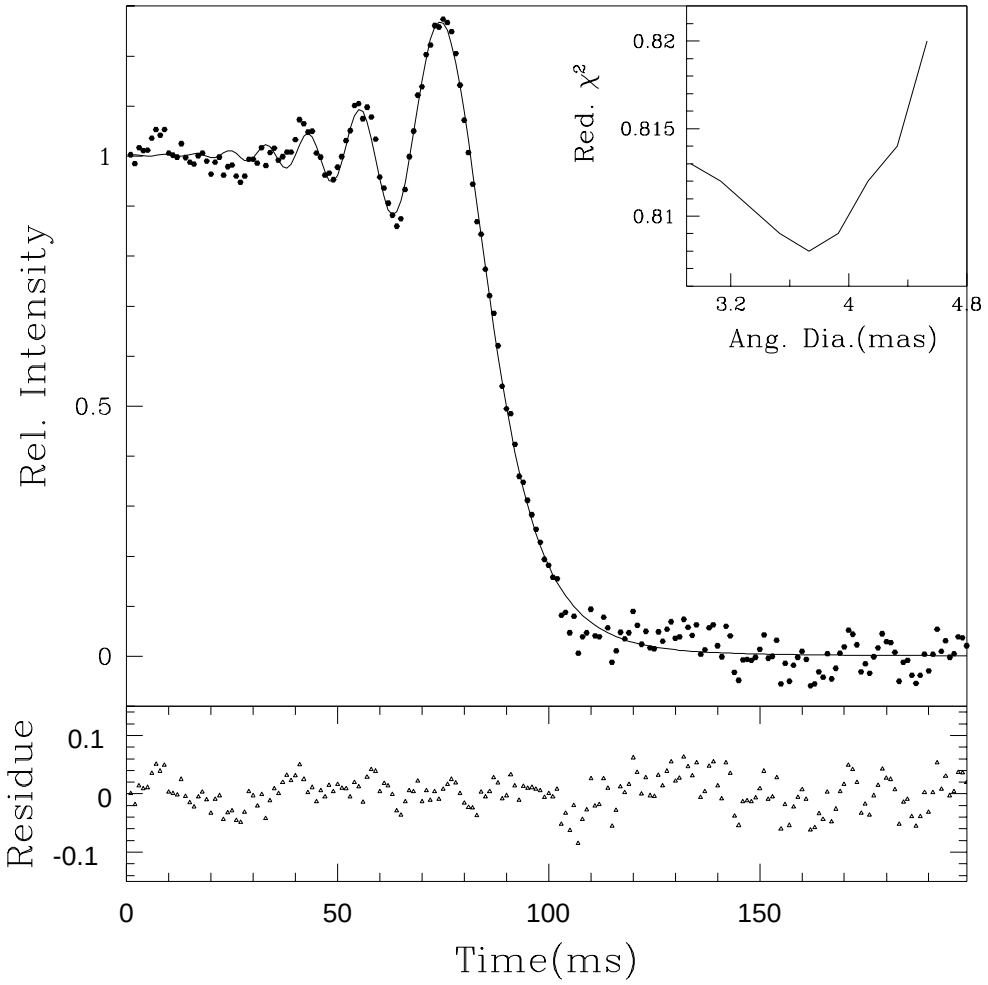

Figure 4.11: The data (dots) with the model fit to it (solid line) for IRC+20090. The inset shows the χ^2 convergence. The lower panel shows the residuals of the fit.

Perrin et al. (1998). Further monitoring of this source will be very interesting.

IRC-20444

Hansen & Blanco (1973) classify it as M8 or later. The other classification is M9 by Volk & Cohen(1989). This is the latest spectral type in our sample. The IRAS LRS shows a broad 9.7 μm silicate emission feature. From a previous lunar occultation of this source Richichi et al. (1998b) give a uniform disk angular diameter of 4.54$\pm$0.06 mas and an effective temperature of 2636$\pm$132 K for this source. We have a relatively poor light curve as shown in Fig. 4.12. We obtain a uniform disk

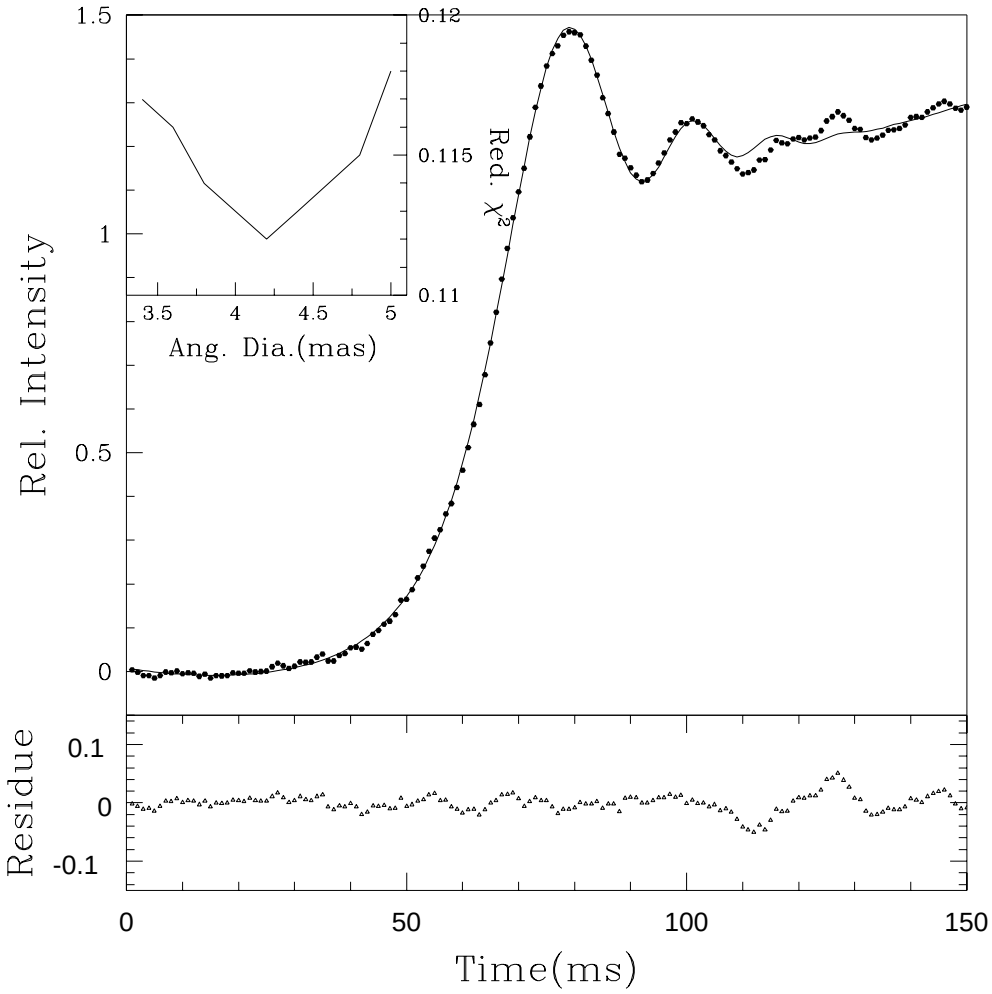

Figure 4.12: The data (dots) with the model fit to it (solid line) for IRC-20444. The inset shows the χ^2 convergence. The lower panel shows the residuals of the fit.

value of 4.2±0.5 mas. The fit shown in the figure is the best possible. We have used a 2nd order Legendre polynomial to account for the distortion. Increasing the order of the polynomial did not improve the fit and moreover abrupt changes in the shape of the polynomial started becoming dominant with the increase in the order. With the bolometric flux listed in Richichi et al. (1998b) we derive an effective temperature of 2788±215 K for this source.

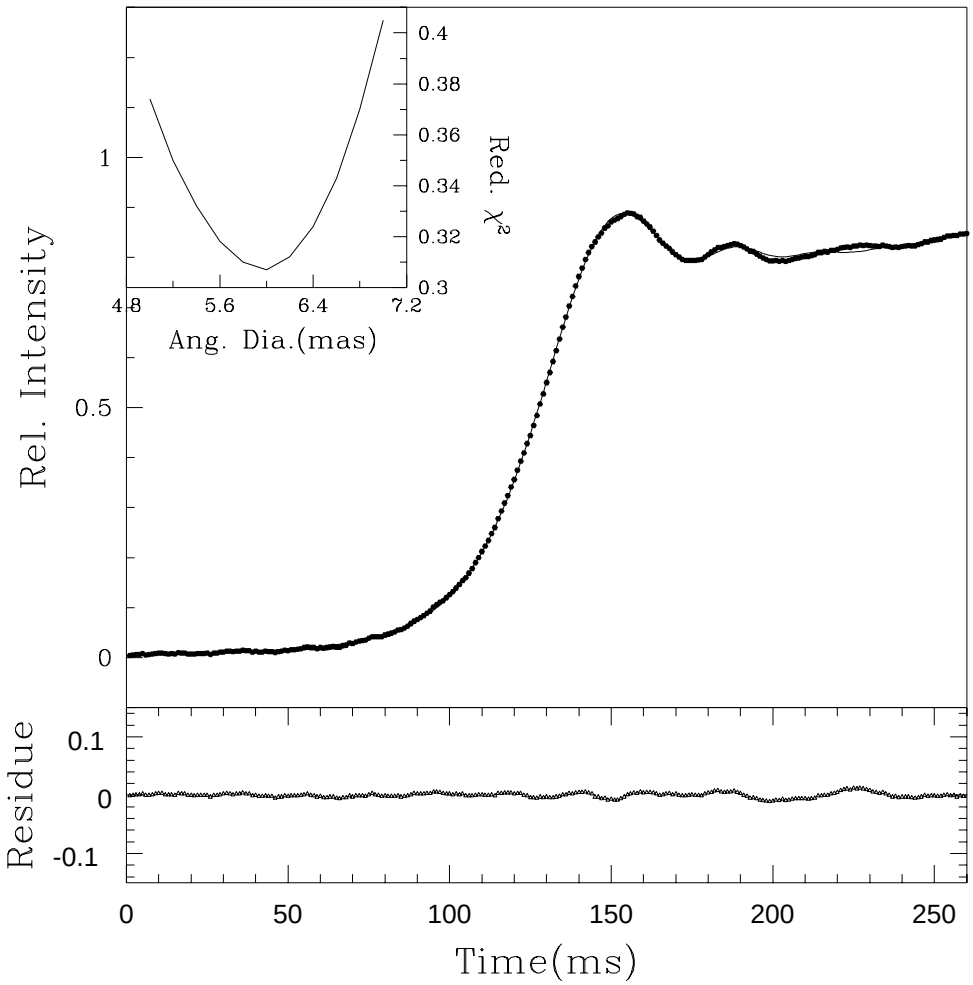

Figure 4.13: The data (dots) with the model fit to it (solid line) for IRC-10308. The inset shows the χ^2 convergence. The lower panel shows the residuals of the fit.

IRC-10308

It is an oxygen rich semiregular variable of type SRb. Noguchi (1990) classify it as M5 III. An alternate classification is of M3 by Stencel & Backman (1991). Hron et al. (1997) give an estimate of the stellar and dust temperature from black body fits to the IRAS LRS. They get a stellar temperature of 2528 K and a dust temperature of 389 K. Hashimoto (1994) from his radiative transfer stellar model gives an inner dust radius of $100R_\star$ and an outer dust radius of $316R_\star$. He derives a dust temperature of 289 K. Whereas, Volk & Kwok (1987) give a dust temperature of 728 K. The period of this variable is poorly defined. Jura & Kleinman (1992) give a period of 120 days. Journal of previous lunar occultation results for this source is given in Table 4.6. Schmidtke et al. (1986) refer to a temporal variation in the size of IRC-10308 subject to position angle variation.

Table 4.6: Journal of Previous Observations for IRC+10194 and IRC-10308

Source	Date of Observation	Wavelength of Observation	ϕ_{UD} (mas)	Reference
IRC+10194	1979	1.618 μm	4.49 $\pm$0.59	Ridgway et al. (1979)
	1977	1.640 μm	3.11 $\pm$0.51	Ridgway et al. (1979)
	1978	0.75 μm	4.00 $\pm$0.50	White (1978)
	1997	2.2 μm	4.20 $\pm$0.50	Ragland et al. (1997a)
IRC-10308	1979	1.618 μm	6.55 $\pm$0.15	Ridgway et al. (1982)
	1981	0.86 μm	6.69 $\pm$0.07	Ridgway et al. (1982)
	1981	1.618 μm	5.14 $\pm$0.39	Ridgway et al. (1982)
	1981	2.17 μm	5.49 $\pm$0.37	Ridgway et al. (1982)
	1981	1.65 μm	5.79 $\pm$0.11	Schmidtke et al. (1986)
	1981	2.17 μm	5.80 $\pm$0.2	Schmidtke et al. (1986)

For this source we have a poor quality light curve. The light curve was contaminated with 50 cycle pick up from the mains power line. This frequency component was effectively and efficiently filtered out using FFT. With a slope to account for the varying background and a 2nd order Legendre polynomial to take care of the scintillation we obtain a uniform disk value of 6$\pm$0.5 mas. The data and the model fit is shown in Fig. 4.13. Due to dominant scintillation noise in the data only a truncated portion was used for data analysis. We derive an effective temperature of 3160$\pm$154 K. From the Hipparcos parallax measurement we obtain a linear radius of 217$\pm$89 $R_{\odot}$.

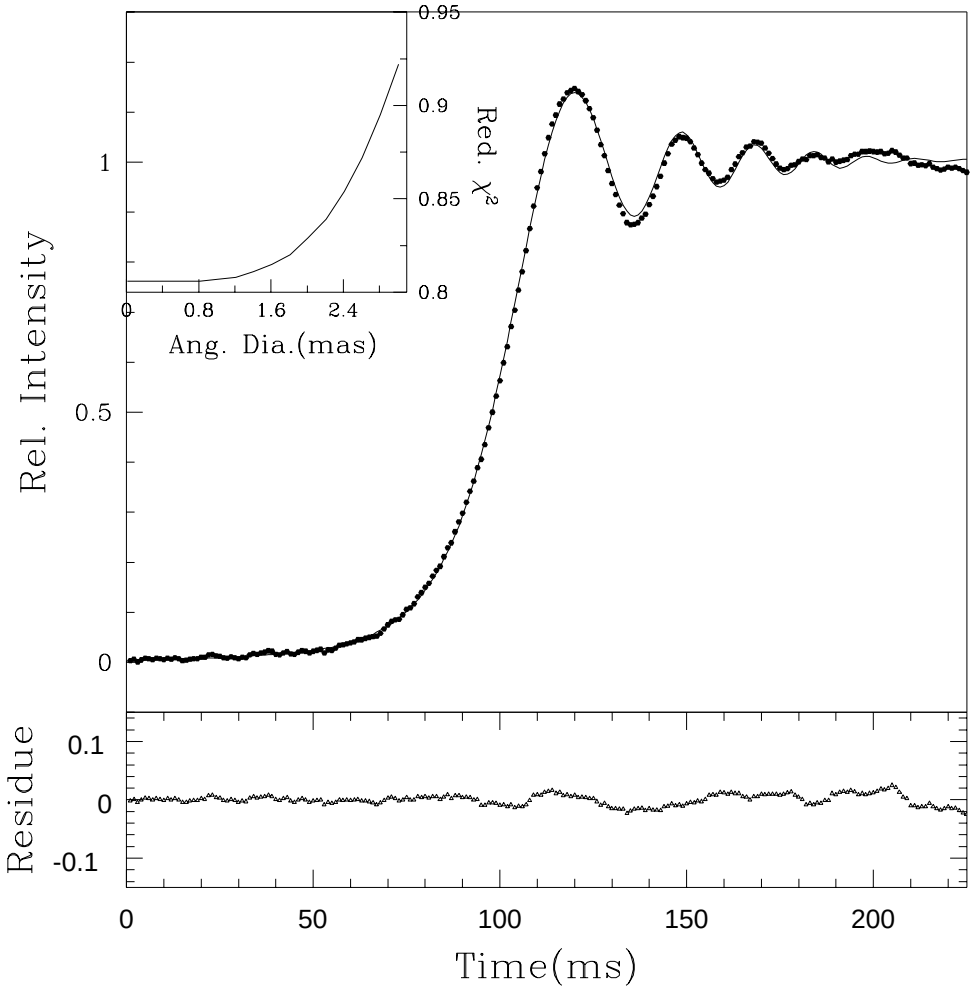

Figure 4.14: The data (dots) with the model fit to it (solid line) for IRC-10301. The inset shows the χ^2 convergence. The lower panel shows the residuals of the fit.

4.3.2 *Unresolved Sources*

IRC-10301

It is a variable of type SRb. Jura & Kleinman (1990) classify it as M5II. The other classification is of M4-M4.5 II-III given by Keenan & McNeil (1989). The IRAS LRS spectra for this source is featureless. We have recorded a good quality light curve shown in Fig. 4.14. We have estimated an upper limit of ≤ 2 mas for this source and this constitutes the first HAR observation of this source. The Hipparcos parallax to this source is 2.36$\pm$1.2 mas. Hence, an upper limit of 91 $R_{\odot}$ can be put on the linear radius of this source. We derive the spectral type between M4 – M7 for this

source from its infrared colours.

IRC+10032

It is just listed as a M type star. The data and the fit is shown in Fig. 4.15. We put an upper limit of 2 mas on the angular size of this source. This is the first HAR observation of this source. The Hipparcos parallax to this source is 1.57±1.06 mas. This puts an upper limit of 137 $R_\odot$ on the stellar linear radius. We derive a spectral

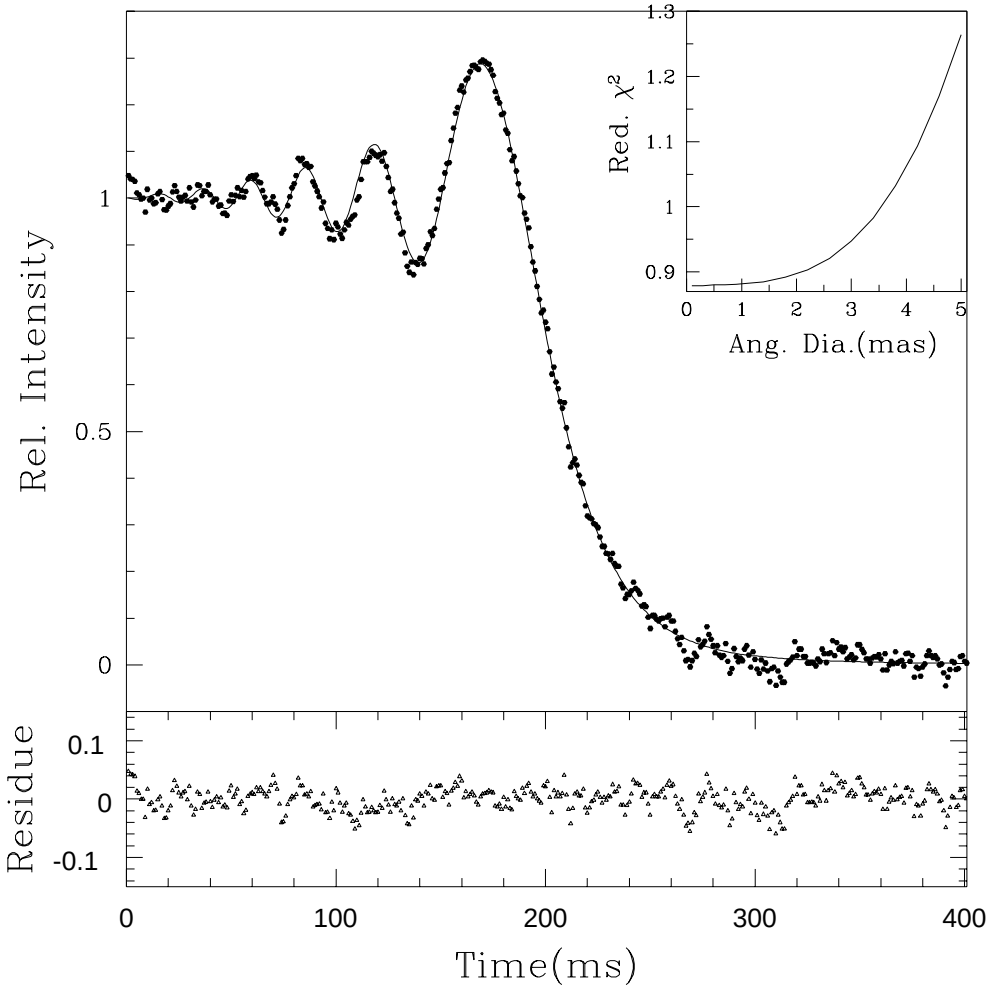

Figure 4.15: The data (dots) with the model fit to it (solid line) for IRC+10032. The inset shows the χ^2 convergence. The lower panel shows the residuals of the fit.

type between M4 – M5 for this source.

It is classified as a M7 giant (Hansen & Blanco 1973). We put an upper limit of 2 mas on this source which constitutes the first HAR observation of this source. The data and the uniform disk fit is shown in Fig. 4.16.

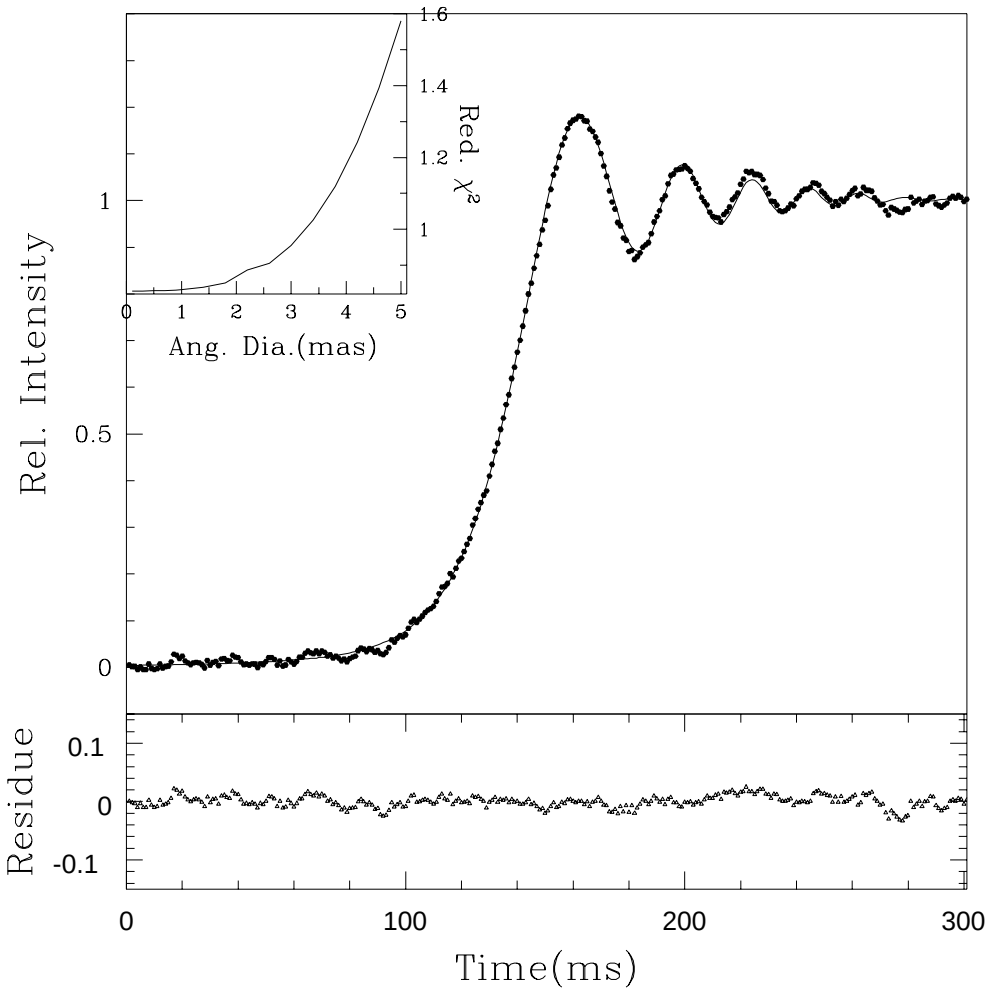

Figure 4.16: The data (dots) with the model fit to it (solid line) for IRC-20470. The inset shows the χ^2 convergence. The lower panel shows the residuals of the fit.

IRC+20125

It is classified as a M5 giant (Nassau & Blanco 1954). But the infrared colours give a range between M5 – M7. The non linear least squares fit to the data puts an upper

limit of 2 mas. A 3rd. order Legendre polynomial is used to fit the data. This is the first HAR observation of this source. The data and the fit are shown in Fig. 4.17.

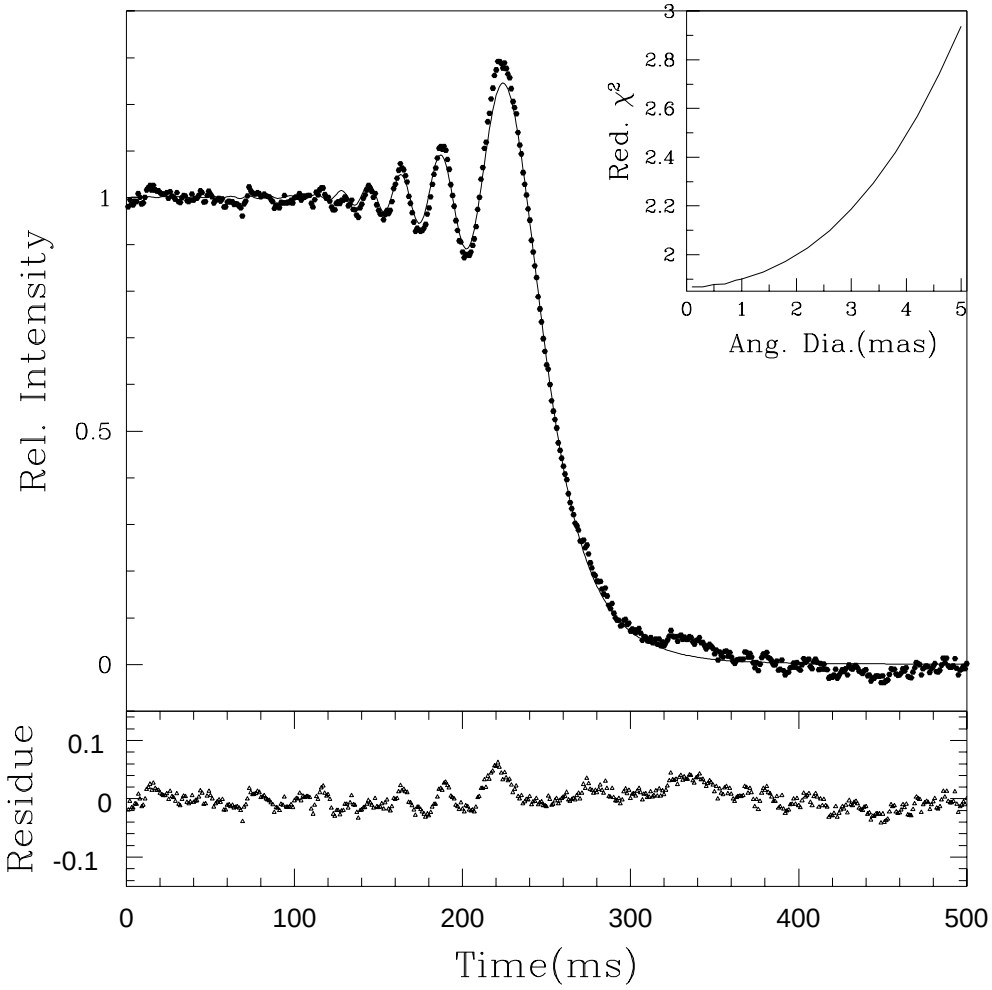

Figure 4.17: The data (dots) with the model fit to it (solid line) for IRC+20125. The inset shows the χ^2 convergence. The lower panel shows the residuals of the fit.

4.4 Discussion

4.4.1 Angular diameters for the M giant sample.

The results are consolidated in Table 4.7. We have derived the diameter values of 11 sources out of which five are new diameter measurements. The four unresolved sources in our sample have no previous diameter measurements and hence

Table 4.7: Angular diameter results on M giants

Source	ϕ_{V-K} (mas)	ϕ_{UD} (mas)	ϕ_{LD} (mas)	Remarks
IRC-10301	3.4	$\leq$ 2.0	$\leq$ 2.07	New result
IRC-10305	2.3	3.6$\pm$0.2	3.73	New result
IRC-20299	2.8	3.1$\pm$0.4	3.21	New result
IRC+10034	4.2	3.3$\pm$0.3	3.42	
IRC+10032	2.0	$\leq$2.0	$\leq$2.07	New result
IRC+10194	2.9	3.0$\pm$0.3	3.11	
IRC+20067	2.02	5.4$\pm$0.4	5.60	
IRC+20111	3.9	3.2$\pm$0.4	3.31	
IRC-10580	6.3	5.7$\pm$0.4	5.90	New result
IRC-20470	2.9	$\leq$2.0	$\leq$2.07	New result
IRC+20125	2.0	$\leq$2.0	$\leq$2.07	New result
IRC+10038	2.5	3.0$\pm$0.2	3.11	New result
IRC+20090	2.2	3.7$\pm$0.3	3.83	New result
IRC-20444	4.0	4.2$\pm$0.5	4.35	
IRC-10308	7.0	6.0$\pm$0.5	6.21	

we have put the first upper limits on the angular diameter of these sources. Even-though we do not have a statistically large sample, these results are a substantial contribution to the data base of angular diameters which can be used to strengthen stellar models and also to derive correlation between different stellar parameters.

In Table 4.7 we have also listed the estimated angular diameters derived from the visual surface brightness and the infrared colour of the sources. We have used the relation derived by Ragland (1996) based on the angular diameter data

Table 4.8: Effective Temperatures of the resolved M giants.

Source	Spectral Type (derived)	$(V-K)$	$(J-K)$	T_{eff} (K)
IRC-10305	M2.0	5.13	1.10	2883±108
IRC-20299	M7.0	6.95	1.33	3140±216
IRC+10034	M7.3	7.43	1.32	3556±186
IRC+10194	M3.1	4.93	1.17	3453±190
IRC+10038	M6.8	6.63	1.68	3098±133
IRC+20067	M7.5	6.35	1.34	2244±101
IRC+20090	M8.0	8.21	1.37	2533±123
IRC+20111	M7.5	7.05	1.31	3318±222
IRC-10580	M7.5	8.05	1.37	3088±134
IRC-20444	M9.0	10.31	2.0	2788±215
IRC-10308	M7.0	6.95	1.29	3160±154

and visual magnitudes cataloged in White & Feierman (1981) and infrared magnitudes from Gezari et al. (1993). However, these estimates have large errors (20-50%).

4.4.2 The T_{eff} Scale

The effective temperatures calculated are shown in Table 4.8 We have also listed in this table the spectral types derived from infrared colours. Fig. 4.18 shows the effective temperature as a function of the spectral type. As is clearly evident the sample is not large enough to give any meaningful temperature scale. Moreover, there is a clustering around M7 – M8. To compare our results with the ones existing in literature we plot all the data points available for M giants from literature alongwith our points in Fig 4.19. We see that our results fall in place with the given scatter except for the two sources IRC+20067 and IRC+20090. Also plotted are the

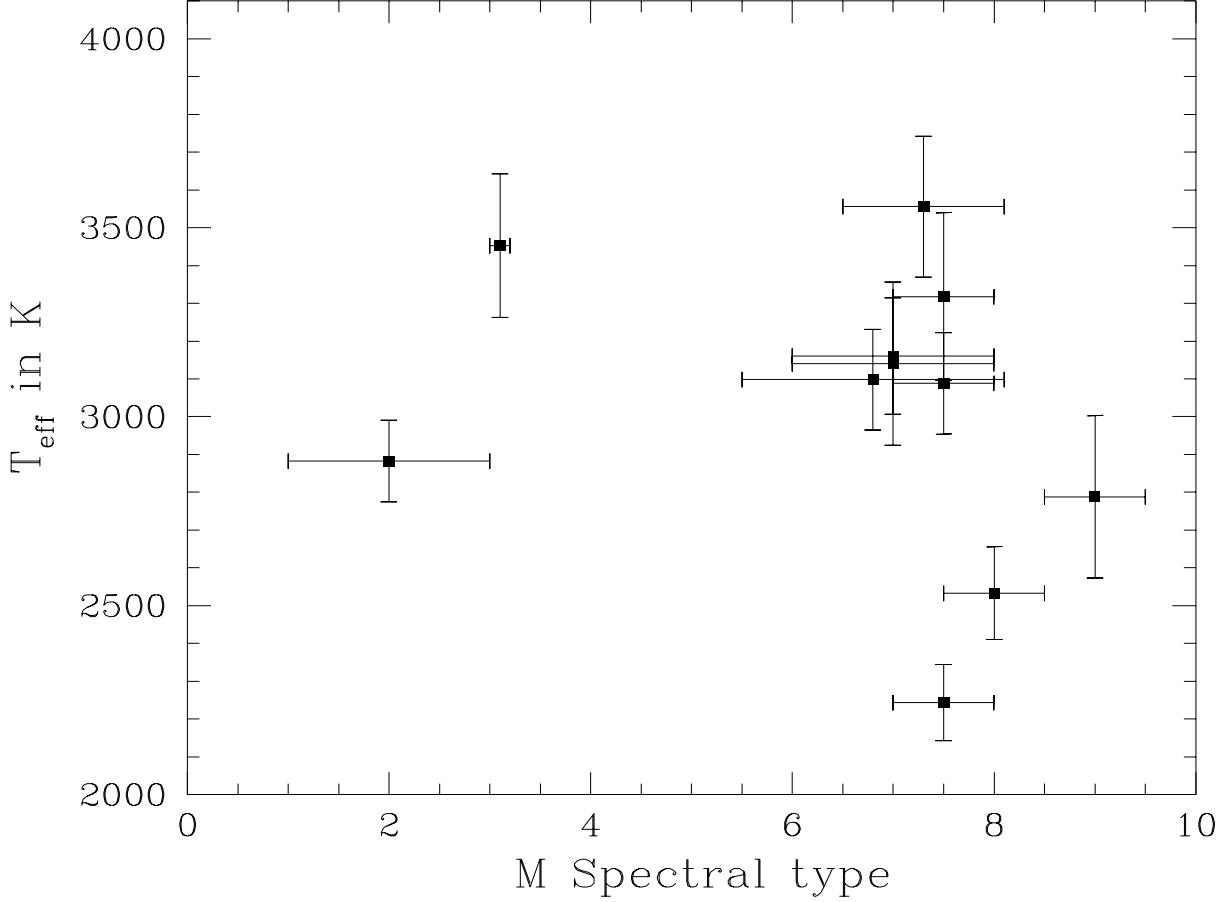

Figure 4.18: Spectral type versus the derived effective temperature of our sample of M giants. The x axis error bars show the uncertainty in the spectral type.

fits obtained by each group. Looking at the scatter in the data points, we wish to suggest that a single calibration curve, be it a linear regression fit or a cubic spline does not seem to adequately represent the measurements. Looking at the scatter in the points a band seems to be more suitable.

4.4.3 Linear Radii.

The linear radii derived for the sources having Hipparcos parallax measurements are listed in Table 4.9. For the two unresolved sources we have put upper limits. It is apparent from the values derived by van Belle et al. (1999) and Dumm & Schild (1998) that there is large scatter in the linear radii for a particular spectral class for M type giants. Our derived values are consistent with these estimations within the given scatter.

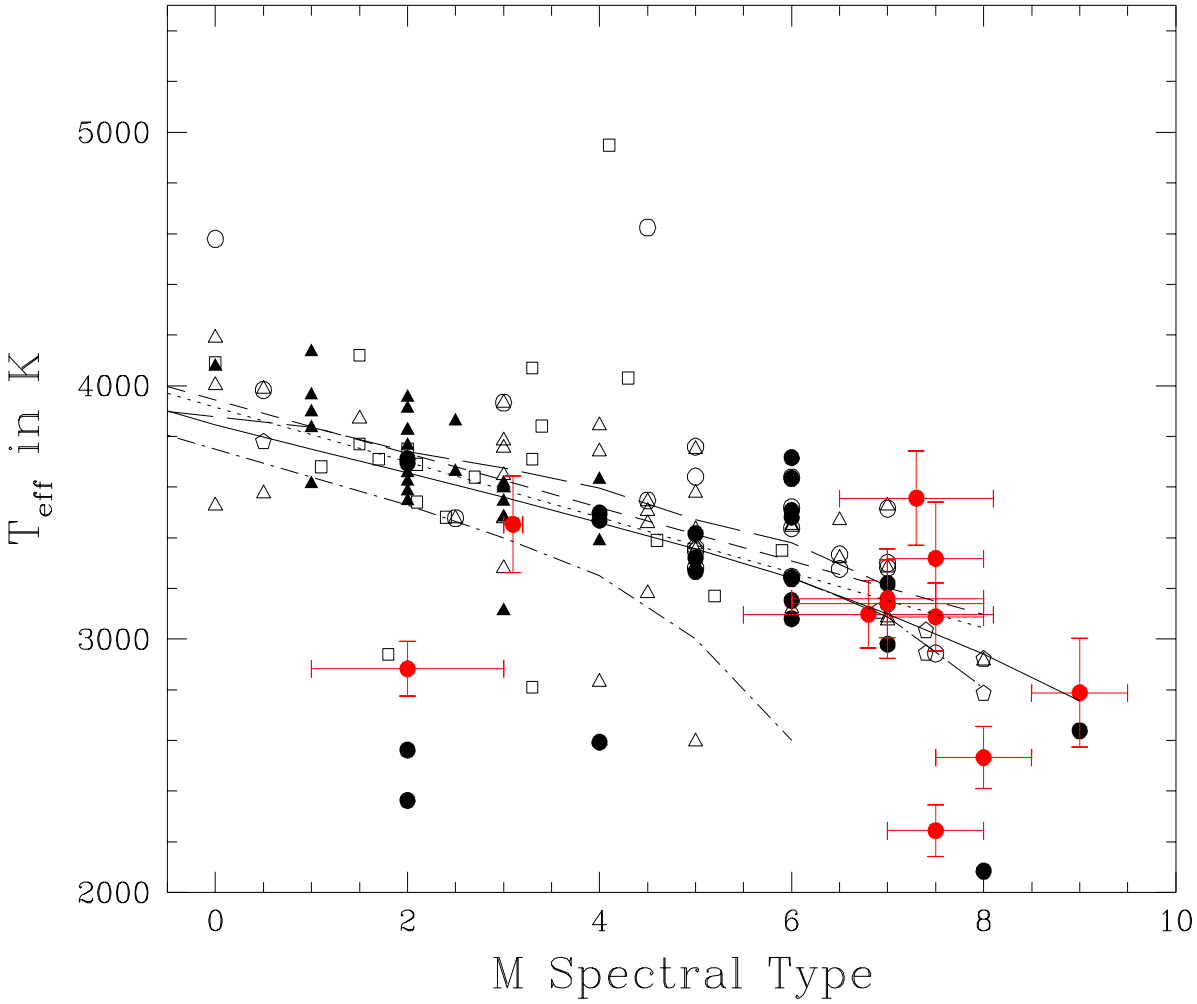

Figure 4.19: This figure compares our data points with all other effective temperature derivations from literature. The red circles are our points. The other data sets are: Ridgway et al. (1980)(open squares); Dyck et al. (1998)(open triangles); Dyck et al. (1996)(open circles); Perrin et al. (1998)(open pentagon); Richichi et al. (1999)(Closed circles); van Belle et al. (1999)(closed triangles). This figure also shows the fits obtained by these different groups. They are Richichi et al. (1999) (solid line); van Belle et al. (1999)(dotted line); Dyck et al. (1998)(short dash); Dyck et al. (1996)(long dash); Ridgway et al. (1980)(dot-short dash) and Perrin et al. (1998)(dot-long dash).

Table 4.9: Derived linear radii for giants having Hipparcos parallax.

Source	Distance(pc)	Linear radii ($R_{\odot}$)
IRC-10301	424±215	$\leq$ 91
IRC-10305	459±206	178±80
IRC+10032	637±430	$\leq$ 137
IRC+10194	446±215	144±71
IRC-10580	285±102	175±64
IRC-10308	337±135	217±89

4.5 Remarks

We have added to the growing list of M giants which have well determined angular diameters. As many of the later M types are variable sources, multiple HAR observations of each of these sources are required before one can derive its effective temperature scale meaningfully. Infrared long baseline interferometric measurements in the coming years are likely to yield a large sample of accurate diameters which can then be compared with the large data base of infrared lunar occultation studies.

Chapter 5

Other Sources

In this chapter we present the results of 8 sources of spectral type earlier than M and of various luminosity classes. The cross identifications of these sources are given in Table 5.1 and the journal of observations and source details are listed in Table 5.2. Table 5.3 gives the predicted circumstances of the events.

Table 5.1: Cross identification of sources.

Serial No.	TMSS	SAO	IRAS	HD	BS	Other Names
1.	IRC-20271	158840	14481-1550	130841	5531	Alf 2 Lib
2.	IRC-20502	-	18341-1915	171736	-	-
3.	IRC-20325	160046	16386-1738	150416	6196	-
4.	IRC-20362	-	17245-1855	-	-	-
5.	IRC+20191	97399	07541+1555	64960	3095	1 Cnc
6.	IRC+20076	93897	04200+1725	27697	1373	Del Tau
7.	IRC-10300	158427	14102-1002	124294	5315	Kap Vir
9.	-	94345	05058+1947	33121	-	107 Tau

Table 5.2: Journal of observations and source details.

Source Name	Date of Observation	Event Type	Spectral Type	V	K	Hipparcos Parallax (mas)
IRC-20271	1995 Jun 10	D	A3IV	2.75	2.41	42.25±1.05
IRC-20502	1995 May 17	D	G8Ib	7.10	2.92	2.60±1.15
IRC-20325	1997 Feb 02	R	G7.5III	4.96	2.35	8.34±0.85
			G7.5II-III			
			G8II			
IRC-20362	1997 May 23	R	-	-	2.83	-
IRC+20191	1996 Dec 26	R	K3III	5.78	2.89	7.06±0.90
	1997 Mar 18	D				
IRC+20076	1996 Mar 24	D	K0III	3.78	1.60	21.29±0.93
			K0IIICN.5			
			A2IV			
IRC-10300	1997 Jun 16	D	K3III	4.30	1.19	14.59±0.95
			K2.5III Fe-0.5			
SAO 94345	1995 Jan 13	D	G5III	6.50		5.94±0.87

Table 5.3: Predicted circumstances of the events.

Source	Time (UT) (hh mm ss)	Alt. of star (deg)	PA[1] (deg)	CA[2] (deg)	Vel. comp. (km/s)
IRC-20271	17 15 21	48.7	84.31	-23.24	0.6203
IRC-20502	20 33 17	40.7	256.53	171.24	0.6836
IRC-20325	24 03 31	30.1	286.93	182.37	0.7572
IRC-20362	23 49 06	24.8	230.97	144.60	0.6257
IRC+20191(R)	22 30 42	63.3	258.47	149.70	0.5370
IRC+20191(D)	16 08 14	75.8	109.61	3.10	0.5203
IRC+20076	15 23 23	33.7	26.05	-64.48	0.3342
IRC-10300	15 43 52	55.1	62.6	-53.61	0.3576
SAO 94345	16 40 27	85.0	95.31	7.49	0.5476

1. Position Angle 2.Contact Angle.

5.1 Results

5.1.1 Angular diameter

We discuss the individual sources below giving a brief source history of each.

IRC-20271

This source is classified as a A3IV star. It is a $JHKLM$ standard star (Bouchet et al. 1991) and a secondary standard for $BVRI$ photometry (Moffett & Barnes 1979). In a search for circumstellar dust around main sequence A stars within 25 pc of the sun, IRC-20271 was found not to be dusty (Cheng et al. 1992). This was done using IRAS data. Using the Infrared Flux Method (IRFM) described in Blackwell et al. (1979), Shallis et al. (1985) give an estimate of the linear radii of the star as $R/R_{\odot}=1.8\pm0.31$, whereas, Babu & Shaylaja (1981) give a value of $R/R_{\odot}=2.0$.

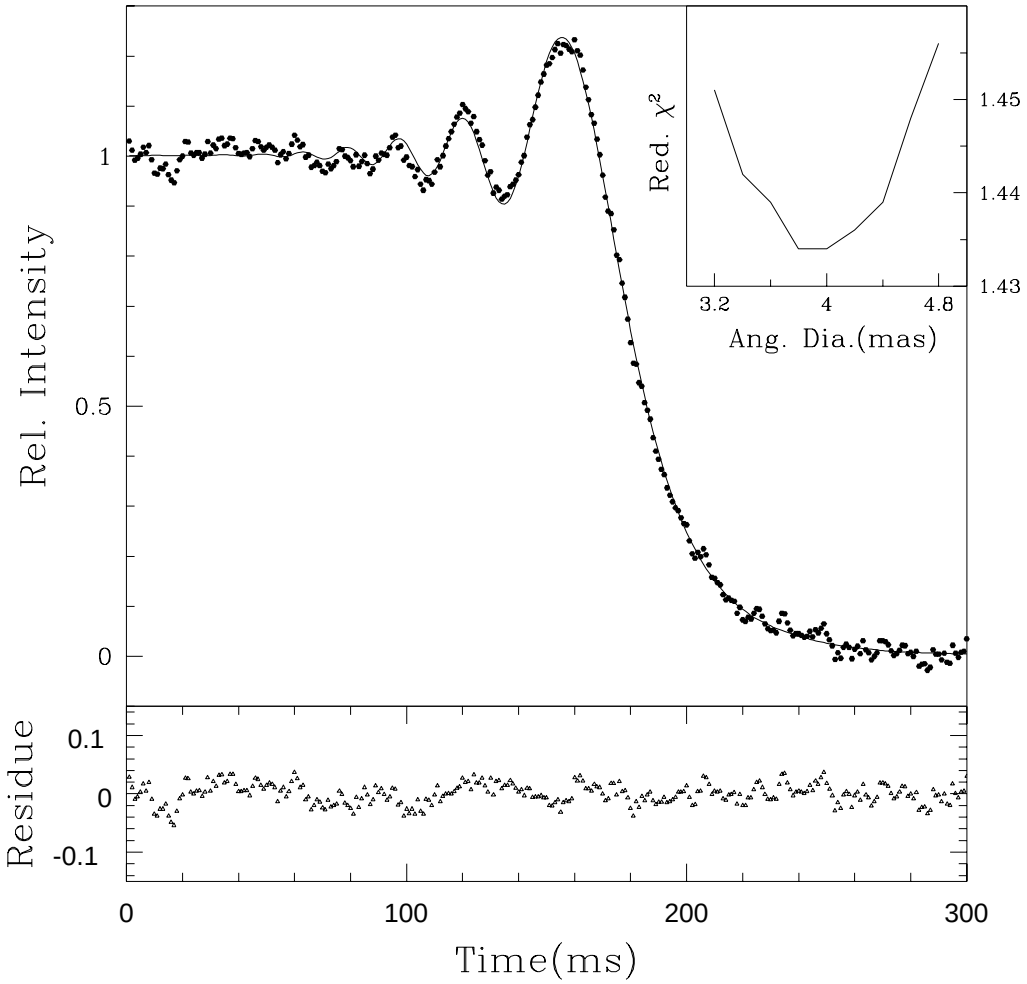

Figure 5.1: The data (dots) with the model fit to it (solid line) for IRC-20271. The lower panel shows the residuals of the fit. The inset shows the χ^2 convergence.

Shallis & Blackwell (1979) estimate a mean angular diameter of 0.953 mas for this source. We have a good quality occultation light curve for this source. Fig. 5.1 shows the data with the model fit to it. We derive a uniform disk angular diameter value of 4.0±0.4 mas and we estimate an effective temperature of 5200±368 K. This is inconsistent with the black body temperature of 8100 K fitted to the spectral energy distribution of the source and also inconsistent with the spectral type. We are getting a large diameter than expected from the spectral type and bolometric flux of this source. An earlier occultation of this source was recorded in the *B* band at KPNO on 31 May 1966 using the 36 inch reflector (Poss 1971). The light curve showed the presence of a close binary (projected separation of 10 mas) with $\Delta m = 0.4$. Although we do not detect any close binaries beyond the noise in our

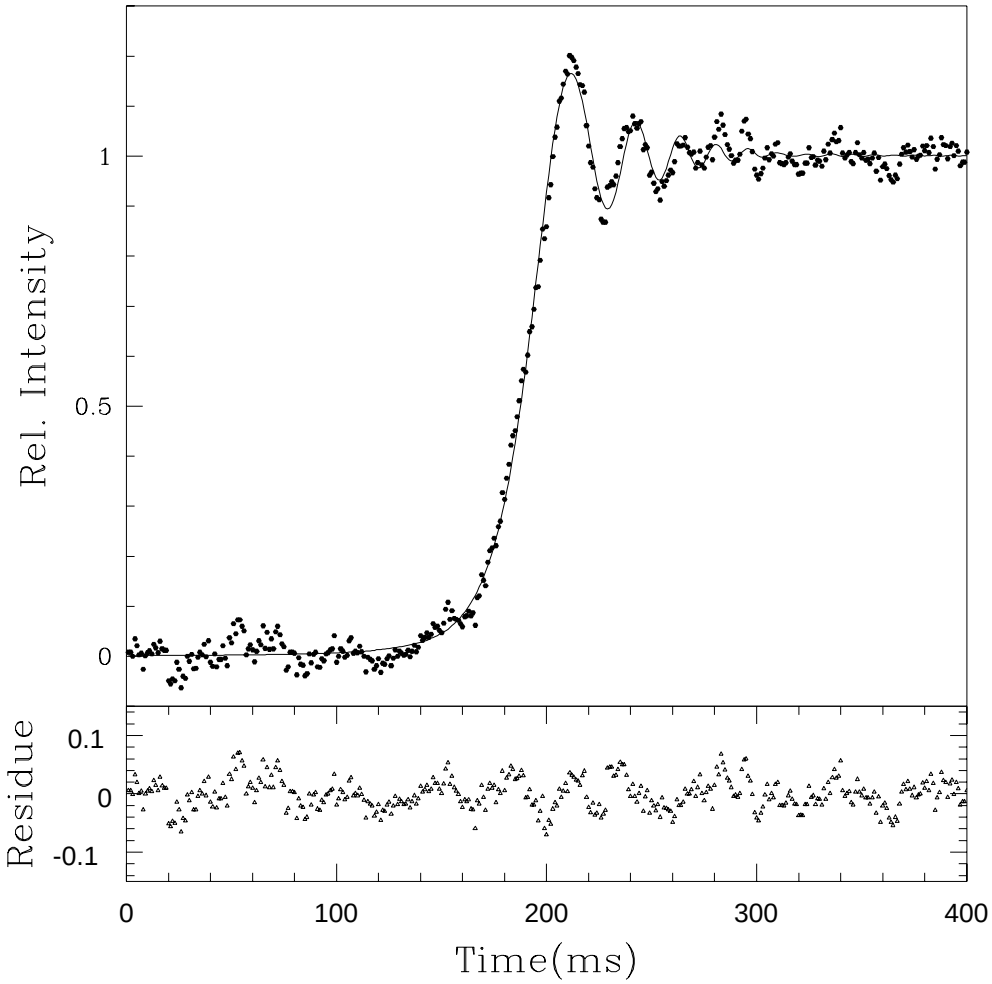

Figure 5.2: The data (dots) with the model fit to it (solid line) for IRC-20502. The lower panel shows the residuals of the fit.

data, but the presence of one would mimic a large angular diameter. From the Hipparcos parallax measurement we derive a linear radii of 10.3 $\pm$1.1 $R_{\odot}$ for IRC-20271.

IRC-20502

It is classified as G8Ib. No other information is available on this source. From the analysis of our occultation light curve we put an upper limit of 2 mas on the angular size of the source. The data and the least squares fit to it is shown in Fig. 5.2

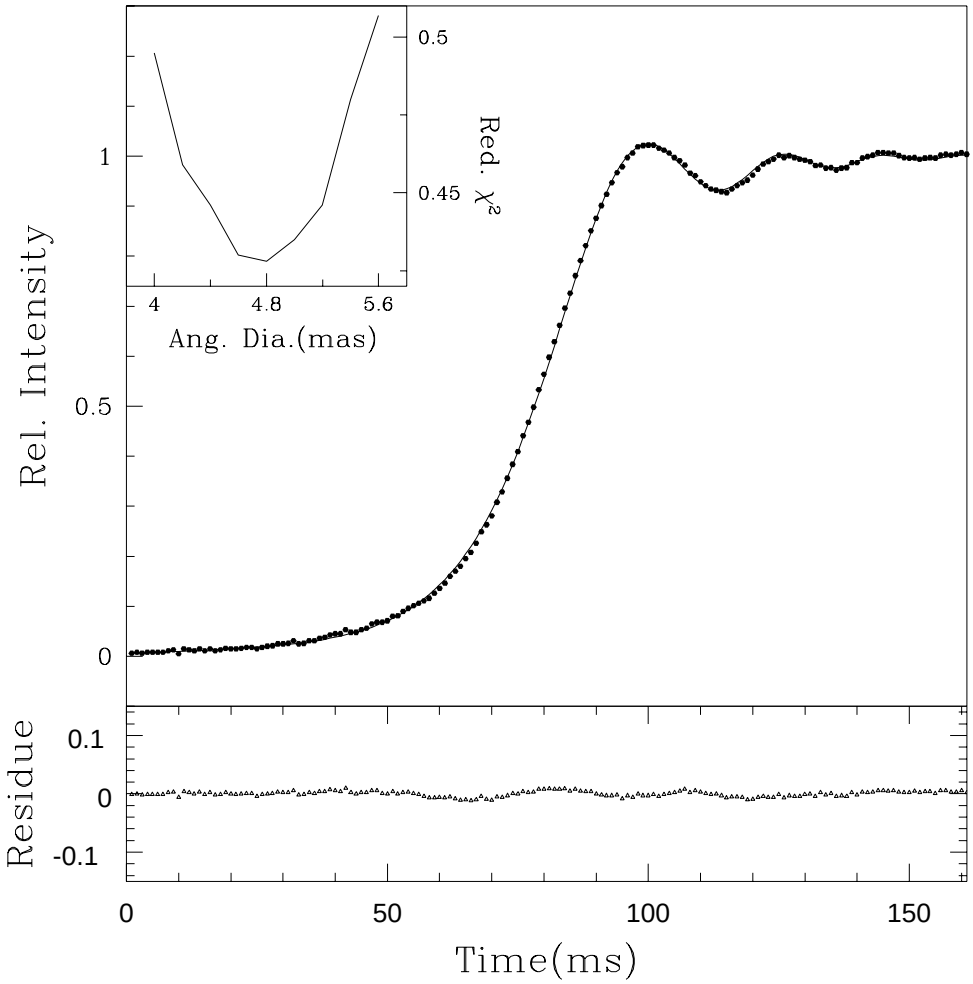

Figure 5.3: The data (dots) with the model fit to it (solid line) for IRC-20325. The lower panel shows the residuals of the fit. The inset shows the χ^2 convergence.

IRC-20325

It is a barium star classified as G7.5 II CN1 Ba0.4 by Keenan & Pitts (1980). The other classifications of this source available in literature are listed in Table 5.2. There seems to be a large distance discrepancy for this source. Jones et al. (1992) list a distance of 21.3 pc for this source but the recent results from the Hipparcos mission gives a distance of 120 pc. From the available photometry and colour-temperature relations, Brown et al. (1989) give a temperature estimate of 4900 K for IRC-20325 which they comment as uncertain. Sporadic radio emission at 8.4 GHz was detected from this source (Slee et al. 1989).

The light curve of this source has a dip just after the event due to less than

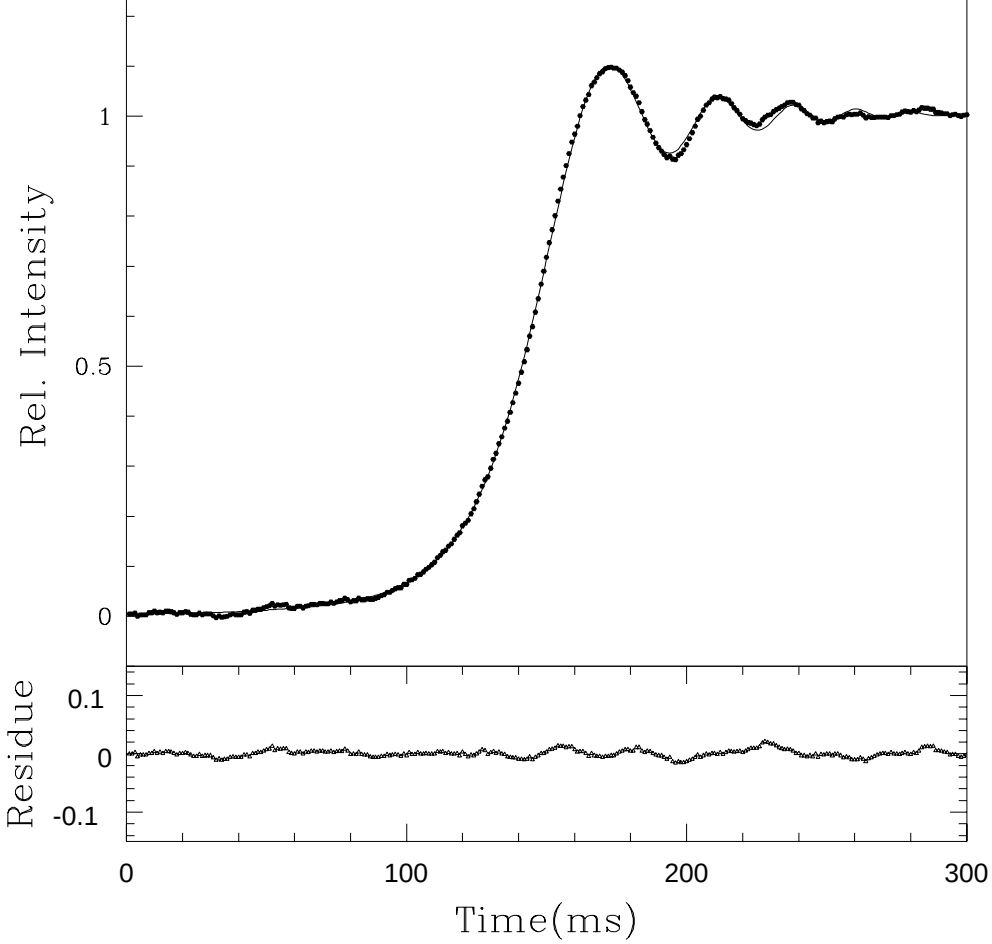

Figure 5.4: The data (dots) with the model fit to it (solid line) for the reappearance event of IRC+20191. The lower panel shows the residuals of the fit.

optimal sky condition during observation. Hence, a truncated portion is used for data analysis. Using data of a larger length to accomodate the dip and then giving low weightage to that portion also yields consistent results. We derive a uniform disk value of 4.8$\pm$0.2 mas. The light curve with the model fit is shown in Fig. 5.3. We derive an effective temperature of 3595$\pm$195 K for this source. The black body temperature which fits the spectral energy distribution of this source is 4100 K. From the Hipparcos distance estimate we derive a linear radii of 62$\pm$6.7 $R_{\odot}$ for IRC-20325.

IRC+20191

IRC-20191 is classified as spectral type K3III. The most recent work by Keenan & Barnbaum (1999) on the revision of the MK luminosity classes for cool giants using

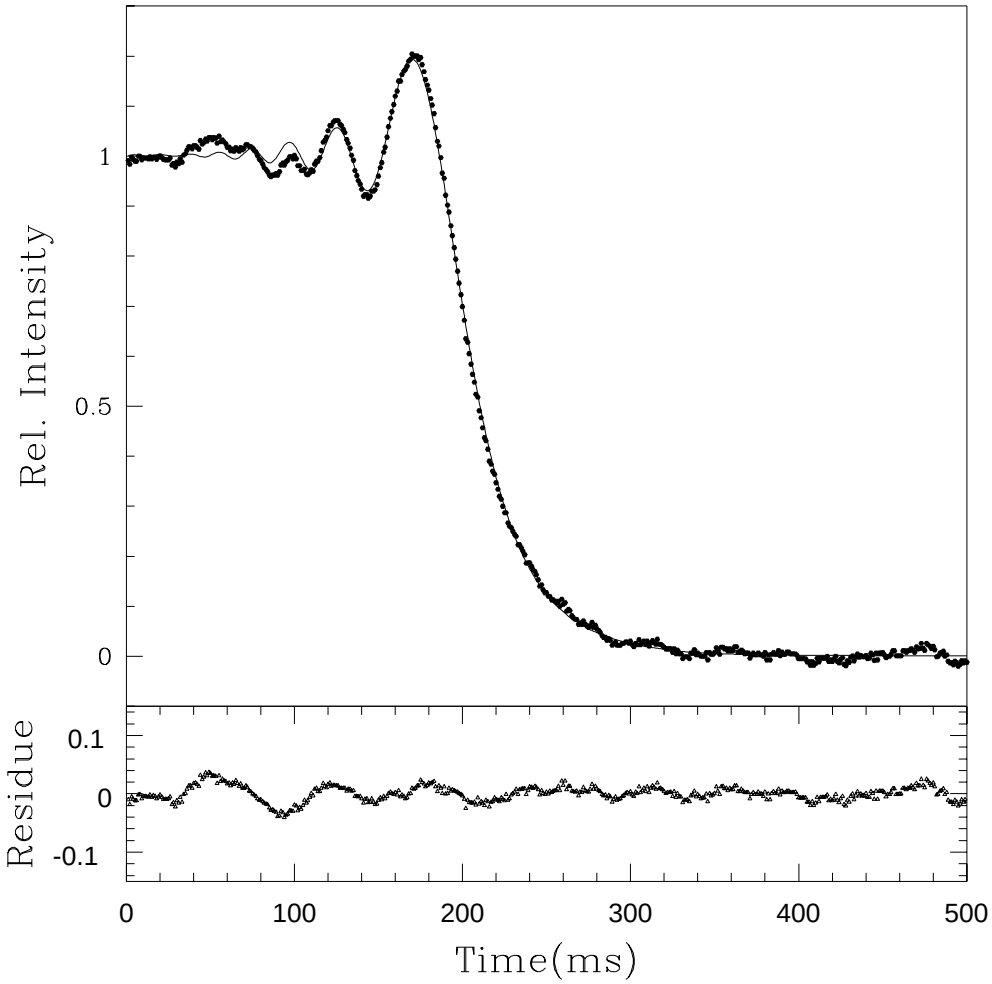

Figure 5.5: The data (dots) with the model fit to it (solid line) for the disappearance event of IRC+20191. The lower panel shows the residuals of the fit.

Hipparcos parallaxes give the spectral classification as K3-III. A previous lunar occultation of this source by de Vegt (1976) give a uniform disk value of 2.1±0.6 mas at 0.6 μm.

We have two occultation events of this source. The light curve of the disappearance is affected by fluctuations due to passing clouds. From both the events we derive an upper limit of 2 mas for this source which is consistent with previous estimation. Both the light curves and the uniform disk model fit to them are shown in Fig. 5.4 and Fig. 5.5 respectively.

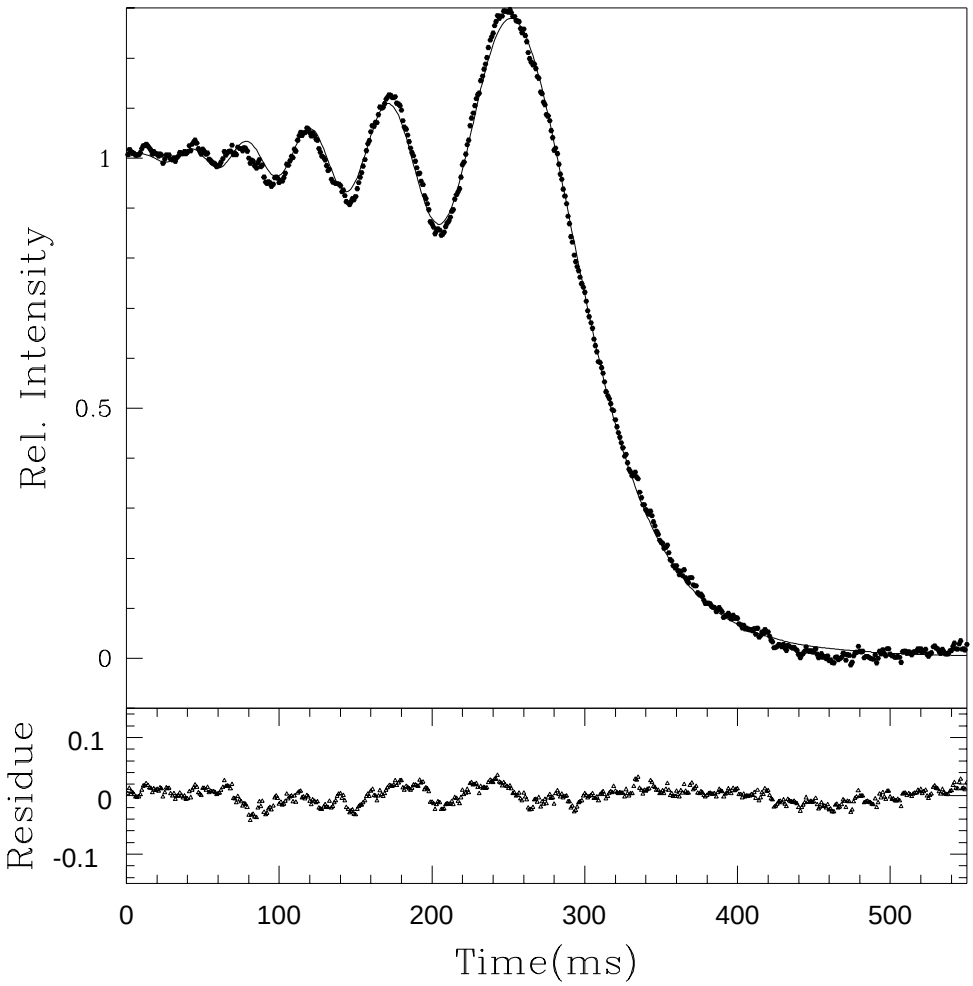

Figure 5.6: The data (dots) with the model fit to it (solid line) for IRC+20076. The lower panel shows the residuals of the fit.

IRC+20076

This single lined spectroscopic binary is classified as K0III. The other classifications are listed in Table 5.2. There seems to be a discrepancy in the classification. Barstow et al. (1994) in their IUE survey for hot DA white dwarfs in non-interacting binary systems have listed this source as A2IV and have used it as a comparison. This could be the hot companion of the K giant. Boffin et al. (1993) give a spectral classifiaction of K0III CN.5 for this source. They list it as a spectroscopic binary with a period of 529.8 days.

In a recent work by Cohen et al. (1999) on spectral irradiance calibration in the infrared, IRC+20076 has been classified as a G9.5 giant and a diameter estimate

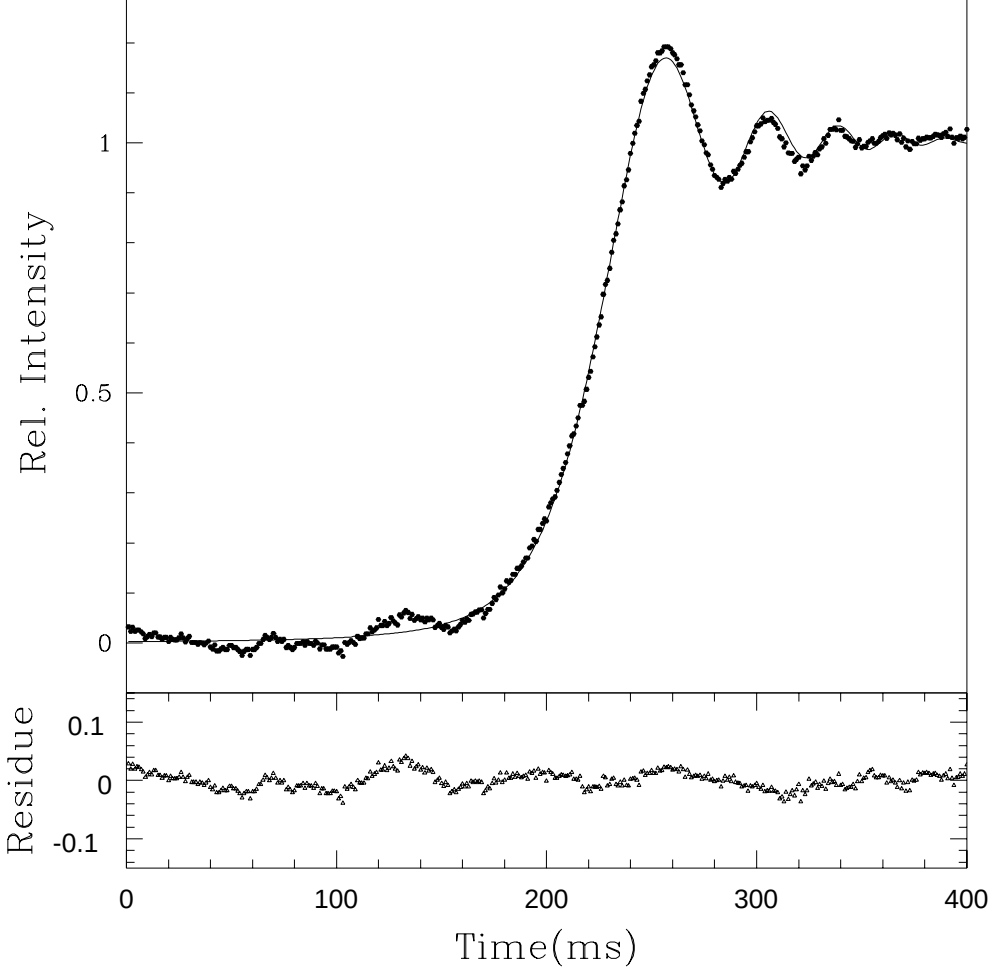

Figure 5.7: The data (dots) with the model fit to it (solid line) for IRC-20362. The lower panel shows the residuals of the fit.

of 2.28±0.024 mas is given for this source. Using the IRFM with the improved Kurucz model atmospheres, Blackwell & Lynas-Gray (1994) give a temperature of 4938 K and a angular size of 2.262 mas for IRC+20076. Halbwachs (1981), from theoretical calculations, estimate the binary separation to be 60 mas.

We have recorded a good S/N ratio light curve for this source. Detailed data analysis put an upper limit of 2 mas on the angular size. This value is conistent with previous estimates. Fig. 5.6 shows the data and the model fit.

IRC-20362

This source is only listed in the TMSS catalogue. No spectral type or luminosity information is available for this source. From our JHK photometry and the infrared colours given by Perrin et al. (1998) we derive a classification of M8 III or

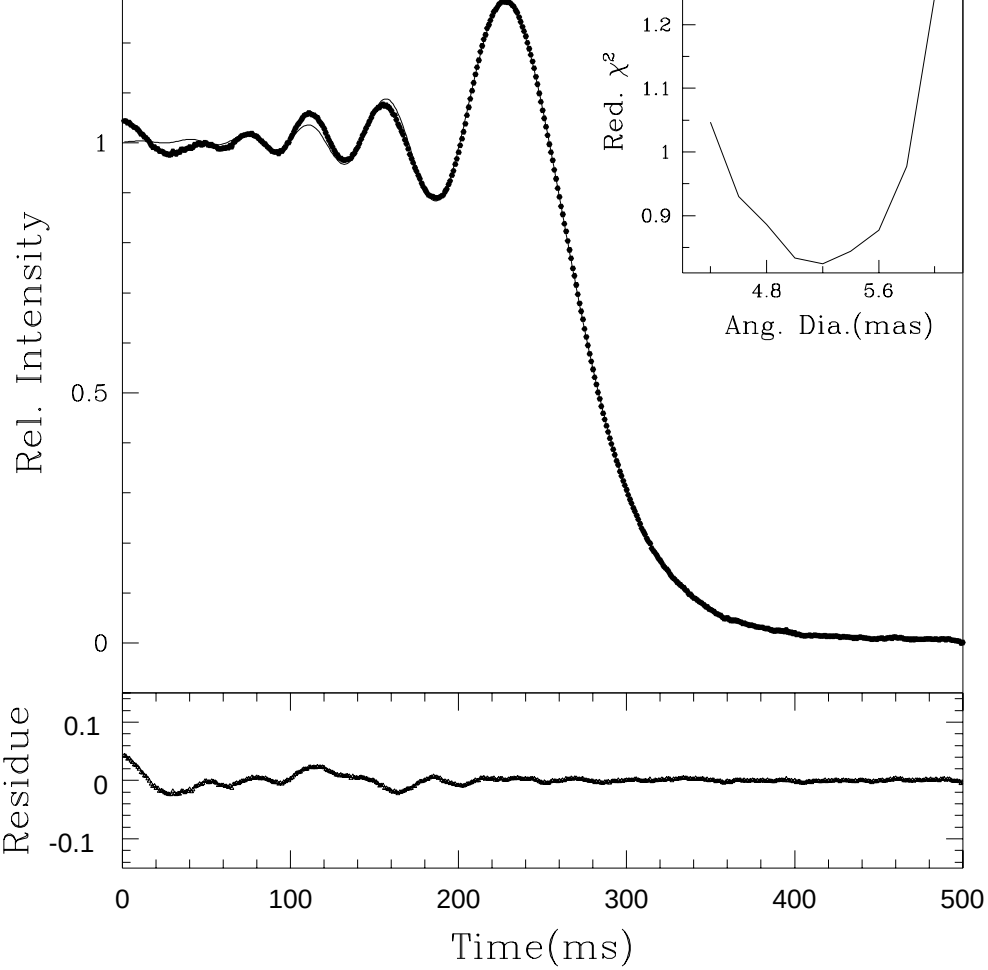

Figure 5.8: The data (dots) with the model fit to it (solid line) for IRC-10300. The lower panel shows the residuals of the fit. The inset shows the χ^2 convergence.

later for this source. Photometric and spectroscopic monitoring of this source will be interesting.

We derive a angular size value of $\leq$ 2 mas for this source. The data and the model fit are shown in Fig. 5.7

IRC-10300

κ Vir is classified as K2.5III Fe-0.5 by Keenan & McNeil (1989). This source is listed as a southern $JHKL$ standard in Carter (1990). In Cohen et al. (1999) on the calibration of spectral irradiance this is listed as K2.5III and a diameter estimate of 3.31$\pm$0.033 mas is estimated. Whitford (1946) had observed the lunar occultation of this source through clear filter and gave an angular size of 5 mas with an error of 10%.

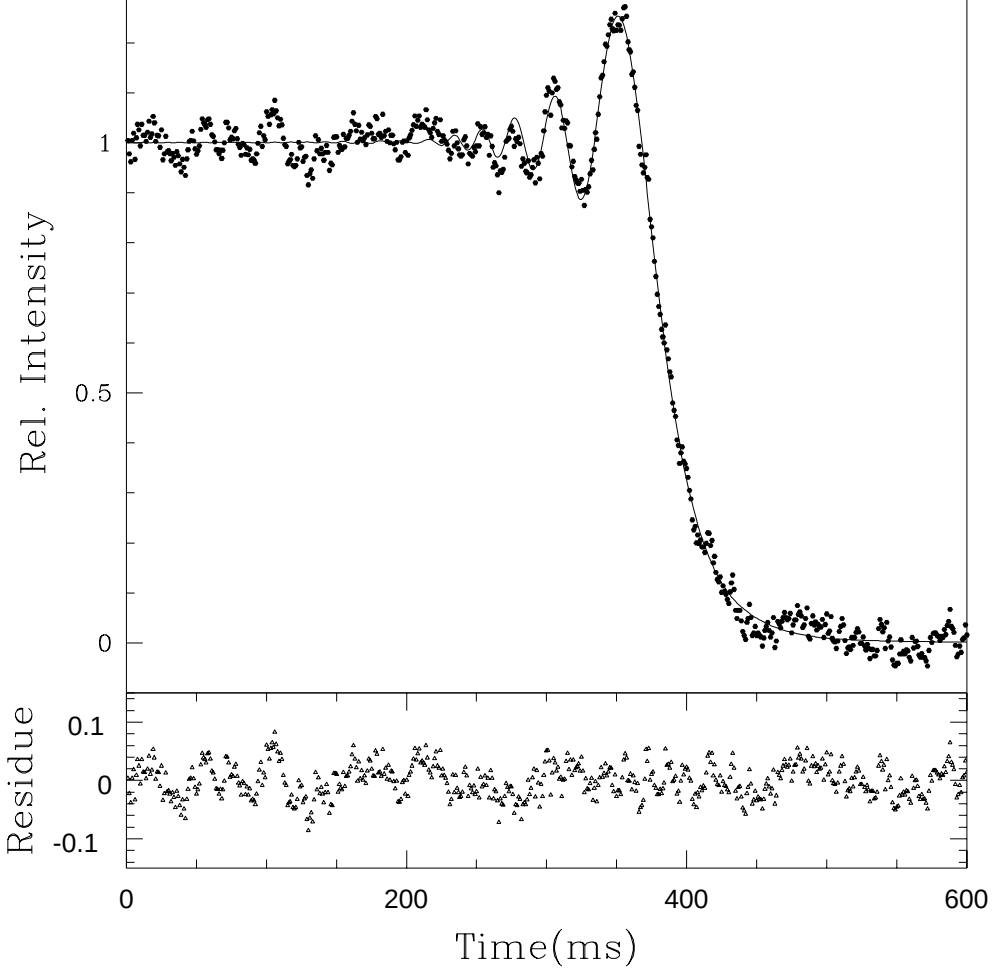

Figure 5.9: The data (dots) with the model fit to it (solid line) for SAO 94345. The lower panel shows the residuals of the fit.

We have observed the lunar occultation of this source through passing clouds. The dominant noise in the light curve is due to the fluctuations seen in the signal level because of the clouds. We have derived an angular diameter of 5.2±0.5 mas for this source. Fig. 5.8 shows the data and the uniform disk model fit to it. The effective temperature derived for this source is 3350±232 K. This is consistent with the black body temperature of 3650 fitted to the spectral energy distribution of IRC-10300. The derived linear radii is 39±4.5 $R_{\odot}$.

SAO 94345

This source is classified as G5III (Harlan 1969). Two previous occultation of this source has been observed (Blow et al. 1982; Eitter & Beavers 1979) but no angular diameter estimate is available. We put an upper limit of 2 mas on the angular size

Table 5.4: The derived angular diameters

Source	Angular diameter (mas)
IRC-20271	4.0±0.4
IRC-20502	≤2
IRC-20325	4.8±0.2
IRC+20191	≤2
IRC+20076	≤2
IRC-20362	≤2
IRC-10300	5.2±0.5
SAO 94345	≤2

from our data. Fig. 5.9 show the data and the model fit.

The angular diameters obtained are consolidated in Table 5.4. We give the first angular diameter determinations of IRC-20271 and IRC-20325. We also give the first upper limits for three sources namely IRC-20502, IRC-20362 and SAO 94345.

5.1.2 JHK photometry, derived effective temperatures and linear radii.

We have carried out JHK photometry of 4 of the sources in our sample. Two others namely IRC-20271 and IRC-10300 are standard $JHKLM$ stars and hence the values are used from Bouchet et al. (1991) and Carter (1990) respectively. For SAO 94345 and IRC-20502 accurate photometry could not be obtained. The derived photometric magnitudes are listed in Table 5.5.

For the resolved sources in our sample the bolometric fluxes were calculated using our photometry values supplemented with available photometry from literature. The derived effective temperatures are listed in Table 5.6. Using the

Table 5.5: JHK magnitudes.

Source	JD	J	H	K
IRC-20325	2450917.5	3.02±0.02	2.49±0.02	2.35±0.02
IRC-20362	2450918.5	4.35±0.02	3.19±0.02	2.83±0.02
IRC+20076	2450482.5	2.15±0.03	1.67±0.02	1.57±0.02
IRC+20191	2450473.5	3.76±0.03	3.04±0.03	2.90±0.03

Table 5.6: Effective temperatures.

Source	Effective Temp. (K)
IRC-20271	5200±368
IRC-20325	3595±195
IRC-10300	3350±232

Table 5.7: Derived linear radii.

Source	Distance(pc)	Linear radii ($R_\odot$)
IRC-20271	24±0.60	10.3±1
IRC-20502	385±170	≤83
IRC-20325	120±12	62±6.7
IRC+20191	142±18	≤31
IRC+20076	47±2	≤10
IRC-10300	69±4.5	39±4.5
SAO 94345	168±25	≤36

Hipparcos parallax measurements we have calculated the linear radii for our sample. Table 5.7 gives the Hipparcos distances and the calculated linear radii. This also lists the distances.

5.2 Remarks

In this chapter we have discussed the results obtained for a heterogeneous sample of eight stars. This includes the first HAR measurements of five sources, out of which two are resolved sources. For the rest we have given upper limits of 2 mas.

Chapter 6

Summary of the thesis and scope for future work

6.1 Summary

The aims of this thesis are :

- To accurately determine the angular diameter of a sample of bright infrared sources from the TMSS catalogue by using the technique of lunar occultation in the K band and to derive their effective temperatures.
- To study the phase and wavelength dependent angular size variations of Mira type variable R Leonis in the near infrared and determine its mode of pulsation. To determine the angular diameter of a suspected Mira variable IRC-20563 at two epochs in the K band and investigate the possibility of a size variation.
- To obtain the effective temperatures of a sample of M giants and compare the values with the existing calibrations of the effective temperature scale.

Towards achieving the above mentioned goals a rigorous attempt was made to successfully observe a large number of favourable lunar occultation events from the 1.2m telescope at Gurushikar. Instrumentation of an angular chopper was designed and developed to yield accurate JHK photometry required for the determination of the bolometric fluxes to derive the effective temperatures. Extensive

laboratory testing of the detector system was done to study the nature and shape of the time response curve under different settings of the dewar. This information was used in the data analysis procedure.

Detailed analysis of the recorded light curves were done using the non-linear least squares fitting procedure. An alternate approach of analysis involving an observed point source occultation light curve was also formulated and used as a cross check on the main mode of analysis especially while looking for angular size variations at the sub-milliarc second level.

The sample considered for this thesis comprises of 25 stars. The bar chart of the spectral types covered in our sample is given in Fig. 6.1. Of the 25 stars in our sample 16 have been resolved. From a careful analysis of the unresolved sources, the instrumental resolution limit was determined to be 2 mas. In this thesis, angular diameters for 7 sources and upper limits for 7 of the 9 unresolved sources have been given for the first time. The bar chart giving the distribution of resolved angular diameters in our sample is shown in Fig. 6.2. The percentage errors in the determination of angular diameters which crucially depend on the S/N ratio in the observed occultation light curves range from 4 – 13 %. The distribution is shown in Fig. 6.3.

Mira variables are interestingly poised in an epoch of stellar evolution which can throw light on various vistas of stellar astrophysics. The angular diameter measurements of R Leonis at 3.36 μm and 2.2 μm at the visual variability phases of 0.17 and 0.44 respectively, have enabled a study of the phase-dependent and wavelength-dependent variation of its angular size. Large phase coherent variations of this source reported in the optical region are not seen in the infrared. Linear radii values of 478$\pm$50 $R_\odot$ and 441$\pm$50 $R_\odot$) derived for the two epochs of observations preclude the fundamental mode and constrain the mode of pulsation to the first overtone.

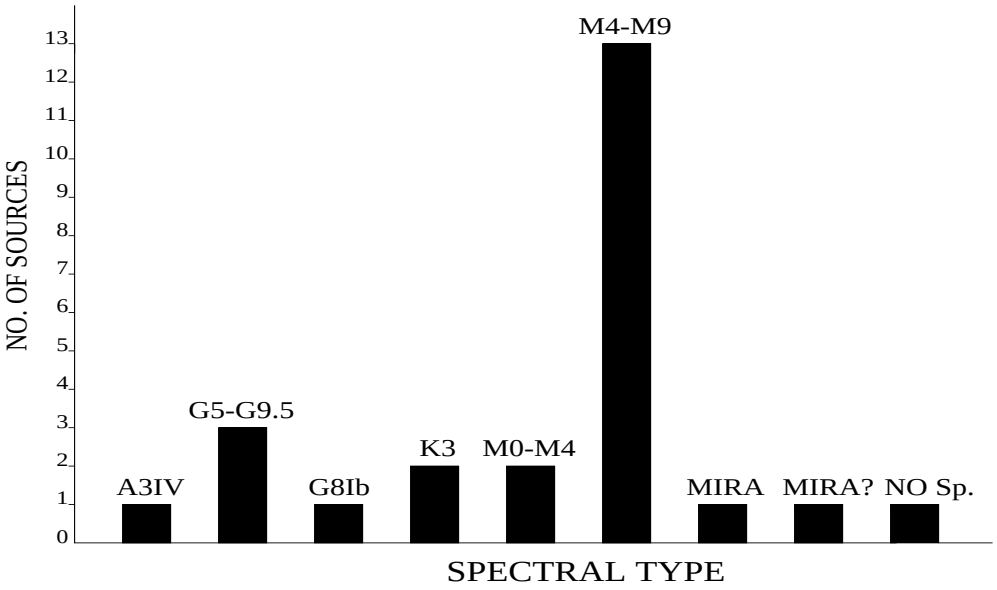

Figure 6.1: Bar chart of spectral type in our sample.

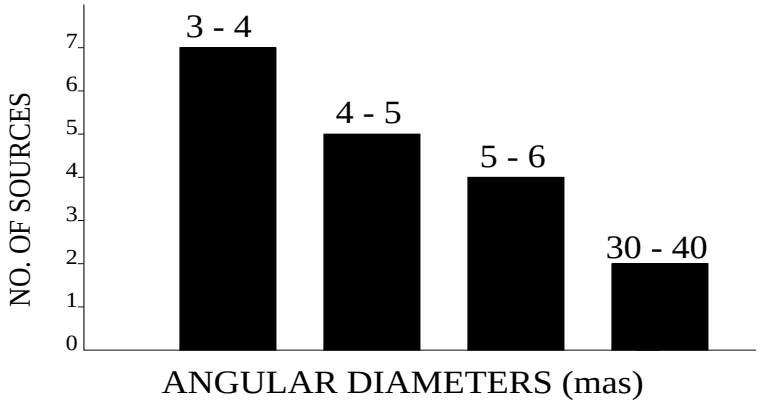

Figure 6.2: Bar chart of resolved angular diameters.

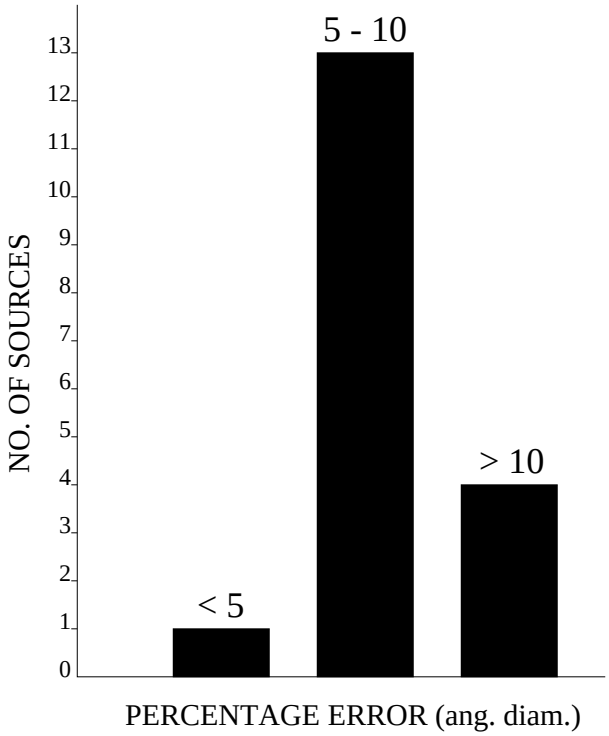

Figure 6.3: Bar chart of percentage error in angular diameter determinations.

Two good lunar occulation light curves of IRC-20563 have been recorded at 2.2mum. Angular diameters of 4.4$\pm$0.5 mas and 4.4$\pm$0.4 mas are obtained for the two epochs of observations repectively. No variation is seen beyond the errors. This is consistent with the results on R Leonis and needs to be further investigated in case of other Mira variables at IR wavelengths.

Angular sizes of 15 M giants ranging in spectral types from M2 – M9 have been derived. Of these, 11 are resolved sources. Using the resolved angular diamters and the derived bolometric fluxes, effective temperatures of stars in this sample have been determined. As can be seen from Fig. 6.1 there is a clustering of spectral types between M5 – M9. Looking at the dearth of HAR measurements of M giants, the present data base is a valuable contribution. The percentage error in the effective temperature determinations is shown in the bar chart plotted in Fig. 6.4. Two of the sources in our sample namely IRC+20067 and IRC+20090 show appreciably low temperatures inconsistent with their spectral class. They are not known Miras but the infrared colours and the derived temperatures put them in the Mira zone (Feast 1996). Spectroscopic and photometric monitoring of these

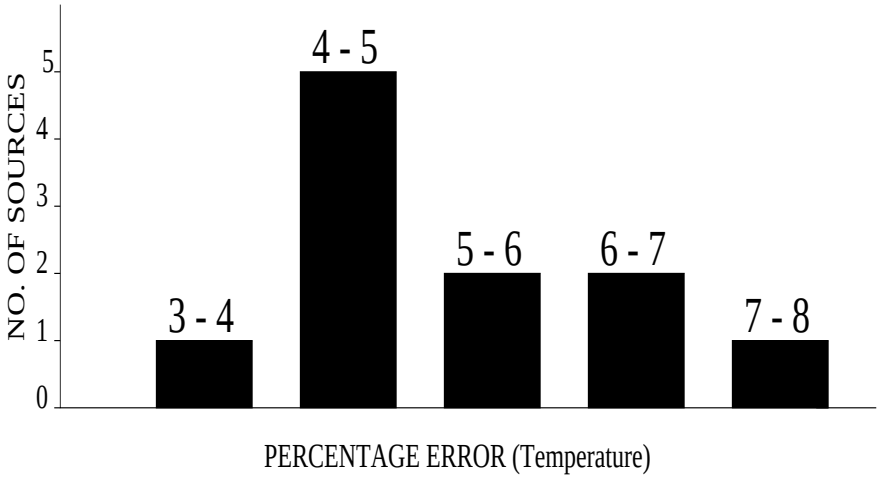

Figure 6.4: Bar chart of percentage error in the derivation of effective temperatures.

sources is needed to establish the nature of these sources and also to validate the accuracy of the derived angular diameters.

6.2 Scope for future work

6.2.1 Spectral classification

As can be deduced from the discussions in Chapter 4, the T_{eff} scale is still not very well established for the M giants especially for M5 and beyond. This is mainly due to paucity of accurate diameter measurements and the uncertainty in the spectral classification. Taking into consideration the variability of these objects a large data base spread over the entire spectral range for a period of several years is required to quantify the scale. Infrared lunar occultations along with the long baseline interferometric techniques hold promise for a large data base of HAR measurements of late M giants to enable an accurate temperature scale to be derived.

In Chapter 4 we have briefly discussed the uncertainty in spectral classification of M giants. This being one of the parameters involved in the temperature calibration, one has to tightly constrain it in order to get an accurate temperature scale. For these cool stars, reliable spectral classification is possible only with spectral features in the infrared. CO absorption becomes prominent in the spectra

of cool stars. The most studied signatures are the ($\Delta\nu = 2$) bands longward of 2.29 μm. The ($\Delta\nu = 3$) series are also prominent but the lines are blended with vibration–rotation lines of OH. The strengthening of CO absorption with decreasing temperature and increasing luminosity has been studied by Kleinmann & Hall (1986), who have also suggested the use of K band spectra for two-dimensional spectral classification. Lancon & Rocca- Volmerange (1992) have presented a library of stellar spectra from 1.428 to 2.5 μm. They have shown that even with a resolving power ~ 500 one can study the decrease in the band strength of ^{12}CO with increasing temperature. In their spectra between 2 to 2.5 μm , the curvature of the (pseudo) continuum increases beyond M5 III and the ^{12}CO strength increases. Similar increase in curvature is also seen in the H band spectra. Apart from this CO absorption signature, the K band spectra also shows strong features of NaI doublet at 2.208 μm and CaI triplet at 2.263 μm. The NICMOS3 array available at Gurushikhar has a resolving power of 1000. Hence, the use of CO bands as a strong diagnostic tool complemented with other atomic line strengths and curvature of the continuum can be exploited to get a more accurate spectral classification of the M giants of our sample and also address the problem of their spectral calibration.

6.2.2 Lunar occultation in the Thermal IR

Occultation measurements have been mostly done at 2.2 μm in the infrared. L band occultations are rare. Only two L band occultations are listed in Richichi et al. (1996) and 5 in White & Feierman (1987). We have also obtained the occultation of R Leo at 3.36μm but with a narrow bandwidth of 0.05 μm. Observing at longer wavelengths has the advantage of preferentially probing the circumstellar environment. Interferometric techniques have just begun to probe the thermal infrared region. A recent work by Mennesson et al. (1999) report the first long baseline interferometric observations of α Bootis and α Herculis in the thermal infrared at 3.75μm using the 21m baseline of IOTA. We propose to observe occultations of

stellar sources bright in the L band with the narrow band filters. Occultation observations in both K and L band simultaneously are also planned with the recently developed two channel IR photometer.

6.2.3 *Use of IR Arrays for lunar occultation*

Other than the introduction of photoelectric techniques in the 50's and IR photometers in the 70's there has hardly been any change in the instrumental aspect of occultation observations. But with the advent of NIR arrays there is likely to be a revolutionary change in terms of sensitivity and application. But observing lunar occultations with the array requires a fast read out of a sub frame of the array. If the fast readout capability is achieved in the IR array, the sensitivity of the lunar occultation technique can be pushed down by a couple of K magnitudes below the TMSS limit of $m_k = 3$ for angular diameter determinations.

The sensitivity limit for detection of close binaries with the array is much more promising than the angular diameter determinations. The capability of the arrays to operate on the bright limb of the moon with very short exposures will enable the true separation of binaries to be determined from a single event by observing both disappearance and reappearance. The improved sensitivity would make the search for low-mass companions of stars in the solar neighbourhood feasible. Within 25pc of the sun $\sim$ 400 objects (Gliese & Jahreiss 1990) are subject to lunar occultation, though a large telescope with IR array is required to observe these. Wavelength-resolved observations of lunar occultation, obtained by dispersing the light so as to enable different parts of the array to record different wavelengths, would help in investigating wavelength-dependent angular size variations of sources, particularly Miras. Since diffraction is a chromatic process, the light curves of different wavelength can be stretched to the same scale and averaged to reduce scintillation noise and hence improve the S/N ratio and thus ultimately improve the resolution.

In conclusion, not withstanding the impressive advances in recent years in the field of optical and near infrared long baseline interferometry, lunar occultation, due to its inherent simplicity and potential, will continue to play an important role in determinations of stellar angular diameters in the future, particularly in isolated 1m class telescopes around the globe. Current trends point to a merging of the data sets of long baseline work and lunar occultation and a more complete uv plane coverage than either of the two techniques taken individually.

Bibliography

[1] Albrow, M. D., Beaulieu, J. -P., Caldwell, J. A. R., Dominik, M., et al. 1999, astro-ph/9811479

[2] Armstrong, J. T., Mozurkewich, D., Rickard, L. J., Hutter, D. J., et al. 1998, ApJ, 496, 550

[3] Aschenbach, B. & Brinkmann, W. 1975, A&A, 41, 147

[4] Ashok, N. M., Chandrasekhar, T., Ragland, S. & Bhatt, H. C. 1994, Exp. Astron., 4, 177

[5] Babcock, H. W. 1953, PASP, 65, 221

[6] Babu, G. S. D. & Shailaja, B. S. 1981. ApSS, 79, 243

[7] Baldwin, J. E., Beckett, M. G., Boysen, R. C., Burns, D., et al., 1996, A&A, 306, L13

[8] Balmforth, N. J., Gough, D. O. & Merryfield, W. J. 1990, *From Miras to planetary nebulae: Which path for stellar evolution?*, eds. Mennessier, M. O. & Omont, A., Gif-sur-Yvette, France, Editions Frontieres, p85

[9] Barnes, T. G. & Evans, D. S. 1976, MNRAS, 174, 489

[10] Barstow, M. A., Holberg, J. B., Fleming, T. A., Marsh, M. C., et al. 1994, MNRAS, 270, 499

[11] Beckers, J. M. 1993, ARAA, 31, 13

[12] Benson, J. A., Hutter, D. J., Elias, N. M., Bowers, P. F., et al. 1997, AJ, 114, 1221

[13] Bessell, M. S., Scholz, M. & Wood, P. R. 1996, A&A, 307, 481

[14] Bester, M., Degiacomi, C. G., Danchi, W. C., Greeenhill, L. J., et al. 1994, IAU Symp. no. 158 : Very High Angular Resolution Imaging, p 257

[15] Bidelman, W. P. 1980, Publ. Warner Swasey Obs.2, No. 6

[16] Blackwell, D. E. & Lynas-Gray, A. E. 1994, A&A, 282, 899

[17] Blackwell, D. E., Shallis, M. J. & Selby, M. J. 1979, MNRAS, 188, 847

[18] Blazit, A., Bonneau, D., Koechlin, L. & Labeyrie, A. 1977, 214, L79

[19] Blow, G. L., Chen, P. C., Edwards, D. A., Evans, D. S. et al. 1982, AJ, 87, 1571

[20] Boffin, H. M. J., Cerf, N. & Paulus, G. 1993, A&A, 271, 125

[21] Bogdanov, M. B. & Cherepaschuk, A. M. 1990, SvA, 34, 247

[22] Böhm-Vitense, E. 1981, ARAA, 19, 295

[23] Born, E. & Debrunner, H. 1979, Ap&SS, 63, 457

[24] Bouchet, P., Schmider, F. X. & Manfroid, J. 1991, A&AS, 91, 409

[25] Breckinridge, J. B. 1972, Appl. Optics, 11, 2996

[26] Brown, J. A., Sneden, C., Lambert, D. L. & Dutchover, E. JR. 1989, ApJS, 71, 293

[27] Burns, D., Baldwin, J.E., Boysen, R.C., Haniff, C.A., et al. 1998, MNRAS, 297, 462

[28] Burns, D., Baldwin, J.E., Boysen, R.C., Haniff, C.A., et al., 1997, MNRAS, 290, L11

[29] Carter, B. S. 1990, MNRAS, 242, 1

[30] Chandrasekhar, T., Ashok, N. M. & Ragland, S. 1992, JAA, 13, 207

[31] Chandrasekhar, T., Ashok, N. M., Tej, A., Watson, P. V. et al. 1996, Earth, Moon and Planets, 75, 157

[32] Cheng, K.-P., Bruhweiler, F. C., Kondo, Y. & Grady, C. A. 1992, ApJ, 396, L83

[33] Cohen, M., Walker, R. G., Carter, B., Hammersley, P., et al. 1999, AJ, 117, 1864

[34] Cruzalèbes, P., Lopez, B., Bester, M., Gendron, E., et al. 1998, A&A, 338, 132

[35] Curie, D. G., Knapp, S.L. & Liewer, K. M. 1974, ApJ, 187, 131

[36] Danchi, W.C., Besta, M., Degiacomi, C.G., Greenhill, L.J., et al. 1994, AJ, 107, 1469

[37] Davis, J., Tango, W. J., Booth, A. J., Thorvaldson, E. D., et al. 1999b, MNRAS, 303, 783

[38] Davis, J., Tango, W. J., Booth, A. J., ten Brummelaar, T. A., et al. 1999a, MNRAS, 303, 773

[39] Deustch, A. J., 1960, in *Stars and Stellar Systems*, ed. Greenstein, J.L., vol6, Chapter 15

[40] de Laverny, P., Geoffray, H., Jorda, L. & Kopp, M. 1997, A&AS, 122, 415

[41] de Vegt, C. 1976, A&A, 47, 457

[42] Di Benedetto, G. P. & Rabbia, Y. 1987, A&A, 188, 114

[43] Di Giacomo, A., Richichi, A., Lisi, F. & Calamai, G. 1991, A&A, 249, 397

[44] Diercks, H. & Hunger, K. 1952, Z. Astron., 31, 182

[45] Draine, B. T. 1981, *Physical Processes in Red Giants*, ed. Iben, I. Jr. & Renzini, A. (Reidel, Dordrecht), p. 317

[46] Draine, B. T. 1985, ApJS, 57, 587

[47] Dumm, T. & Schild, H. 1998, New Astron., 3, 137

[48] Dyck, H. M., Benson, J. A. & Ridgway, S. T. 1993, PASP, 105, 610

[49] Dyck, H. M., van Belle, G. T. & Thompson, R. R. 1998, 116, 981

[50] Dyck, H. M.,Benson, J. A., Carleton, N. P., Coldwell, C., et al. 1995, AJ, 109, 378

[51] Dyck, H. M. 1986, in *Late Stages of Stellar Evolution*, eds. Kwok, S & Pottasch, S.R., D.Reidel Publishing Company, p19.

[52] Dyck, H. M., Benson, J. A., van Belle,G. T. & Ridgway, S. T. 1996, AJ, 111, 1705

[53] Eddington, A. J. 1918, MNRAS, 69, 178

[54] Eitter, J. J. & Beavers, W. I. 1979, ApJS, 40, 475

[55] Evans, D. S. & Fekel, F. C. 1979, ApJ, 228, 497

[56] Evans, D. S., Edwards, D. A., Frueh, M., McWilliam, A. et al. 1985, AJ, 90, 2360

[57] Feast, M. 1996, MNRAS, 278, 11

[58] Feast, M. W., Robertson, B. S. C., Catchpole, R. M., Lloyd Evans, T., et al. 1982, MNRAS, 201, 439

[59] Feast, M., Whitelock, P. A. & Carter, B. S. 1990, MNRAS, 247, 227

[60] Fizeau, A. H. 1868, C.R.Acad. Sci (Paris), 66 : 934

[61] Fluks, M. A., Plez, B., Thè, P. S., de Winter, D., et al. 1994, A&AS, 105, 311

[62] Forest, W. J., Gillet, F.C. & Stern, W. A. 1975, ApJ, 195, 423

[63] Fox, M. W. & Wood, P. R. 1982, ApJ, 259, 198

[64] Gatewood, G. 1992, PASP, 104, 23

[65] Gay, J.& Mekarnia, D. 1988, in *High Resolution Imaging by Interferometry* ed. Merkle, F., Conf. and Workshop proc., vol. 29, ESO, p811.

[66] Gezari, D.Y., Schmitz, M., Pitts, P.S. & Mead, J.M. 1993, *Catalog of Infrared Observations, NASA Reference Publication 1294*

[67] Gliese, W. & Jahreiss, H. 1990, *Preliminary Version of the 3rd Catalogue of Nearby Stars.*

[68] Granes, P., Vakili, F. & Thom, C. 1986, A&A, 165, L13

[69] Halbwachs, J. L. 1981, A&AS, 44, 47

[70] Hanbury Brown, R. 1974, in *The Intensity Interferometer*, London: Taylor & Francis

[71] Hanbury Brown, R., Davis, J., Allen, L.R. & Rome, J.M. 1967, MNRAS, 137, 393

[72] Haniff, C. A., Scholz, M. & Tuthill, P. G. 1995, MNRAS, 276, 640

[73] Hansen, O. L. & Blanco, V. M. 1973, AJ, 78, 669

[74] Hansen, O. L. & Blanco, V. M. 1975, AJ, 80, 1011

[75] Harlan, E. A. 1969, AJ, 74, 916

[76] Hashimoto, O. 1994, A&AS, 107, 445

[77] Hayes, D. S. 1978, *IAU Symp. No. 80, The HR diagram*, ed. Philip, A. G. D., p65

[78] Hofmann, K. -H., Scholz, M. & Wood, P. R., 1998, A&A, 339, 846

[79] Hron, J., Aringer, B. & Kerschbaum, F. 1997, A&A, 322, 280

[80] Iben, I. 1985a, Quart. Journ. Astr. Soc., 26, 1

[81] Iben, I. 1985b, A&SS, 117, 1

[82] Johnson, H. L. 1966, ARAA, 4, 193

[83] Johnson, M. A., Betz, A. L. & Townes, C. H. 1974, Phys Rev Lett, 33, 1617

[84] Jones, K. L., Robinson, R. D., Slee, O. B. & Stewart, R. T. 1992, MNRAS, 256, 535

[85] Jones, T. W. & Merrill, K. M. 1976, ApJ, 209, 509

[86] Jura, M. & Kleinmann, S. G. 1990, ApJS, 73, 769

[87] Jura, M. & Kleinmann, S. G. 1992, ApJS, 83, 329

[88] Keenan, P. C. & Barnbaum, C. 1999 ApJ, 518, 859

[89] Keenan, P. C. & McNeil, R. C. 1989, 71, 245

[90] Keenan, P. C. & Pitts, R. E. 1980, ApJS, 42, 541

[91] Kenyon, S. J. & Fernandez-Castro, T. 1987, AJ, 93, 938

[92] Kenyon, S. J. & Gallagher, J. S. 1983, AJ, 88, 666

[93] Kerschbaum, F. & Hron, J. 1994, A&AS, 106, 397

[94] Klienmann, S. G. & Hall, D. N. B. 1986, ApJS, 62, 501

[95] Knapp, G. R. & Morris, M. 1985, ApJ, 292, 640

[96] Knoechel, G. & von der Heide, K. 1978, A&A, 67, 209

[97] Koechlin, L. & Rabbia, Y. 1985, A&A, 153, 91

[98] Kukarkin, B. V., Kholopov, P. N., Efremov Yu. N., Kukarkina, N. P., et al. 1969, General Catalogue of Variable Stars, Academy of Sciences of the USSR, Moscow

[99] Labeyrie, A. 1970, A&A, 6, 85

[100] Labeyrie, A. 1975, ApJ, 196, L71

[101] Labeyrie, A. 1978, ARAA, 16, 77

[102] Labeyrie, A., Authier, B., Boit, J. L., de Graauw, T., et al. 1984, in *Trio: A Kilometric Optical Array Controlled by Solar Sails*, BAAS, 16, 3

[103] Labeyrie, A., Koechlin, L., Bonneau, D., Blazit, A. et al. 1977, ApJ, 218, L75

[104] Labeyrie, A., Schumacher, G., Dugue, M., Thom, C., et al. 1986, A&A, 162, 359

[105] Lahulla, J. F. 1987, PASP, 99, 998

[106] Lancon, A. & Rocca- Volmerange, B. 1992, A&AS, 96, 593

[107] Lang, K. R. 1992, *Astrophysical Data: Planets and Stars*, Springer Verlag.

[108] Lattanzi, M. G., Munari, U., Whitelock, P. A. & Feast, M. W. 1997, ApJ, 485, 328

[109] Lockwood, G. W. 1985, ApJS, 58, 167

[110] Lopez, B., Danchi, W. C., Bester, M., Hale, D. D. S., et al. 1997, ApJ, 488, 807

[111] Lyne, A. G. 1972, MNRAS, 158, 431

[112] Manduca, A. 1979, A&AS, 36, 411

[113] Mariotti, J. M., Chelli, A., Foy, R., Lena, P., et al. 1983, A&A, 120, 237

[114] Mattei, J. A. 1998, Observations from the AAVSO International Database (private communication)

[115] McAlister, H. A. 1985, ARAA, 23, 59

[116] McCarthy, D. W. & Low, F. J. 1975, ApJ, 202, L37

[117] Mennesson, B., Mariotti, J. M, Coudé du Foresto, V., Perrin, G., et al. 1999, A&A, 346, 181

[118] Merrill, K. M. & Stein, W. A. 1976, PASP, 88, 285

[119] Michelson, A. A. & Pease, F. G. 1921, ApJ, 53, 249

[120] Moffett, T. J. & Barnes, T. G. 1979, PASP, 91, 180

[121] Mondal, S., Chandrasekhar, T., Ashok, N. M. & Kikani, P. K. 1998, BASI, 27, 335

[122] Mozurkewich, D., Hutter, D. J., Johnston, K. J., Simon, R. S., et al., 1988, AJ, 95, 1269

[123] Mozurkewich, D., Johnston, K. J., Simon, R. S. & Bowers, P. F. 1991, AJ, 101, 2207

[124] Nassau, J. J. & Blanco, V. M. 1954, ApJ, 120, 118

[125] Nather, R. E. & Wild, P. A. T. 1973, AJ, 78, 628

[126] Nather, R. E. 1970, AJ, 75, 583

[127] Nather, R. E.& McCants, M. M. 1970, AJ, 75, 963

[128] Neugebauer, G., Becklin, E. E., Clough, G., Law, A., 1973, S&T, 45, 91

[129] Noguchi, K. 1989, PASJ, 41, 779

[130] Noguchi, K. 1990, PASJ, 42, 419

[131] Nyman, L. A., Booth, R. S., Carlstrom, U., Habing, H. J., et al. 1992, A&AS, 93, 121

[132] Olnon, F. M., Raimond, E., Neugebauer, G., van Duinen, R. J., et al. 1986, A&AS, 65, 607

[133] Ostlie, D. A. & Cox, A. N. 1986, ApJ, 311, 864

[134] Perrin, G., Coudé du Foresto, V., Ridgway, S. T., Mennesson, B., et al. 1999, A&A, 345, 221

[135] Perrin, G., Coudé du Foresto, V., Ridgway, S. T., Mariotti, J. M., et al. 1998, A&A, 331, 619

[136] Pettit, E. & Nicholson, S. B. 1933, ApJ, 78, 320

[137] Poss, H. L. 1971, *Highlights of Astronomy, Vol. 2*, ed. de Jager, c. p692

[138] Press, W. H., Teukolsky, S. A., Vellerling, W. T. & Flannery, B. P. 1992, *Numerical Recipes in Fortran: The Art of Scientific Computing*, Cambridge Univ. Press.

[139] Radick, R. & Lien, D. 1980, AJ, 85, 1053

[140] Ragland, S. 1996, Ph D. Thesis, Gujarat Univ., India

[141] Ragland, S., Chandrasekhar, T. & Ashok, N. M. 1997a, MNRAS, 287, 681

[142] Ragland, S., Chandrasekhar, T. & Ashok, N. M. 1997b, A&A, 319, 260

[143] Richichi A. 1994, IAU Sym. 158, Very High Resolution Imaging, eds. Robertson, J. G. & Tango, W. J., p71.

[144] Richichi, A. 1989, A&A, 226, 366

[145] Richichi, A. & Lisi, F. 1990, A&A, 230, 355

[146] Richichi, A., Baffa, C., Calamai, G. & Lisi, F. 1996a, AJ, 112, 2786

[147] Richichi, A., Calamai, G. & Leinert, Ch. 1994a, A&A, 286, 829

[148] Richichi, A., Calamai, G., Leinert, Ch., Stecklum, B. et al. 1996b, A&A, 309, 163

[149] Richichi, A., Calamai, G., Leinert, Ch. & Stecklum, B. 1997, A&A, 322, 202

[150] Richichi, A., Chandrasekhar, T., Lisi, F., Howell, R.R., et a;. 1995, A&A, 301, 439

[151] Richichi, A., Fabbroni, L., Ragland, S. & Scholz, M. 1999, 344, 511

[152] Richichi, A., Leinert, Ch., Jameson, R. & Zinnecker, H. 1994b, A&A, 287, 145

[153] Richichi, A., Lisi, F. & Di Giaconio, A. 1992, A&A, 254, 149

[154] Richichi, A., Ragland, S. & Fabbroni, L. 1998a, A&A, 330, 578

[155] Richichi, A., Ragland, S., Stecklum, B. & Leinert, Ch. 1998b, 338, 527

[156] Richichi, A., Salinari, P. & Lisi, F. 1988, ApJ, 326, 791

[157] Ricker, G. R., Ryckman, S. G., Ballintine, J. E., Doty, J. P., et al. 1975, ApJL, 197, 83

[158] Ridgway, S. T., Jacoby, G. H., Joyce, R. R., Siegel, M. J. et al. 1982, AJ, 87, 808

[159] Ridgway, S. T., Wells, D. C., Joyce, R. R. & Allen, R. G. 1979, AJ, 84, 247

[160] Ridgway, S. T., Joyce, R. R., White, N. M. & Wing, R. F. 1980, ApJ, 235, 126

[161] Robertson, B. S. C. & Feast, M. W. 1981, MNRAS, 196, 111

[162] Roddier, C. & Roddier, F. 1983, ApJ, 270, L23

[163] Roddier, C. & Roddier, F. 1985, ApJ, 295, L21

[164] Roddier, C., Roddier, F., Petrov, R., Martin, et al. 1986, ApJ, 305, L77

[165] Rowan-Robinson, M. & Harris, S. 1983, MNRAS, 202, 767

[166] Sargent, A & Beckwith, S. 1987, ApJ, 323, 294

[167] Scargle, J. D. & Strecker, D. W. 1979, ApJ, 228, 838

[168] Schmidtke, P. C., Africano, J. L., Jacoby, G. H., Joyce, R. R. et al. 1986, AJ, 91, 961

[169] Scholz, M. 1997, *Fundamental Stellar Properties: The Interaction between Observation and Theory, IAU Symp. No. 189.*, eds. Bedding, T. R., Booth, A. J. & Davis, J., Kluwer, Dordrecht, p51

[170] Scholz, M. & Takeda, Y. 1987, 186, 200

[171] Shallis, M. J. & Blackwell, D. E. 1979, A&A, 79, 48

[172] Shallis, M. J., Booth, A. J., Baruch, J. E. F. & Selby, M. J. 1985, MNRAS, 213, 307

[173] Shao, M. & Colavita, M. M. 1992, ARAA, 30, 457

[174] Shao, M. & Staelin, D. H. 1980, Appl. Opt, 19, 1519

[175] Shao, M., Colavita, M. M., Staelin, D. H., Johnston, K. J., et al., 1987, AJ, 93, 1280

[176] Shao, M., Colavita, M. M., Hines, B. F., Staelin, D. H., et al. 1988, A&A, 193, 357

[177] Simon, M., Chez, A. M., Leinert, Ch., Cassar, L., et al. 1995, ApJ, 443, 625

[178] Simon, M., Peterson, D. M., Longmore, A. J., Storey, J. W. V., et al. 1985, ApJ, 298, 328

[179] Singal, A. K. 1987, A&AS, 169, 91

[180] Slee, O. B., Stewart, R. T., Bunton, J. D., Beasley, A. J., et al. 1989, MNRAS, 239, 913

[181] Stencel, R. E. & Backman, D. E. 1991, ApJS, 75, 905

[182] Strecker, D. W. 1973, Ph D. Thesis, University of Minnesota.

[183] Strecker, D. W., Erickson, E. F. & Witteborn, F. C. 1978, AJ, 83, 26

[184] Sutton, E. C., Storey, W. V., Betz, A. L. & Townes, C. H. 1977, ApJ, 217, L97

[185] Tej, A., Chandrasekhar, T. C., Ashok, N. M., Ragland, S., et al. 1999, AJ, 117, 1857

[186] Thè, P. S., Thomas, D., Christensen, C. G. & Westerlund, B. E. 1990, PASP, 102, 565

[187] Traub, W. A. & Gursky, H. 1980, in *Coherent Optical Arrays for Space Astronomy*, SPIE, vol 228

[188] Tsuji, T. 1978, PASJ, 30, 435

[189] Tuchman, Y. 1991, ApJ, 383, 779

[190] Tuthill, P. G., Haniff, C. A., Baldwin, J. E. 1995, MNRAS, 277, 1541

[191] Tuthill, P. G., Haniff, C. A., Baldwin, J. E. & Feast, M. W. 1994, MNRAS, 266, 745

[192] van Belle, G. T., Dyck, H. M., Benson, J. A., & Lacasse, M. G. 1996, AJ, 112, 2147

[193] van Belle,G.T., Lane, B. F., Thompson, R. R., Boden, A. F., et al. 1999, AJ, 117, 521

[194] van Leeuwen, F., Feast, M.W., Whitelock, P.A. & Yudin, B. 1997, MNRAS, 287, 955

[195] van der Veen, W. E. C. J. & Habing, H. J. 1988, A&A, 194, 125

[196] Volk, K. & Cohen, M. 1989, AJ, 98, 931

[197] Volk, K. & Kwok, S. 1987, ApJ, 315, 654

[198] Von Hoerner, S. 1964, ApJ, 140, 65

[199] Warner, B. 1988, in *High Speed Astronomical Photometry*, Cambridge Univ Press, p35.

[200] White, N. M. 1978, *IAU Sym. No 80 The HR Diagram*, eds. Philip, A. G. D. & Hayes, D. S., p447

[201] White, N. M. 1987, Vistas in Astronomy, 30, 13

[202] White, N. M. & Feierman, B.H. 1987, AJ, 94, 751

[203] Whitelock, P., Menzies, J., Feast, M., Catchpole, R. et al. 1995, MNRAS, 276, 219

[204] Whitford, A. E. 1946, AJ, 52, 131

[205] Whitford, A. E. 1939, ApJ, 89, 472

[206] Williams, J. D. 1939, ApJ, 89, 467

[207] Wilson, L. A. 1983, *Pulsations in Classical and Cataclysmic Variable Stars.*, eds. Cox, J.P. & Hansen, C.J., University of Colorado, Boulder, p 284

[208] Wood, P. R. 1990, *From Miras to planetary nebulae: Which path for stellar evolution?*, eds. Mennessier, M. O. & Omont, A., Gif-sur-Yvette, France, Editions Frontieres, p67

[209] Wood, P. R 1975, MNRAS, 171, 15

[210] Wood, P. R. 1982, *Pulsations in Classical and Cataclysmic Variable Stars.*, eds. Cox, J. P. & Hansen, C. J., University of Colorado, Boulder, p 269

[211] Ya'ari, A. & Tuchman, Y. 1999, ApJ, 514, L35

[212] Young, K., Phillips, T. G. & Knapp, G. R. 1993, ApJS, 86, 517